Influence of spectral fine structure on the electronic transport of icosahedral quasicrystals

von der Fakultät für Naturwissenschaften
der Technischen Universität Chemnitz genehmigte

Dissertation

zur Erlangung des akademischen Grades
doctor rerum naturalium
(Dr. rer. nat.)

vorgelegt von

Carlos V. Landauro Sáenz

geboren am 2. März 1972 in Huaraz, Perú.

eingereicht am 11. April 2002

Gutachter: Prof. Dr. H. Solbrig, TU Chemnitz
Prof. Dr. P. Häussler, TU Chemnitz
Prof. Dr. H.-R. Trebin, Universität Stuttgart.

Tag der Verteidigung: 15. Juli 2002

Archiv: http://archiv.tu-chemnitz.de/pub/2002/....

Bibliographische Beschreibung

Carlos V. Landauro Sáenz
Influence of spectral fine structure on the electronic transport of icosahedral quasicrystals
Technische Universität Chemnitz, Fakultät für Naturwissenschaften
Dissertation (in englischer Sprache), 2002

Referat

Die Spektrale Leitfähigkeit ikosaedrischer Approximanten zeigt Feinstrukturen (∼100 meV) die das besondere elektronische Transportverhalten der Quasikristalle und Approximanten erklären können. Der Ursprung diese spektralen Feinstrukturen liegt im Zusammenwirken der typischen mehrkomponentigen Atomcluster des Systems. Das Konzept stellt Struktur und chemische Dekoration auf der Längenskala der *Cluster* über ausgedehnte Quasiperiodizität.

Ab-initio Methode mit und ohne periodische Randbedingungen werden hier angewendet, um das Zusammenwirken der Cluster für niedere Approximanten ikosaedrischer Quasikristalle zu untersuchen. Deshalb werden die Linearen Muffin-Tin Orbitale in einem Superzellenkonzept, die Tight-Binding Linearen Muffin-Tin Orbitale in einem Cluster-Rekursionsverfahren und die Landauer/Büttiker-Methode in dieser Arbeit eingesetzt.

Auf der Grundlage der *ab-initio* Ergebnisse werden spektrale Modelle (Lorentz-Funktionen) für den spektralen spezifischen Widerstand gebildet. Der Übergang zum Quasikristall erfolgt durch Skalierung der Modellparameter auf der Grundlage der gemessenen Thermokraft. Die optische Leitfähigkeit und die Temperaturverläufe des Widerstandes, der Thermokraft, des Hall-Koeffizienten und der elektronischen Wärmeleitfähigkeit einiger ikosaedrischer Systeme werden so durch je zwei Lorentz-Funktionen beschrieben.

Wir zeigen, dass die Transportanomalien zusammen mit den spektralen Feinstrukturen empfindlich vom Subsystems des jeweils aktiven Übergangsmetalls abhängen (Orientierung und Dekoration der ikosaedrischen Cluster).

Schlagwörter

Quasikristalle, Ikosaedrische *Cluster*, Pseudogap, Übergangsmetalle, Elektronische Transport, Kubo-Greenwood Formel, Transportkoeffizienten, Linearen Muffin-Tin Orbital, Tight-Binding Linear Muffin-Tin Orbital, Landauer/Büttiker Leitwert.

Contents

Chapter 1

Introduction

Quasicrystals open a new class of matter in the solid state between the amorphous and crystalline systems. The interest to understand the physical properties of these systems was rapidly growing. The only geometrical point of view, that the new materials can be arranged in quasiperiodic order is interesting and was a crucial point to change the standard ideas of the crystallography. Since the discovery of the rapidly solidified Al-Mn quasicrystal in 1984 [Shechtman 84], hundreds of new alloys have been observed with quasicrystalline symmetry.

The electronic behavior of quasicrystals reveals very interesting properties. For example, materials with abundant content of aluminium (that is a good metal) and poor in transition metals, such as Al-Pd-Re, Al-Pd-Mn, Al-Cu-Fe, Al-Cu-Ru, show high resistivities close to a metal-insulator transition. This is not due to the disorder in the system, as the Anderson transition, but a new *"parameter"*, that may depend on the quasiperiodicity and on the chemical order of these systems must be taken into account. Moreover, the temperature dependence of the resistivity behaves non-metallic, the Hall coefficient is three orders of magnitude larger than for related amorphous phases, the thermopower changes its sign with temperature, the thermal conductivity is two orders of magnitude lower than in fcc-Al.

The consequences of quasiperiodicity for the electronic transport properties were intensively studied using very simple Hamiltonian models (tight binding Hamiltonians: s-orbitals, and nearest neighbors interactions only) and *ab-initio* band-structure calculations. In the latter one, the electron was treated as ballistic (Bloch-Boltzmann theory). Very few calculations of the electronic transport of realistic materials were carried out using the Kubo-Greenwood formula. Strong experimental evidences (for instance, very high resistivities, changes of sign of the Hall coefficient/thermopower with the temperature and chemical composition) show that the electrons do not behave as being nearly free. Theoretical discussions [Sire 94, Yamamoto 95a, Fujiwara 96] show the limitations of semi-classical calculations for the electronic transport of quasicrystals. In this sense, here it is intended to study the electronic transport of quasicrystalline materials employing the Kubo-Greenwood formula. This formula allows to employ $\underline{k}$-space methods (for unit cells with ~250 atoms) as well as $\underline{r}$-space methods (together with the recursion procedure one can treat clusters with more than ∼1000 atoms).

The question if the above mentioned *anomalous* properties arise from only the quasiperiodic atomic arrangement or from the chemical order, or from both, is a matter of principal interest in this work. Our starting point is the investigation of spectral fine structures in the density of states around the Fermi energy, both as results of theoretical and experimental works. Such features of the density of states around the Fermi energy, do not appear in other amorphous and crystalline phases of similar concentrations. Hence, it is expected that these fine spectral features are the origin of the unusual electronic properties of quasicrystals.

Moreover, we will comment on the potential applicability of quasicrystals in the industry. Practical applications for which quasicrystals may prove suitable are derived from their physical and chemical properties. Specially exciting properties for industrial applications are low coefficients of friction, good wear-resistance, and good oxidation-resistance. Indeed, applications of these materials exist already in the marketplace. Non-stick cookware can be purchased which contains a quasicrystal coating, rather than a teflon coating, and which is impervious to scratching by metal utensils.

The present work is organized in the following way. In Chapter 2 we review the structural and geometrical properties of quasicrystals. The chapter 3 is devoted to discuss about the basic concepts of the electronic transport and their applicability to quasicrystals. The relation between spectral fine structures and anomalous transport is treated in chapter 4. The importance of extended quasiperiodicity and/or chemical sensitivity to explain the electronic properties of quasicrystals is discussed in chapter 5. *Ab-initio* methods, such as the LMTO-ASA supercell method, the TB-LMTO cluster recursion, and the Landauer/Büttiker approach, are presented.

In Chapter 6, spectral fine structures, on the ∼100 meV scale, are shown. They can explain consistently the temperature dependent transport coefficients, such as the conductivity, thermopower, Hall coefficient, and electronic thermal conductivity. The i-Al-Cu-Fe quasicrystal is taken as an example. The spectral properties of i-Al-Pd-Re approximant models are presented in chapter 7. The temperature dependent conductivity is modeled for samples ranging from $1635 \mu\Omega cm$ to more than $25500 \mu\Omega cm$. The possible scenario of a metal-insulator transition is also discussed. Chapter 8 deals with the optical conductivity of low order approximants. A model for the optical conductivity of quasicrystals is also presented. The possibility to apply icosahedral quasicrystals as thermoelectric devices is discussed in chapter 9. Finally, the relation of filtered electronic wave functions and transport is studied in chapter 10.

Chapter 2

Quasicrystals among related phases

2.1 Quasiperiodicity

The atoms in quasicrystals are arranged in a *deterministic nonperiodic* fashion. This arrangement gives rise to striking properties, such as i) *sharp* diffraction patterns with rotational symmetries that are *forbidden* by classical crystallography, ii) long-range order without translational symmetry, iii) embedding in an n-dimensional reciprocal lattice gives a periodic n-dimensional structure, and iv) no average structure in three-dimensions (non-crystallographic point symmetry).

The previously discussed structural properties of quasicrystals hinder to describe them in three-dimensional space as easily as normal crystal structures. The reflections of normal crystals are characterized by only three integer Miller indices. This is due to the three-dimensional translational periodicity of the structure. On the other hand, if we intend to do this in quasicrystals, at least five basic vectors are necessary. Thus, we need five Miller indices for polygonal (two-dimensional) quasicrystals and six Miller indices for icosahedral quasicrystals. Hence, the five (six) vectors span the reciprocal space to five (six) dimensions. Therefore, there is also a five (six) dimensional direct space from which the structure can be built. This means, a quasiperiodic structure can be projected from a periodic one in a high-dimensional space of five (six) dimensions. This way to describe quasicrystals enables us to describe the whole structure with a finite set of parameters.

The complexity of the structure of quasicrystals, in comparison with other phases, can be summarized as follows: quasicrystals are *long-range ordered* structures (in difference to amorphous phases), *without translational* symmetry (in difference to crystals), and they have *no average structure in three-dimensions* (in difference to incommensurable structures).

Cut-and-project method

In order to understand the concept of high dimensionality for the geometrical description of quasicrystals one can employ the cut-and-projection method [Katz 85, Kalugin 85, Katz 86, Elser 86]. The construction of an icosahedral Penrose tiling serves as a basic example.

For icosahedral quasicrystals we must embed the three dimensional quasicrystal in a six-dimensional space. In this case, the six dimensional space is a simple cubic lattice with lattice constant a and unit-vectors,

$$\begin{aligned} \hat{e}_1 &= (1,0,0,0,0,0) \\ \hat{e}_2 &= (0,1,0,0,0,0) \\ &\vdots \\ \hat{e}_6 &= (0,0,0,0,0,1). \end{aligned} \tag{2.1}$$

From the origin of this lattice we can draw a three dimensional space which is called the *parallel* or *physical* space, $E^{||}$. The space perpendicular to $E^{||}$ is called the *orthogonal* space, $E^{\perp}$. For example, for the one dimensional case (Fibonacci chain), the hyper-space is a two dimensional simple cubic lattice and the physical space is a line crossing the origin of this lattice with slope $\tau^* = (\sqrt{5}+1)/2$.

Now, to obtain the quasiperiodic structure in $E^{||}$ one must project those points of the six dimensional cubic lattice onto $E^{||}$ which have projections to $E^{\perp}$ inside the acceptance domain. This acceptance domain is obtained by projecting the six-dimensional unit cell onto $E^{\perp}$, in this case a *triacontahedron*. That means, a point $\underline{x} = a \cdot (n_1, n_2, n_3, n_4, n_5, n_6)$ of the six-dimensional cubic lattice is projected onto the parallel or orthogonal space by,

$$\begin{aligned} \underline{x}^{||} &= P^{||}(\tau^*)\, \underline{x} \\ \underline{x}^{\perp} &= P^{\perp}(\tau^*)\, \underline{x} \quad . \end{aligned} \tag{2.2}$$

Only when $\underline{x}^{\perp}$ lies inside the triacontrahedron, $\underline{x}^{||}$ is a vertex of the quasiperiodic structure. The projection matrices $P(\tau^*)$ are defined as,

$$P^{||}(\tau^*) = \frac{1}{\sqrt{2(2+\tau^*)}} \begin{pmatrix} 1 & \tau^* & 0 & -1 & \tau^* & 0 \\ \tau^* & 0 & 1 & \tau^* & 0 & -1 \\ 0 & 1 & \tau^* & 0 & -1 & \tau^* \end{pmatrix} \quad , \tag{2.3}$$

and

$$P^{\perp}(\tau^*) = \frac{1}{\sqrt{2(2+\tau^*)}} \begin{pmatrix} -\tau^* & 1 & 0 & \tau^* & 1 & 0 \\ 1 & 0 & -\tau^* & 1 & 0 & \tau^* \\ 0 & -\tau^* & 1 & 0 & \tau^* & 1 \end{pmatrix} \quad . \tag{2.4}$$

It is also important to note that the projection-matrix $P^{||}(\tau^*)$ contains the required icosahedral symmetry with basics vectors $\underline{a}_1 = \lambda(1,\tau^*,0)$; $\underline{a}_2 = \lambda(\tau^*,0,1)$; $\underline{a}_3 =$

$\lambda(0,1,\tau^*)$; $\underline{a}_4 = \lambda(-1,\tau^*,0)$; $\underline{a}_5 = \lambda(\tau^*,0,-1)$; and $\underline{a}_6 = \lambda(0,-1,\tau^*)$ in the physical three dimensional space ($\lambda = a/\sqrt{2(2+\tau^*)}$).

This geometrical description of quasicrystals provides the corresponding diffraction patterns found experimentally (see [Tsai 99] and references therein). Geometrically, quasicrystals are classified as octagonal, decagonal, dodecagonal, or icosahedral. Moreover, octagonal, decagonal, and dodecagonal quasicrystals are described as a periodic stacking of aperiodically ordered planes (two-dimensional quasicrystals). Icosahedral quasicrystals, on the other hand, are quasiperiodic in the three principal axes (three-dimensional quasicrystals).

2.2 Formation and stoichiometry region

The formation of quasicrystals is closely related to the location of the elements in the periodic table [Tsai 99]. Icosahedral quasicrystals are commonly associated with crystalline phases containing icosahedrally packed groups of atoms [Tsai 99], and they are electronically stabilized.

Several quasicrystals that are thermodynamically stable can be grown employing conventional crystal growth techniques. Quasicrystals of high structural quality, such as the Al-Pd-Mn [Yokoyama 92] and the Al-Ni-Co [Kortan 93] alloys, have been grown with sizes of the order of ∼1 cm.

Phase diagrams have been redrawn to include quasicrystals. Quasicrystals occupy narrow composition regions, and they are normally surrounded by crystalline and amorphous phases. Phase diagrams of different icosahedral phases can be found in [Tsai 99]. For instance, the composition region of the icosahedral Al-Cu-Fe quasicrystal lies between $Al_{64.5}Cu_{23}Fe_{12.5}$ and $Al_{62}Cu_{26.5}Fe_{11.5}$ [Tsai 99]. At 953 K, the composition of the icosahedral phase extends over a triangle with vertices of (Al,Cu,Fe) compositions of respectively (62.4,24.4,13.2), (65,23,12), and (61,28.4,10.6) [Gratias 93]. This is a very small composition region in comparison with the existence region of related amorphous and crystalline phases. For example, the β-phase with CsCl-type structure and composition close to $Al_{50}(CuFe)_{50}$, the γ-phase that is isostructural to the monoclinic $Al_{13}Fe_4$ structure, and the ω-phase with tetragonal structure and $Al_{70}Cu_{20}Fe_{10}$ composition are crystals found around the icosahedral structure. Fig. (2.1) shows a schematic representation of the phase diagram of the Al-Cu-Fe system. Similar small regions of existence are found in other quasicrystals. This is an interesting point because experimental works [Lindqvist 93, Haberkern 00a] show that the electronic properties are sensitive to very small composition changes (of the order of 0.5 atom percent [Lindqvist 93]) which is not the case for their related amorphous or crystalline[1] phases.

---

[1] In crystals, more precisely crystalline metals, small composition changes are given by the presence of vacancies, for example. Then, it is not expected that changes less than 5% of the vacancy density provide strong changes on the electronic transport.

Approximant phases form also part of the phase diagram of quasicrystals. They are crystalline alloys with similar local order as quasicrystals and can be found around the composition region of quasicrystals. For instance, for the Al-Cu-Fe phases, the orthorhombic o-$Al_{60.4}Cu_{29.9}Fe_{9.7}$, the pentagonal P1-$Al_{63.6}Cu_{24.5}Fe_{11.9}$, and the rhombohedral R-$Al_{62.8}Cu_{26}Fe_{11.2}$ approximant phases have been studied [Berger 95].

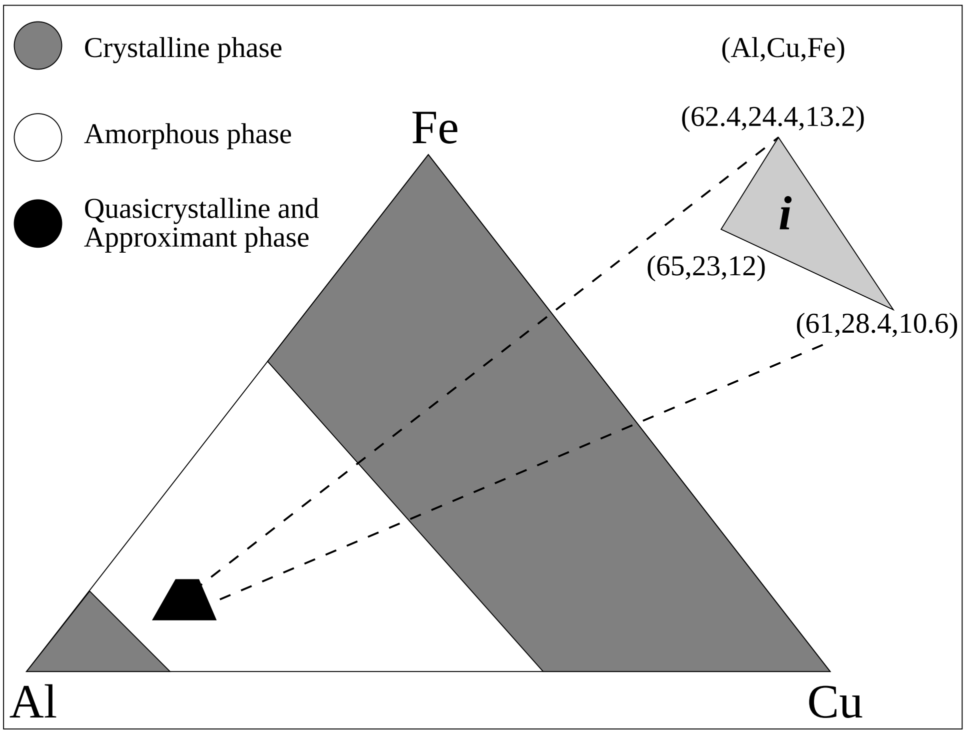

Figure 2.1: Schematic phase diagram of Al-Cu-Fe: the region of existence of approximants and quasicrystals is very small in comparison with their related amorphous and crystalline phases. Similar small regions of existence are found in other quasicrystals.

Important relations between approximants and quasicrystals are: i) the similar composition region, ii) the same local order, and iii) the similar local chemical decoration. In this sense, it is to expect that the physical properties of approximants and quasicrystals must be similar. This point will be discussed in more detail in the following chapters.

Chapter 3

Basic concepts of the electronic transport and quasicrystals

Experimental studies of the resistivity in quasicrystals exhibit peculiar behaviors which are, as yet, not fully understood [Poon 92, Berger 94, Rapp 99]. The resistivities are of the order of $\sim$100-500 $\mu\Omega cm$ for disordered metastable quasicrystals, $\sim$800 $\mu\Omega cm$ for the first discovered stable i-Al-Cu-Li quasicrystal, and $\sim$10000 $\mu\Omega cm$ for the thermodynamically stable and structurally perfect icosahedral quasicrystals, such as i-Al-Cu-(Fe/Ru) and i-Al-Pd-Mn. These values are anomalously high for materials that contain $\sim$ 60-70 at.% of metallic elements (commonly Al). In comparison, amorphous metals have typical resistivities of a few 10^2 $\mu\Omega cm$, and real metals reach resistivities of a few $\mu\Omega cm$, due to defects or phonons. Furthermore, the resistivities of quasicrystals increase after removing the defects by annealing. For instance, the resistivity, at 4 K, of $Al_{62}Cu_{25.5}Fe_{12.5}$ increases from 5500 $\mu\Omega cm$ to 7500 $\mu\Omega cm$ by structural improvement [Berger 94]. The resistivity decreases with rising temperature. Power laws [Gignoux 97, Tamura 97, Lalla 95] and variable range hopping [Guo 96, Delahaye 00] conduction have been reported. Quantum interferences effects and electron-electron interaction are also proved important at very low temperatures [Rapp 99].

An interesting property, found experimentally [Madel 00], is that the conductivity of thin film quasicrystals and related amorphous phases follow a common inverse Matthiessen rule,

$$\sigma(T) = \sigma_0 + \Delta\sigma(T) \quad , \tag{3.1}$$

where σ_0 depends only on the sample at $T = 0$. This rule was previously established [Mayou 93] for quasicrystals and approximants. The inverse Matthiessen rule is contrary to metals where a corresponding rule holds for the resistivity, $\rho(T) = \rho_0 + \Delta\rho(T)$.

In the following, the electronic transport of quasicrystals will be discussed under various points of view.

3.1 Ballistic electrons: resistivity due to scattering

This section deals with different explanations of the electronic transport starting from crystalline approximants where the resistivity is only due to impurity scattering between ballistic states. Models such as the two-band model and the narrow-band model will be discussed in the framework of quasicrystals. First, the influence of the structure on the resistivity is discussed.

Influence of the structure

Amorphous metals and quasicrystals of similar concentrations possess an electronically induced peak in the static structure factor at $2k_F$ [Roth 99] (k_F is the Fermi wave number). Hence, the Hume-Rothery mechanism [Hume-Rothery 26] is proved important for the stability of quasicrystals, too [Smith 87, Friedel 88]. A relation between the structure factor and the resistivity is given by the Faber-Ziman formula [Ziman 61, Faber 65],

$$\rho_Z = \sigma_Z^{-1} = \frac{3\pi}{4} \frac{\mathcal{N}}{\hbar e^2 v_F^2 k_F^4} \int_0^{2k_F} S(q)\, |w(q)|^2\, q^3\, dq \quad , \tag{3.2}$$

where $\underline{q}$ represent the scattering vector, $w(q)$ the Fourier transform of the effective-atom pseudopotential, and $S(q)$ the static structure factor. $\mathcal{N}$ and v_F are the atomic number density and Fermi velocity, respectively.

Then, due to q^3 in (3.2) and a pronounced peak of $S(q)$ close to $q = 2k_F$ a high resistivity is expected due to both constructive interference and nesting about back scattering. However, compared with amorphous phases, quasicrystals have a more pronounced peak at $2k_F$ [Roth 99, Haberkern 00a] due to long-range order. In consequence, the resistivity of quasicrystalline systems is higher [Roth 99]. Furthermore, in the framework of Ziman's formula (3.2), the temperature dependence is obtained when the static structure factor is replaced by the dynamic one [Baym 64]. Then, increasing the temperature, the electronically induced peak in the static structure factor at $q \simeq 2k_F$ reduces and the conductivity increases.

In summary, this formula provides a *qualitative* explanation of the influence of structural perfection on the electrical resistivity on account of the structure factor. The Faber-Ziman formula supposes the electron to occupy free-electron states and weak scattering. Hence, it gives no reliable quantitative results for systems containing d-orbitals of transition metals at the Fermi-level (strong scattering) which is the case for the more resistive quasicrystals (see [Berger 94]). Furthermore, the effect of multiple scattering is also not considered.

Two-band model

The experimental finding of sign reversal of the Hall coefficient [Haberkern 93] motivated the use of this simple model: negative/positive sign can be explained considering the presence of electrons/holes. This effect is consistent with the Hume-Rothery mechanism of stability [Hume-Rothery 26] that is fulfilled for quasicrystals [Smith 87, Friedel 88]. The touch between the Jones zone (generalization of the Brillouin zone for non-crystalline materials) and the Fermi surface in different directions produce electron and hole states [Haberkern 95]. Then, the transport coefficients, in the framework of the two-band model, can be described as the sum of electron and hole contributions. For instance, for the conductivity one can write,

$$\sigma = e^2 \left(\tau_e \frac{n_e}{|m_e^*|} + \tau_h \frac{n_h}{|m_h^*|} \right) \quad , \tag{3.3}$$

with the electron and hole densities n_e, n_h, the effective masses m_e^*, m_h^*, and the scattering times τ_e, τ_h.

This model was initially used with good agreement by Haberkern *et al.* [Haberkern 93, Haberkern 95] to explain experimental results of conductivity, Hall coefficient, and thermopower of the icosahedral Al-Cu-Fe phase. In that procedure temperature independent scattering times and effective masses were used. However, a strong temperature dependence of the carrier densities for holes and electrons, similar to the Debye-Waller factor, is required which is a serious drawback of this approach. There is no indication that carrier densities increase with temperature as known from the activation behavior of semiconductors or as a power law. Furthermore, for amorphous metals, the model is less convincing, because there is no definite touch between the Fermi surface and a Jones zone. Summarizing, the two-band model is rather a phenomenological approach.

Narrow-band model

Considering that approximants are periodic systems with large unit cells, the conductivity of low order approximants (e.g. see [Fujiwara 93b, Krajčí 97]) can be calculated using the Bloch-Boltzmann formula,

$$\sigma_{\alpha,\alpha} = e^2 \tau \left(\frac{n_e}{m_e^*} \right) = \frac{e^2 \tau}{\Omega_{cell}} \sum_{n,\underline{k}} v_{\alpha,n}(\underline{k})^2 \left(- \frac{df(\varepsilon,\mu,T)}{d\varepsilon} \right)_{\varepsilon=\varepsilon_n(\underline{k})} \quad , \tag{3.4}$$

where n is the band index, $v_{\alpha,n}(\underline{k}) = (1/\hbar)\,(\partial\varepsilon_n(\underline{k})/\partial k_\alpha)$ is the component along α of the velocity of the state $(n,\underline{k})$, $f(\varepsilon,\mu,T)$ is the Fermi-Dirac distribution function (A.9), τ is the relaxation time, and Ω_{cell} the unit cell volume. $\varepsilon_n(\underline{k})$ gives the dispersion relation. Fujiwara *et al.* [Fujiwara 93b, Trambly 94, Roche 98] and Krajčí *et al.* [Krajčí 97, Krajčí 98] employed this semiclassical Bloch-Boltzmann equation (3.4) with an *empirical* $\tau \sim 10^{-14}$-10^{-15}sec. The dispersion relation was calculated using the LMTO [Andersen 75] or TB-LMTO [Andersen 85] basis. Again, the electrons occupy ballistic states. Resistivity comes from defect/impurity scattering.

The following explanation [Fujiwara 93b] is given for the low conductivity of quasicrystals: from low to high order approximants the number of atoms per unit cell increases, that means, the number of bands increases. Moreover, due to strong hybridization effects between, for example, *sp*-Al and *d*-TM states the bands become flats, this guides to small velocities of the wave packets (Fermi velocity, $v_F \sim 0.5 \times 10^7 cm/s$, and large effective masses ($m_e^* \sim$ 2-10 m_e, [Fujiwara 93b]). In consequence, in the quasiperiodic limit the conductivity vanish. It is worth noting that defects in the system should allow finite conductivities.

However, the applicability of the Bloch-Boltzmann formula to quasicrystals has been criticized because the scaling properties of critical eigenstates [Sire 94, Yamamoto 95a, Fujiwara 96] lead to the expectation that the propagation of the electrons is neither ballistic as in the case of periodic systems nor diffusive as in the case of disordered systems.

Recently, Krajčí and Hafner [Krajčí 01] published a work where the conductivities of low order approximants of Al-Pd-(Mn/Re) are calculated by means of the Bloch-Boltzmann equation (3.4) and the Kubo-Greenwood formula (3.5). The resulting conductivities obtained differ seriously from one another. This indicates that the electronic diffusivity (3.8) provides additional information necessary to understand the transport. Equation (3.4) considers only the band dispersion.

3.2 Arbitrary electron states: the role of diffusivity

Mott g-factor governing the transport

The transport in systems which possess pseudogaps in the density of states around the Fermi energy can be characterized through the *so called* Mott g-factor [Mott 69]. Mott defined it as the ratio of the state density at the Fermi energy, n_F, over the corresponding free electron value. Then, when the scattering is weak, the transport should be governed by Boltzmann transport equations, (3.2), (3.4), but the conductivity must decreases as g^2 if the Fermi energy lies in the pseudogap. In fact, using the Einstein relation (3.8), and considering that the electronic diffusivity is proportional to the state density one gets to $\sigma \propto n_F^2 \propto g^2$.

Mizutani investigated experimentally [Mizutani 98], employing the low temperature coefficient of the electronic specific heat, $\gamma_{sh} = (\pi k_B)^2 n_F/3$, as an indicator of n_F, the role of pseudogaps in the electronic transport of quasicrystals and their related approximants and amorphous phases. He shows that the Mott theory is valid, i.e. the conductivity changes in proportion to the square of the state density, when the temperature is around 300 K (room temperatures). However, at low temperatures, he shows that, as the relation conductivity-pseudogap is concerned, three different groups can be found: the *sp*-type quasicrystals, the *spd*-type quasicrystals, and i-Al-Pd-Re samples of high quality.

The last two groups contain transition metals with atomic d orbitals at the Fermi level. It seems that *sp*-*d* hybridization plays an important role in the electronic transport of quasicrystals containing transition metals. A detailed experimental analysis of the importance of transition metals in quasicrystals was carried out by Lindqvist *et al.* [Lindqvist 93]. The authors find for concentration differences of 0.5 at. % Fe changes in the conductivity from 100 $(\mu\Omega cm)^{-1}$ to 250 $(\mu\Omega cm)^{-1}$.

Here, the Kubo-Greenwood formula (3.5) will be employed taking into account hybridization effects. The results, presented in the following chapters, show that not only the amount of participating states but also the kind of the states are important to determine the metallic or non-metallic character of the material under study. For instance, the studied crystalline materials have very low resistivities due to their high diffusivity, whereas approximants of quasicrystals with similar state densities are very resistive due to the low diffusivity of their electronic states.

Kubo-Greenwood Formula

The transport equations described in the previous section, (3.2), (3.3), and (3.4), are not successful when the electron mean free path is of the order of atomic diameter (see for instance [Mott 87]). That means, the electron is not ballistic and the assumption of single scattering fails. On the other hand, theoretical studies in quasicrystals indicate that electrons can not be considered as ballistic [Sire 94, Fujiwara 96]. Moreover, experiments [Lindqvist 93, Mizutani 98] show that hybridization effects on the conductivity are important.

In such cases, the Kubo-Greenwood formula [Kubo 57, Greenwood 58] is one way to calculate the conductivity. This formula, in difference to Boltzmann formulas, makes no assumptions on the character of the states. It asks for both, the *amount* and *character* of the states available for the transport. Moreover, this formula takes into account multiple scattering [Asano 80, Butler 85] and describes correctly the effect of hybridization with atomic d-orbitals in the transport properties. In summary, the Kubo-Greenwood formula provides a quantum mechanical treatment of the electronic transport within the one-particle approximation. In the following, this formula will be presented, as well as, its relation with the electronic diffusivity.

In the framework of the linear response theory, the electrical conductivity of a system can be calculated with the Greenwood form [Greenwood 58] of the Kubo formula [Kubo 57]. A brief deduction will be presented in appendix A.1. The frequency zero limit of the optical conductivity gives the temperature dependent electrical dc-conductivity, see equation (A.5), which is calculated from the spectral conductivity,

$$\widehat{\sigma}_{\mu,\mu}(\varepsilon) = 2\frac{\pi\hbar e^2}{\Omega} \sum_{i,j} |\langle i|v_\mu|j\rangle|^2 \, \delta(\varepsilon-\varepsilon_i) \, \delta(\varepsilon-\varepsilon_j) \quad , \tag{3.5}$$

where $|i\rangle$ is the electronic wavefunction with the energy eigenvalue ε_i. The prefactor 2 consider both spin-components, Ω is the volume of the system and $v_\mu = \hbar/(im_e)\partial/\partial\mu$ is the μ-component of the velocity operator. Hereafter $\widehat{\sigma}(\varepsilon) \equiv \widehat{\sigma}_{\mu,\mu}(\varepsilon)$ will be used for the spectral conductivity with $\mu = z$. Other cases will be explicitly mentioned.

Two points are to be mentioned in reference to equation (3.5): i) as shown in appendix A.1, $\widehat{\sigma}(\varepsilon_F)$ is the zero temperature limit of the dc-conductivity (A.5), and ii) the two delta functions evaluated at the same energy ε indicate that the transport is confined on-the energy-shell ε.

Numerical calculations require to broaden the delta functions in (3.5), because only small systems are feasible where the level density is quite low. Gauss functions,

$$\delta(\varepsilon - \varepsilon') \to \frac{1}{\Sigma\sqrt{2\pi}}\, exp\left\{-\frac{(\varepsilon-\varepsilon')^2}{2\Sigma^2}\right\} \quad , \tag{3.6}$$

or Lorentz functions,

$$\delta(\varepsilon - \varepsilon') \to \frac{1}{\pi}\frac{\Gamma}{(\varepsilon-\varepsilon')^2+\Gamma^2} \quad , \tag{3.7}$$

are the most appropriate functions (the delta functions are recovered in the limit $\Sigma, \Gamma \to 0$).

On the other hand, the half-width Γ (Σ) also simulates thermally inelastic scattering. The transporting states are not longer confined to the energy shell ε but rather to an energy window of the width 2Γ around ε. Hence, one can relate Γ with the temperature by means of $2\Gamma \simeq k_B T$. Finally, it is important to mention that the election of Γ must be made careful: it must be much larger than the averaged level spacing, $\delta\varepsilon$. At a fixed energy, the unphysical region, $\Gamma < \delta\varepsilon$, is characterized by $\sigma \propto \Gamma^2$ due to the product of the two delta (Lorentz) functions in (3.5).

The electronic diffusivity can be calculated employing the Einstein relation,

$$\widehat{D}^{-1}(\varepsilon) = 2\,\frac{e^2}{\Omega}\widehat{n}(\varepsilon)\widehat{\rho}(\varepsilon) \quad , \tag{3.8}$$

where $\widehat{\rho}(\varepsilon) = \widehat{\sigma}^{-1}(\varepsilon)$ is the spectral resistivity and $\widehat{n}(\varepsilon)$ is the density of states.

Calculations of $\widehat{\sigma}(\varepsilon)$ employing the Kubo-Greenwood formula for s-band tight-binding quasicrystalline models including disorder [Roche 97a] and for realistic low order approximants of quasicrystals [Fujiwara 96, Roche 98] indicate the importance of scaling with scattering time in quasiperiodic systems. However, in a recent work Krajčí and Hafner show [Krajčí 01] that the conductivity decreases in the limit of both small and large scattering time, moreover, they found a stationary behavior over a wide range of intermediate values which is in disagreement with the analysis for the diffusivity carried out by Fujiwara *et al.* [Fujiwara 96]. In this sense, more detailed studies are necessary.

Small τ: interband hopping

Transport mechanisms related to anomalous diffusion are governed by low or large disorder regimes, respectively, large or short relaxation times τ. These mechanisms go beyond the Bloch-Boltzmann theory, as will be seen below. For short τ, collision events can induce interband transitions (hopping) between electronic eigenstates (critical states). In fact, following [Roche 97b], a limit for the largest lifetime is given by $\Delta\epsilon$, the bandwidth for a given scale L. If the scattering time, induced by disorder (static, phonons), is $\tau \ll \hbar/\Delta\epsilon$ then, the diffusivity, $D = (1/3)L(\tau)^2/\tau$, depends on it as $D \propto 1/\tau$ because of L will not depend anymore on τ (fixed bandwidth). Hence, from the Einstein relation (3.8), the conductivity is $\sigma \propto 1/\tau$ which explain qualitatively the inverse Matthiessen rule (3.1). As was pointed out by Roche *et al.* [Roche 97b], due to the almost dispersionless bands in quasicrystals, this transport mechanism should apply even to small disorder.

Large τ: anomalous diffusion

For large τ, the electronic wave packet propagates between two scattering events as in the perfect quasiperiodic structure. Indeed, numerical calculations in perfect quasiperiodic structures show [Passaro 92, Sire 94] that the wave packet spreads with an anomalous diffusion law $L(t) \propto t^\beta$ ($0 < \beta < 1$, $\beta = 0.5$ means normal diffusion). If $\tau \gg \hbar/\Delta\epsilon$ then, the electronic diffusivity is $D = (1/3)L^2(\tau)/\tau \propto \tau^{2\beta-1}$, which gives, after employing the Einstein relation (3.8), the so-called *anomalous Drude conductivity* [Mayou 94, Sire 94, Bellissard 95],

$$\sigma \propto \tau^{2\beta-1} \quad . \tag{3.9}$$

The normal Drude conductivity is recovered for $\beta = 1$ (ballistic transport). On the other hand, provided that $\beta < 0.5$ the transport is sub-diffusive and the conductivity will decrease with increasing τ, which explains qualitatively the inverse Matthiessen rule (3.1).

The parameter Γ employed in (3.7) can be related via $2\Gamma\tau \simeq \hbar$ to a finite lifetime, τ, of the electronic eigenstates due to disorder (defects, impurities, phonons). Thus, equation (3.9) becomes,

$$\sigma \propto \Gamma^{1-2\beta} \quad . \tag{3.10}$$

This provides another interpretation of Γ.

Calculations on realistic approximant models of d-Al-Cu-Co quasicrystals show that $\beta \simeq 0.375$ [Fujiwara 96, Roche 98]. Provided that the Bloch-Grüneisen law, $\tau \propto T^{-5}$, holds [Fujiwara 96, Roche 98], which is due to the electron-phonon coupling, one obtains in (3.9) $\sigma(T) \propto T^{5(1-2\beta)} = T^{1.25}$. This result is compatible with experiments [Gignoux 97, Tamura 97, Lalla 95] which show such behavior also for high temperatures, up to 1000 K.

However, the Bloch-Grüneisen law is obtained under the consideration of a phononic Debye-spectrum. The different contributions of longitudinal and transversal modes can modify the T^{-5}-dependence of τ. Moreover, this law is valid only for temperatures far below the Debye temperature. For quasicrystals the Debye temperature is experimentally estimated to be 400-500 K [Martin 91, Pierce 93b]. For high temperatures the electron-phonon contribution gives $\tau \propto T^{-1}$ which cannot explain the experiments, as was pointed out by Bellissard [Bellissard 00]. Hence, the question of the transport mechanism at high temperatures remains open.

In the present work it will be confirmed, employing (3.5), (3.7), and (3.10) in realistic approximant models, that the electronic transport of icosahedral quasicrystals should be sub-diffusive ($\beta < 1/2$). Furthermore, it will be shown that the temperature dependence of the conductivity can be calculated without the use of the Bloch-Grüneisen law. These results are in good agreement with experiments up to temperatures of 600 K (for i-Al-Cu-Fe and i-Al-Cu-Ru) and 900 K (for i-Al-Pd-Re).

3.3 Variable range hopping transport and quantum corrections to the conductivity

Variable Range Hopping

Mott employed a simple approximation for the spectral conductivity [Mott 87],

$$\widehat{\sigma}(\varepsilon) = \left\{ \begin{array}{ccc} 0 & \texttt{for} & \varepsilon < \varepsilon_c \\ \sigma_{min} & \texttt{for} & \varepsilon \geq \varepsilon_c \end{array} \right. , \tag{3.11}$$

where ε_c is known as the *mobility edge*, and the constant $\sigma_{min} \simeq (0.03e^2/\hbar)(1/\xi_c)$ is the so called *minimum metallic conductivity* (ξ_c is the localization length for an electronic wave function at $\varepsilon < \varepsilon_c$). The energy ε_c separates the localized from the delocalized states. At low temperatures ($\mu(T) \approx \varepsilon_F$), with the Fermi energy below the mobility edge ($\varepsilon_c - \varepsilon_F > 0$), the simplified spectral conductivity (3.11) provides, employing (A.5), the *thermally activated conductivity*,

$$\sigma(T) = \sigma_{min}\ exp\left\{ -\frac{(\varepsilon_c - \mu)}{k_B T} \right\} . \tag{3.12}$$

Via thermal excitation, the electrons are lifted from localized states roughly at the chemical potential μ to the mobility edge.

Variable-range hopping, VRH, on the contrary, does not include the states above the mobility edge. It is rather the hopping between states which are localized about different positions in real space. At low temperatures, the energy difference between the participating localized states is very small, that means, the electron must jump to a state which is localized at a quite distant site. In that case the average distance of hopping depends on the temperature. Following Mott [Mott 87], we have

$$\sigma(T) = \sigma_0\ e^{-(T_0/T)^{1/4}} \tag{3.13}$$

where $T_0 \simeq (24\alpha_c^3)/(\pi k_B \widehat{n}(\varepsilon_F))$ with α_c^{-1} the decay length of the localized wave functions.

As yet, the surprisingly low conductivity of i-Al-Pd-Re quasicrystalline alloys at low temperatures is not well understood. It is reported that these samples achieve conductivities about three orders of magnitude smaller than Mott minimum metallic value. For instance, at 0.45 K, the conductivity is approximately $0.05(\Omega cm)^{-1}$ [Pierce 94]. These values are right in the range of systems in the insulating side of the metal-insulator transition such as Al-Al_2O_3 [Sin 84], $In_2O3 - x$ [Frydmann 95], and MoGe [Yoshizumi 88], for instance. However, for an insulator the density of carriers of i-Al-Pd-Re samples is rather high, of the order of $\sim 10^{20} cm^{-3}$.

Variable range hopping conduction has been reported [Guo 96] for i-$Al_{70.5}Pd_{21}Re_{8.5}$ samples. On adding less than 3% Mn, a metallic state is created [Guo 96]. These samples give a zero conductivity after extrapolations from temperatures above 0.45K to zero Kelvin. Similarly, Delahaye found [Delahaye 00] a variable range hopping conductivity studying i-Al-Pd-Re samples in temperature ranges of 20mK to 60mK. The conductivity extrapolates also to zero at zero Kelvin. However, the experimental results of Bianchi *et al.* [Bianchi 97] and Ahlgren *et al.* [Ahlgren 97a] for temperatures down to 40mK suggest, after extrapolations, a finite conductivity at zero Kelvin. **The question of insulating i-Al-Pd-Re remains open**.

Quantum corrections to the conductivity

Quantum effects, such as weak localization and enhanced electron-electron interaction, have been proved important for the conductivity of quasicrystals [Rapp 99]. Weak localization is due to one electron interference effects, whereas electron-electron interaction is due to interference between two scattered electrons. These quantum effects become important at very low temperatures producing quantum corrections to the conductivity.

From the experimental point of view, the magnetoresistance can give evidences of quantum interference effects: $\Delta\sigma(B) = \sigma(B) - \sigma(B=0) \propto \sqrt{B}$ with B the magnetic field, and $\Delta\sigma(T) \propto \sqrt{T}$ or $\Delta\sigma(T) \propto T$ [Klein 92, Berger 94]. Moreover, experiments show that the magnetoresistance becomes anomalously large at low temperatures [Klein 92, Sahnoune 92, Ahlgren 97b]. Thus, the magnetoresistance falls into two groups (see [Rapp 99] and references therein): quasicrystals with resistivities lower than $10^5 \mu\Omega cm$, and i-Al-Pd-Re samples. For the first group, the temperature and magnetic dependence of the magnetoresistance can be described by theories that consider weak localization and electron-electron interaction. For i-Al-Pd-Re samples, the magnetoresistance can not be described by quantum corrections. This is expected because, for example, weak localization is not justified for materials with very high resistivities.

On the other hand, studies by Lin *et al.* [Lin 96] in i-$Al_{70}Pd_{22.5}(Re_{1-x}Mn_x)_{7.5}$ samples show that the conductivity behaves as $\sigma(T) = \sigma(0)(1 + \sqrt{T/\Delta})$ with Δ temperature equivalent of the correlation gap. This behavior is typical of interacting disordered electrons [Grest 83]. Furthermore, this temperature dependence of $\sigma(T)$ shows that the inverse Matthiessen rule (3.1) breaks down when quantum corrections become important (very low temperatures), as was discussed in [Madel 00].

However, when $\Delta \simeq \sigma(0)^2$ the inverse Matthiessen rule is assured as demonstrated by [Lin 96].

Chapter 4

Spectral fine structure and anomalous transport

The features of the electronic density of states can explain the electronic transport. In fact, if one expects that the electronic diffusivity remains unchanged with the energy or if it scales just as the state density, then, using the Einstein relation, equation (3.8), the features of the state density around the Fermi energy can be extrapolated to the spectral conductivity and hence to the transport coefficients (the last correspondence is discussed in appendix A). In this sense, to understand the *anomalous* transport properties of quasicrystals it is necessary to know the behavior of the state density around the Fermi energy. In the following, we will review the state density features and consequences for the transport of quasicrystalline materials.

4.1 Pseudogap in the density of states

One of the first discovered properties of icosahedral quasicrystals is that these materials are Hume-Rothery phases, i.e. electronically stabilized phases [Bancel 86, Tsai 89]. That means, from the interaction between the Fermi surface and the Jones zone results a minimum in the density of states (*pseudogap*), at the Fermi energy. Models of icosahedral alloys within the nearly free electron approximation confirm [Smith 87, Friedel 88, Friedel 92] the existence of such pseudogaps. Band structure calculations of approximants predict the existence of a structure-induced pseudogap at the Fermi energy in many icosahedral alloys [Fujiwara 89, Fujiwara 91, Hafner 92, Hafner 93, Windisch 94, Trambly 94, Krajčí 95]. This pseudogap is enhanced by the hybridization of *sp* and *d* orbitals [Trambly 95].

From experiments, the low temperature coefficient of the electronic specific heat, γ_{sh}, which is proportional to the state density at the Fermi energy, is low in comparison with the estimated free electron value, γ_{sh}^{free}. For instance, 1/3 and 1/10 of γ_{sh}^{free} in i-Al-Cu-Fe [Klein 91, Pierce 93a], and in i-Al-Cu-Ru [Biggs 90], respectively. However, contrarily to the conductivity, only a weak composition dependence is found [Pierce 93a] for γ_{sh}. This indicates that the electronic diffusivity should clearly depend on both the composition and, in a rigid band model, the energy in order to provide the observed strong composition dependence of the conductivity [Lindqvist 93].

On the other hand, by means of spectroscopic techniques, such as photoemission spectroscopy, inverse photoemission spectroscopy, and soft x-ray emission and absorption, one can obtain information of the density of states below, above, and at the Fermi energy. Employing these experimental techniques a wide pseudogap of the order of ∼1 eV was found [Belin 91, Belin 92, Mizutani 94, Stadnik 95, Stadnik 99]. However, this wide pseudogap is believed to exist in both crystalline [Carlsson 95, Trambly 95] and amorphous [Häussler 92] materials. That means, the wide pseudogap around the Fermi energy is important for the stability of quasicrystals. However, the *anomalous* transport properties can not be due.

4.2 Spikiness and fine structure of the density of states

Ab-initio calculations of the density of states of approximants provide many very fine spiked peaks with a width of about 10 meV, distributed over the whole valence band [Fujiwara 89]. These special features of the state density should result from the huge amount of almost dispersionless bands. Spiky state density features were obtained from many band-structure calculations for realistic approximant models of quasicrystals [Fujiwara 89, Fujiwara 91, Hafner 92, Windisch 94, Trambly 94, Krajčí 95]. This should be augmented by the presence of transition metals due to hybridization effects between *sp* and *d* orbitals [Trambly 94].

The spiked state density may explain the unusual sensitivity of the electrical conductivity to slight composition changes. Fujiwara *et al.* argued [Fujiwara 93b] that such composition changes shift the position of the Fermi energy, which results in a dramatic change of the state density at the Fermi energy, and consequently of the conductivity value. It is also shown [Fujiwara 93b] that this spiked density of states can explain *qualitatively* the composition and temperature dependence of other transport coefficients, such as the thermopower, Hall and, optical conductivities. As yet, however, the existence of spikes is not experimentally confirmed and some authors suggest that spikes should be an artifact of the calculation [Stadnik 97, Haerle 98] or only specific for small periodic approximants of quasicrystals [Hafner 92, Zijlstra 00].

Another kind of fine structure is predicted by a model of quasicrystal growth, proposed by Janot and de Boissieu [Janot 94], based on the hierarchical selfsimilar packing of atomic clusters. As a consequence of this model, the electron state density should also show [Janot 94] a hierarchical selfsimilar structure with spiky features in the pseudogap. According to this model the pseudogap is asymmetric and centered at the Fermi energy. In the limit of the selfsimilar packing process, the density of states at the Fermi energy is zero [Janot 97]. Hence, the conductivity should be due to variable-range hopping, equation (3.13), with appropriate alterations [Janot 96, Janot 97] for the hopping probability. He shows [Janot 97] that $\sigma(T) \simeq T^{\alpha}$, the Hall coefficient $R_H(T) \simeq -T^{-\alpha}$, and the electronic thermal conductivity $K(T) \simeq T^{\alpha+1}$. For the i-Al-Pd-Mn quasicrystal, $\alpha = 1.43$ is found [Janot 97]. However, to keep the density constant, overlap between clusters is needed at some selfsimilar packing stage [Janot 97] which should give *unphysically* short distances between some atoms. Moreover, real quasicrystals do not contain only clusters but also other atoms (glue atoms) or joining portions that do not belong to either cluster. These new requirements should change the electronic distribution and hence the behavior of the electronic transport.

Experiments on nuclear magnetic resonance [Tang 97] and tunneling spectroscopy [Escudero 99, Guohong 99] have revealed spectral features on energy scales down to a few 10 meV. These features have been explained using McMillan's scaling theory [McMillan 81], which includes both electron-electron interactions and localization effects. However, the scaling theory predicts a singularity in the state density at the Fermi energy, leading, as the temperature goes to zero, to localization in the system, and consequently the formation of a correlation gap. This is not the case for quasicrystals: the spectral features of the state density at ∼50 meV out of the Fermi energy are well described with the scaling theory [Davydov 98, Escudero 99]. But, within the 50 meV window around the Fermi energy, the scaling theory breaks down. From experiments [Tang 97, Escudero 99, Guohong 99] one finds always a finite density of states at the Fermi energy. On the other hand, experiments [Tang 97, Escudero 99, Guohong 99] only indicate the existence of a symmetric narrow pseudogap around the Fermi energy. There is no evidence of a spiked density of states over the *whole* valence band. That means, the real origin of these fine spectral features is matter of further discussions.

On the other hand, if one adopts that transport quantities can be expressed in terms of the kinetic coefficients and hence the spectral conductivity (see appendix A), the features of these quantities can give indirect information of spectral properties. Most evidently the thermopower provides such information (c.f. Mott formula, equation (6.6)). In fact, experiments of the thermopower, Hall coefficient, optical, and thermal conductivities indicate the presence of fine structure on the spectral conductivity. The thermopower has large values and strong temperature dependence. In icosahedral quasicrystals of high structural quality, the thermopower can change its sign with temperature [Roth 99, Pierce 93a] and with slightly different annealing treatments [Haberkern 95]. The Hall coefficient depends also extremely on the temperature and small composition changes [Pierce 93a, Lindqvist 93]. Normally, but not always, it is found experimentally [Poon 92] that the signs of the Hall coefficient and the thermopower are correlated. Similarly, the composition dependences of the Hall coefficient and the conductivity are correlated [Lindqvist 93, Haberkern 00a]. It is also observed [Poon 92, Pierce 93a] that this peculiar behavior of the thermopower and the Hall coefficient can be *qualitatively* explained considering a state density (respectively, spectral conductivity) minimum of width ∼200 meV around the Fermi energy.

Furthermore, very low thermal conductivity, e.g. for i-Al-Cu-Fe the thermal conductivity is two orders of magnitude lower than in fcc-Al [Perrot 95], and the absence of the Drude peak on the optical conductivity [Homes 91, Basov 94a], common for metals, are found experimentally. This indicates that only small number of carriers, i.e. low density of state at the Fermi energy, are available for the transport.

4.3 The concept of this work

Quasicrystals and related approximants have similar local order. Interesting is that the electronic transport properties in quasicrystals and approximants are quite similar [Poon 92, Berger 94]. Such similarities were also found in thermal [Dubois 92] and optical [Basov 94a] conductivities. **Consequently, it seems that the local environment, e.g. ∼10-20 Å [Berger 94, Trambly 97], should play a key role in the transport properties of icosahedral quasicrystals and approximants**.

On the other hand, it is known that clusters, such as the Mackay and Bergman icosahedra, are the basic elements to build both icosahedral approximants and quasicrystals (for a review see, for instance, [de Boissieu 94, Boudard 99]). **Hence, one can expect that these clusters, their decoration, and their arrangement on scales of ∼10-20 Å, are responsible for the spectral features that can account for the *anomalous* transport properties of approximants and quasicrystals discussed in chapter 3**. In this sense, it should be possible to search for such spectral features in approximants with unit cells larger than 10 Å.

The idea of this work is as follows. One can try to make a model for the spectral resistivity of a small approximant which reasonably reproduces the *ab-initio* results. Thus, this model must consider the important spectral features of the basic cluster, its decoration, and its arrangement in the unit cell. **In view of a related quasicrystal one can hope that, after fitting the model parameters to a few reliable experimental data, other experimental findings can be explained within this model**.

This kind of procedure will be presented in chapter 6 for the i-Al-Cu-Fe quasicrystal. The *ab-initio* results show that these spectral features are of the order of ∼100 meV, and they depend strongly of the chemical decoration and the arrangement of the clusters in the structure. Moreover, the modeled spectral resistivity can explain *consistently* the transport coefficients, such as the conductivity, thermopower, Hall coefficient, and the electronic thermal conductivity. This procedure is also applied to i-Al-Cu-Ru and i-Al-Pd-Re in good agreement with experiments.

Chapter 5

Methods for valence spectral fine structures

The question is, which methods can be employed to account for the density of states and/or the spectral conductivity. Two different concepts can be expected to explain the *anomalous* transport of quasicrystals. The first one considers the extended quasiperiodicity, i.e. long-range quasiperiodic order, more important than the chemical decoration (neglected in the corresponding models). The second one, on the other hand, puts the weights viceversa, i.e. the local chemical environment (20Å scale) is believed more important than extended quasiperiodicity. In the following, limitations and advantages of both concepts will be discussed.

5.1 Extended quasiperiodicity

The term extended quasiperiodicity is here applied to characterize a method that can describe quasiperiodic systems for itself and/or very high order approximant models. In these cases, a *tight binding Hamiltonian* is employed. This Hamilton operator is represented in an orthonormal LCAO-basis (linear combination of atomic orbitals), and is written as,

$$H \;=\; \sum_{n} \, |n\rangle \, \varepsilon_n \, \langle n| \; + \; \sum_{n \neq m} \, |n\rangle \, t_{nm} \, \langle m| \quad , \tag{5.1}$$

where, $\varepsilon_n = \langle n|H|n\rangle$ is the site energy and $t_{nm} = \langle n|H|m\rangle$ is the hopping term, that is different from zero only for the nearest-neighbour sites. This Hamiltonian considers only one s-type orbital per atomic site. Moreover, as was mentioned previously, the chemical aspects are not taken into account. That means, the Hamiltonian (5.1) can be seen as an one-component system. Quasicrystals, on the other hand, are at least two component systems. However, the *tight-binding* Hamiltonian is able to study the influence of long-range quasiperiodicity on the electronic properties, and this is not possible with present *ab-initio* methods, see next section.

The Hamiltonian (5.1) is a very simple description of electrons in different topological environments. For instance, quasiperiodicity is given by the corresponding quasiperiodic sequence of ε_n and/or t_{nm} [Kohmoto 83, Kohmoto 86]. The periodic limit can be obtained when $\varepsilon_n = \varepsilon$, and $t_{nm} = t$ are fixed constants $\forall n, m$. The Anderson Hamiltonian model [Anderson 58] of disordered systems is also obtained from (5.1), for example, with random elections of ε_n and/or t_{nm}. Thus, the electronic properties of crystals and quasicrystals can be easily compared. Moreover, the influence of disorder in quasicrystals can also be studied, for example, changing some site-energies *randomly* [Roche 97a].

Employing the Hamiltonian (5.1) different quasicrystals models were studied. The Fibonacci chain, as an one dimensional quasicrystalline model, shows a singular-continuous and multifractal energy spectrum [Kohmoto 87]. All electronic wave functions of the Fibonacci chain are critical, i.e. the wave function envelopes are power-law function. For certain energies, the conductance behaves [Kohmoto 86] as $G \simeq L^{-\alpha}$, where L is the sample length, and $0 < \alpha < 1$. This behavior of the conductance is related [Kohmoto 86] to the critical nature of the wave functions. For comparison, $G \simeq exp(-\gamma L)$, and $G \simeq L$ correspond to Anderson localization, and Ohmic-law behavior, respectively.

The Penrose tiling is the most common two dimensional quasicrystalline model. In Penrose lattices, the wave functions are also critical [Yamamoto 95b]. Moreover, very special states, called *confined states*, are found [Fujiwara 88]. These states have finite amplitudes only at special tiling regions and vanish outside. The conductance of a two dimensional Penrose tiling shows a power-law dependence [Tsunetsuga 91]: $G \simeq L^{-\nu}$, where $\nu \simeq$ 0.2-0.3. Studies of elementary excitations, such as electrons, phonons, and excitons, in low dimensional aperiodic systems, have been carried out by different authors, the interested reader is referred to [Maciá 00c].

Three dimensional Penrose tilings, with icosahedral symmetry, have also been studied. Rieth found [Rieth 95] that the localization tendency decreases on increasing the order of the approximant. He concludes i) that quasiperiodicity does not necessarily cause the localization of the electronic states, and ii) that quasiperiodicity does not influence the metal-insulator transition. Zijlstra found [Zijlstra 01] that, i) spikes in the density of states, discussed in the previous chapter, which occur in low order approximants may not survive in the quasiperiodic limit, and ii) the conductivity should increases after increasing the order of the approximant, and consequently, the unit-cell size of the lattice.

However, these results can not be compared with experiments. It seems that quasiperiodicity alone is not able to reproduce the transport properties observed experimentally. Zijlstra pointed out [Zijlstra 01] that probably a combination of quasiperiodicity and another mechanism is needed. In the present work, the local chemical order, ~10-20 Å, is proposed as the complementary mechanism to explain the experiments. This point will be discussed in the following section.

5.2 Chemical sensitivity

With the tight-binding Hamiltonian model, (5.1), the quasicrystal is described as a quasiperiodic one-component system. This implies two limitations that can hinder to reproduce the properties of realistic quasicrystals. Namely, it considers only nearest-neighbour interactions, and only one s-type orbital per site. It was proved [Trambly 97, Solbrig 00a], in icosahedral quasicrystals and approximants, that long-range electronic interferences in the transition metal sub-systems give rise to narrow spectral features which are highly important for the electronic transport. Moreover, hybridization effects between sp and d orbitals are important for the stability [Trambly 95] and for the transport [Lindqvist 93]. This indicates that to describe realistic approximants and/or quasicrystals is necessary to consider more than one component and more than one orbital.

The linear muffin-tin orbital method, LMTO, its tight-binding version, the TB-LMTO method, and the muffin-tin scattered wave method, MTSW, are *ab-initio* methods that work for more than one-component systems and consider hybridization effects. These *ab-initio* methods are employed in supercell or recursion approaches. They can be employed as $\underline{k}$-space methods or, combined with recursion procedures, as $\underline{r}$-space techniques. Thus, the use of approaches in both spaces provides us the possibility to search for common spectral fine structures that are not artifacts of the procedures.

The main limitation of these *ab-initio* methods lie on the number of atoms supported for numerical calculations. In the LMTO supercell method, it is limited to ~250 atoms. Recursion methods combined with TB-LMTO and the MTSW work with clusters of the order of ~1000 and ~5000 atoms, respectively. However, as was discussed in section 4.3, if one expects that the local chemical order, ~ 10-20Å, provides the necessary information to describe the electronic transport of quasicrystals then, these *ab-initio* methods can be successfully employed.

In the following will be presented the *ab-initio* methods employed in this work to search for spectral fine structures in the density of states and the spectral conductivity of realistic low order approximants. Furthermore, the Landauer/Büttiker approach is employed to calculate conductances of quasi one-dimensional systems.

LMTO-ASA supercell method

It is not the purpose of this work to enter into the details of the LMTO basis. For that reason, in the following will only be given a brief description of the construction of this basis[1].

---

[1] A brief deduction of the LMTO basis is given in appendix B.1. A complete and detailed explanation of the LMTO method can be found in [Andersen 84a, Andersen 85, Skriver 84, Andersen 87, Tank 00].

Thanks the <u>d</u>ensity <u>f</u>unctional <u>t</u>heory[2], DFT, the problem of many electrons moving in the potential of a set of fixed nuclei can be reduced to an equivalent one in which the electrons are non-interacting. Hence, the one-electron (non-interacting) Schrödinger equation, also called Kohn-Sham equation, can be written as,

$$\left\{ -\frac{\hbar^2}{2m_e}\nabla^2 + V_{eff}(\underline{r}) \right\} \Psi_i(\underline{r}) = \varepsilon_i \Psi_i(\underline{r}) \quad , \tag{5.2}$$

where $V_{eff}(\underline{r})$ is an effective potential [Kohn 65] that depends on the charge density,

$$n(\underline{r}) = e \sum_i^{occ} |\Psi_i(\underline{r})|^2 \quad . \tag{5.3}$$

Equation (5.2) must be solved self-consistently with $V_{eff}(\underline{r})$ because it depends on the wave functions through $n(\underline{r})$, equation (5.3).

The LMTO method provides an efficient scheme to realize this. The idea is to divide the space into atomic polygons for which the Schrödinger equation can be solved, and then the solutions can be connected with the corresponding boundary conditions. The muffin-tin potential is a good approximation to $V_{eff}(\underline{r})$. It divides the space into non-overlapping spheres centered at the atomic sites $\underline{R}$ with radii $S_{\underline{R}}^{MT}$ and the remaining interstitial region, see figure (5.1). Then, the muffin-tin potential of the atomic polygon $\underline{R}$ with the nuclear charge $Z_{\underline{R}}$ is written as,

$$V_{\underline{R}}(r_{\underline{R}}) = \begin{cases} -\dfrac{2Z_{\underline{R}}}{r_{\underline{R}}} + V_{\underline{R}}^{H}(r_{\underline{R}}) + V_{\underline{R}}^{M} + V_{\underline{R}}^{xc}(r_{\underline{R}}) - V_0^{MT} & \texttt{for} \quad r_{\underline{R}} \le S_{\underline{R}}^{MT} \\ 0 & \texttt{for} \quad r_{\underline{R}} > S_{\underline{R}}^{MT} \ , \end{cases} \tag{5.4}$$

where, $r_{\underline{R}} \equiv |\underline{r}_{\underline{R}}|$ with $\underline{r}_{\underline{R}} \equiv \underline{r} - \underline{R}$. Equation (5.4) contains for $r_{\underline{R}} \le S_{\underline{R}}^{MT}$ the screening potential of the electrons, $V_{\underline{R}}^{H}(r_{\underline{R}}) = \int d^3\underline{r}\ 2n(\underline{r}')/|\underline{r} - \underline{r}'|$ (Hartree potential), the Madelung potential, $V_{\underline{R}}^{M} = -\sum_{\underline{R}' \neq \underline{R}} 2Q_{\underline{R}'}/|\underline{R}' - \underline{R}|$ ($Q_{\underline{R}}$ is the effective charge of the sphere $\underline{R}$), the exchange-correlation potential[3], $V_{\underline{R}}^{xc}(r_{\underline{R}})$, and the nuclear potential, $-2Z_{\underline{R}}/r_{\underline{R}}$. Furthermore, the constant V_0^{MT} is the average of all potentials in the interstitial region.

To reduce the influence of the potential in the interstitial region one can use the <u>a</u>tomic <u>s</u>phere <u>a</u>pproximation, ASA, which employs overlapping spheres with radii $S_{\underline{R}}^{WS}$, see figure (5.1). These new spheres are also called Wigner-Seitz spheres because they fill the volume Ω_{cell}. Then

$$\Omega_{cell} = \sum_{\underline{R}}^{N_c} \Omega_{\underline{R}} \equiv \frac{4\pi}{3} \sum_{\underline{R}}^{N_c} (S_{\underline{R}}^{WS})^3 = N_c\, \frac{4\pi}{3} w^3 \quad , \tag{5.5}$$

---

[2] For a review of the density functional theory see the work of Jones and Gunnarsson [Jones 89].

[3] The exchange-correlation potential is a result of the DFT [Hohenberg 64, Kohn 65]. The exact functional form is unknown. However, under the <u>l</u>ocal <u>d</u>ensity <u>a</u>pproximation, LDA (see [Jones 89]), one can calculate it as a function of the charge density [Barth 72].

where $\Omega_{\underline{R}}$ is the volume of the atomic polygon, and N_c and w are the number of atoms in the unit-cell and the average Wigner-Seitz radius, respectively. Thus, the interstitial region is reduced to volume zero.

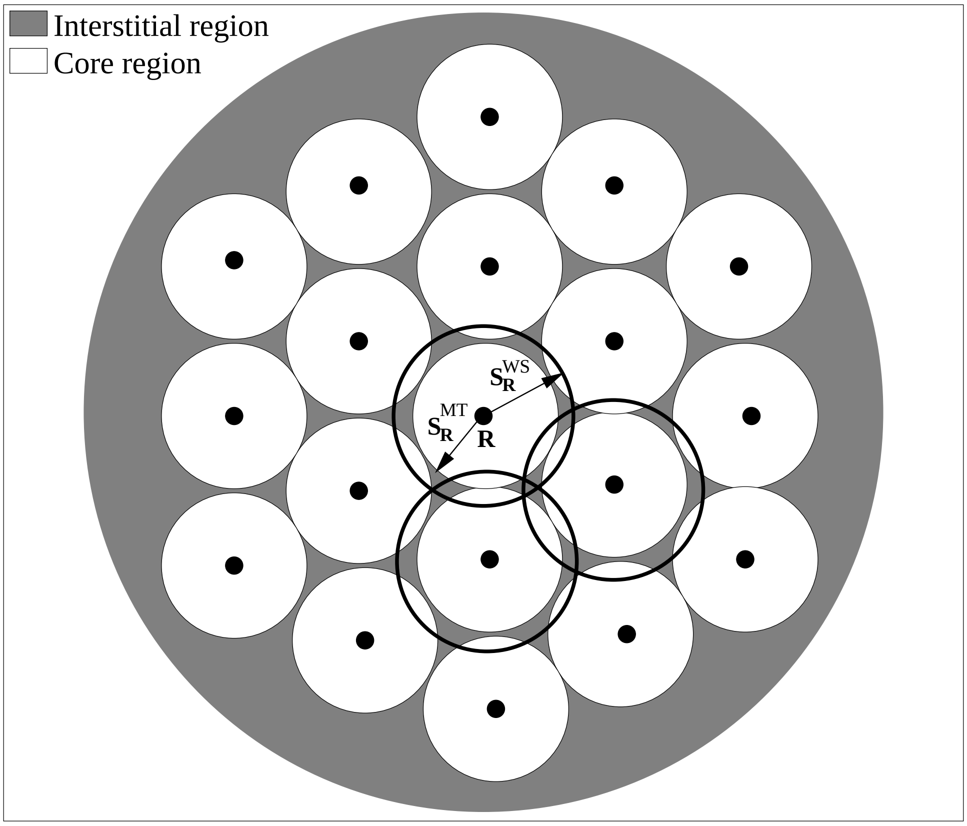

Figure 5.1: Schematic representation of the muffin-tin spheres. The Potential outside the muffin-tin spheres (radii $S_{\underline{R}}^{MT}$) is taken to be constant (zero) whereas inside is calculated assuming that it is spherically symmetric. The ASA approximation employs overlapping spheres with radii $S_{\underline{R}}^{WS} > S_{\underline{R}}^{MT}$.

The solutions of the Schrödinger equation, employing the ASA approximation inside the atomic sphere $\underline{R}$ ($\underline{r} < S_{\underline{R}}^{WS}$) are given by the partial waves, $\phi_{\underline{R}L}(r_{\underline{R}}, \varepsilon) \equiv \phi_{\underline{R}\ell}(r, \varepsilon) Y_L(\hat{\underline{r}}_{\underline{R}})$, where the functions $Y_L(\hat{\underline{r}}_{\underline{R}})$ are spherical harmonics. $\phi_{\underline{R}\ell}(r, \varepsilon)$ is a radial amplitude, $\hat{\underline{r}}_{\underline{R}} \equiv \underline{r}_{\underline{R}}/r_{\underline{R}}$, and $L = (\ell, m)$ denotes the angular-momentum character of the orbital. The energy ε is here a parameter and not an eigenvalue. The matching conditions at the spherical surface $S_{\underline{R}}^{WS}$ determine the eigenvalues of the solid.

The ASA fixes the electronic kinetic energy at zero in the (volumeless) interstitial region[4]. Hence, the problem in the interstitial reduces to solve the Laplacian equation, $\nabla^2 \Psi(\underline{r}) = 0$. This leads to the regular Bessel function, $J_L(r_{\underline{R}}) \equiv J_\ell(r) Y_L(\hat{\underline{r}}_{\underline{R}})$,

---

[4] As pointed out by [Turek 97], the employment of the interstitial region under the ASA approximation is inevitable for a proper mathematical formulation of the problem.

and the irregular Neumann functions, $K_L(r_{\underline{R}}) \equiv K_\ell(r)Y_L(\hat{r}_{\underline{R}})$[5]. The expansion theorem [Andersen 75, Andersen 84a, Skriver 84] relates the solutions of the Laplacian equation with respect to origins of different atomic spheres. Thus, the regular solutions inside the atomic sphere are matched to the irregular solution $K_L(r_{\underline{R}})$ centered at $\underline{R}$ which are expanded into regular solutions $J_{L'}(r_{\underline{R}'})$ centered at other $\underline{R}' \neq \underline{R}$, see equation (B.3).

Summarizing, the muffin-tin orbital basis, MTO, is defined in the whole space as a combination of the partial waves and the regular solutions, $\mathcal{N}^0_{\underline{R}L}(\varepsilon)\phi_{\underline{R}L}(r_{\underline{R}}, \varepsilon) + P_{\underline{R}L}(\varepsilon)J_{RL}(r_{\underline{R}})$, within the atomic sphere $\underline{R}$. The function $K^i_{\underline{R}L}(r_{\underline{R}})$, centered at $\underline{R}$, is taken for the interstitial region[6], and for the other spheres the solution is given by the expansion theorem, equation (B.3). Thus, the muffin-tin orbitals can be written as,

$$\begin{aligned} \chi_{\underline{R}L}(r_{\underline{R}}, \varepsilon) = {} & \mathcal{N}^0_{\underline{R}L}(\varepsilon)\phi_{\underline{R}L}(r_{\underline{R}}, \varepsilon) \\ & + \sum_{\underline{R}'L'} J_{\underline{R}'L'}(r_{\underline{R}'}) \left\{ \mathcal{P}^0_{\underline{R}'L'}(\varepsilon)\delta_{\underline{R}'L',\underline{R}L} - \mathcal{S}^0_{\underline{R}'L',\underline{R}L} \right\} \\ & + K^i_{\underline{R}L}(r_{\underline{R}}) \quad . \end{aligned} \tag{5.6}$$

Hence, the solution of the Schrödinger equation (5.2), in the MTO basis, can be written as $\Psi(\underline{r}, \varepsilon) = \sum_{\underline{R}L} \chi_{\underline{R}L}(r_{\underline{R}}, \varepsilon)\breve{a}_{\underline{R}L}$. After replacing the MTO basis (5.6), one can see that this solution satisfy the Schrödinger equation, inside $\underline{R}'$, only when the coefficients of $J_{\underline{R}'L'}(r_{\underline{R}'})$ vanish. This is known as the *tail-cancellation condition* and gives the KKR-ASA secular equation [Andersen 87],

$$\sum_{\underline{R}L} \breve{a}_{\underline{R}L} \left\{ \mathcal{P}^0_{\underline{R}L}(\varepsilon)\delta_{\underline{R}'L',\underline{R}L} - \mathcal{S}^0_{\underline{R}'L',\underline{R}L} \right\} = 0 \quad . \tag{5.7}$$

This is the equation that one must solve instead of (5.2). The structure constant, $\mathcal{S}^0$, and the potential function $\mathcal{P}^0$, are defined by equations (B.4) and (B.6), respectively. The structure constants are the expansion coefficients of the irregular solutions into the regular ones. The potential function is a result of the matching conditions at the atomic surfaces. The $\breve{a}_{\underline{R}L}$ are the expansion coefficients of the wave function in the muffin-tin orbital basis.

The secular equation (5.7) has nontrivial solutions only when the determinant of the matrix into brackets in (5.7) is zero. This gives the eigenvalues ε_i of the solid. As can be seen, the equation (5.7) separates the whole problem into structure constants, and a potential part, that depends only of the energy ε.

Exactly the energy dependence of $\mathcal{P}$ makes the problem (5.7) a non-linear one[7].

---

[5] According to the asymptotic behavior for $r \to 0$, the functions $J_L(r_{\underline{R}})$, and $K_L(r_{\underline{R}})$ are considered as regular and irregular solutions, respectively.

[6] Within the ASA, the functions $K^i_{\underline{R}L}(r_{\underline{R}})$ are not considered because the interstitial region has volume zero.

[7] The structure constants, $\mathcal{S}^0_{\underline{R}'L',\underline{R}L}$, are independent of the energy in the ASA as consequence of taking a zero kinetic energy in the interstitial region.

However, an equation linear in energy, such as the eigenvalue equation, is more familiar and computationally more efficient. The linearization of the secular equation (5.7) follows from an energy linearization (Taylor expansion) of the MTO basis (5.6) around some reference energy $\varepsilon_{\underline{R}\ell,\nu}$ which is usually chosen in the center of the occupied part of the valence state density of the orbital $\underline{R}L$. Thus, the new linearized MTO basis, LMTO basis, can be written as follows (in bracket-notation),

$$|\chi_{\underline{R}L}\rangle = |\phi_{\underline{R}L}\rangle + \sum_{\underline{R}'L'} \left\{ |\dot{\phi}_{\underline{R}'L'}\rangle + |\phi_{\underline{R}'L'}\rangle \; o_{\underline{R}'L'} \right\} \; h^{0}_{\underline{R}'L',\underline{R}L} \quad , \tag{5.8}$$

where $\underline{h}^0 = \underline{\mathcal{H}}^0 - \underline{\varepsilon}_\nu$ (see equation (5.9)). The elements $\varepsilon_{\underline{R}\ell,\nu}$ of the diagonal matrix $\underline{\varepsilon}_\nu$ are the reference energies used in the basis linearization. The dot in $|\dot{\phi}_{\underline{R}L}\rangle$ means the energy derivative of the partial wave, evaluated in $\varepsilon = \varepsilon_{\underline{R}\ell,\nu}$. The matrix $\underline{o}$ has diagonal elements $o_{\underline{R}L}\delta_{\underline{R}'L',\underline{R}L} = \langle \phi_{\underline{R}'L'} | \overline{\dot{\phi}}_{\underline{R}L}\rangle$, where $|\overline{\dot{\phi}}_{\underline{R}L}\rangle$ is the part inside the brackets in equation (5.8).

As expected, the secular equation (5.7) in the LMTO basis reduces to an linear equation (eigenvalue problem), $(\underline{\mathcal{H}}^0 - \varepsilon\underline{\mathcal{O}}^0)\underline{a} = 0$, where the Hamiltonian matrix is written as [Andersen 87],

$$\underline{\mathcal{H}}^0 = \underline{C} + \sqrt{\underline{\Delta}}\,\underline{\mathcal{S}}^0\,\sqrt{\underline{\Delta}} \quad , \tag{5.9}$$

and $\underline{C}$ and $\underline{\Delta}$, are diagonal matrices whose matrix elements are the so-called *potential parameters* that justly linearize the potential function $\mathcal{P}^0(\varepsilon)$ in the following way (indices $\underline{R}\ell$ omitted)

$$\mathcal{P}^0(\varepsilon)^{-1} \simeq \frac{\Delta}{\varepsilon - C} + \gamma \quad . \tag{5.10}$$

The potential parameters are defined in equation (B.8). Physically, C, Δ, and γ give the position of the band centre, the width of the band, and the distortion of the band, respectively.

Transformation of the orbital basis

It is possible to obtain different LMTO basis sets with certain properties, such as orthogonality or tight-binding behavior. This follows on writing equation (5.7) as $\underline{\mathcal{P}}[\underline{\mathcal{S}}^{-1} + \underline{\alpha} - \underline{\alpha} - \underline{\mathcal{P}}^{-1}]\underline{\mathcal{S}}\underline{a} = 0$ with a new matrix $\underline{\alpha}$ which is diagonal with elements $\alpha_{\underline{R}\ell}$ that are freely chosen. Then, from the transformations

$$(\underline{\mathcal{S}}^0)^{-1} - \underline{\alpha} \equiv (\underline{\mathcal{S}}^\alpha)^{-1} \quad \texttt{and} \quad (\underline{\mathcal{P}}^0)^{-1} - \underline{\alpha} \equiv (\underline{\mathcal{P}}^\alpha)^{-1} \quad , \tag{5.11}$$

follows the new representation $[\underline{\mathcal{P}}^\alpha - \underline{\mathcal{S}}^\alpha]\underline{a}^\alpha = 0$ with the same eigenvalues as equation (5.7).

The LMTO basis and the multiple scattered-wave method have many common properties[8], such as the muffin-tin potential, the atomic basis functions, the expansion in

---

[8] A numerical comparative study can be found, for instance, in [Arnold 97].

local angular-momentum basis functions, the structure constants, the secular equation (5.7), and the resonant potential function. For instance, the potential function is related with the phase shift as follows, $\mathcal{P}_{\underline{R}L} = \mathcal{P}_{\underline{R}\ell}(\varepsilon) = -\cot\eta_{\underline{R}\ell}(\varepsilon)$. Thus, from equation (5.11), one can relate $\underline{\alpha}$ to a *background* phase shift which provides the expected properties.

In the following we describe different LMTO basis-sets with their respective properties. The election of $\underline{\alpha} = 0$ provides the original LMTO basis, also called the *canonical* LMTO basis, described above.

The election of $\underline{\alpha} = \underline{\gamma}$ gives $\mathcal{P}^\gamma = (\varepsilon - C)/\Delta$ which provides an orthogonal LMTO basis. Thus the eigenvalue equation is reduced to $(\underline{\mathcal{H}}^\gamma - \varepsilon\underline{\mathcal{I}})\underline{a} = 0$ with the Hamiltonian

$$\underline{\mathcal{H}}^\gamma = \underline{h}^\gamma + \underline{\varepsilon}_\nu = \underline{C}^\gamma + \sqrt{\underline{\Delta}^\gamma}\;\underline{\mathcal{S}}^\gamma\;\sqrt{\underline{\Delta}^\gamma} \quad . \tag{5.12}$$

This is the LMTO basis employed in the present work together with the supercell concept (described below).

The *tight-binding* LMTO basis, TB-LMTO, is obtained from the transformation equations (5.11) with the condition that the basis must be most-localized. The structure constants in the canonical LMTO basis, $\underline{\mathcal{S}}^0$, are long-range, i.e. they decrease slowly with the increasing distance $|\underline{R} - \underline{R}'|$. However, for numerical calculations one wants to have structure constants with rapid convergence on increasing $|\underline{R} - \underline{R}'|$. It was shown [Andersen 84b, Andersen 85, Andersen 87], for different crystalline lattices, that a particular choice of *screening* constants $\alpha_{\underline{R}\ell} = \beta_\ell$, where β_ℓ is independent of $\underline{R}$, leads to the tight-binding structure constants $\underline{\mathcal{S}}^\beta$.

Table 5.1: Screening constants $\alpha_{\underline{R}\ell} = \beta_\ell$ employed for the transformation of the conventional (canonical) LMTO basis to the tight-binding (screened) LMTO basis, see equation (5.11). The values have been taken from [Andersen 87, Turek 97].

ℓ_{max}	β_s	β_p	β_d	β_f
0	0.2143			
1	0.2872	0.02582		
2	0.3485	0.05303	0.01071	
3	0.3851	0.07321	0.02248	0.00607

As expected, the $\mathcal{S}^\beta_{\underline{R}L,\underline{R}'L'}$, also called screened structure constants, decrease rapidly after increasing the distance $|\underline{R} - \underline{R}'|$. This provides us the possibility to calculate only those elements $\mathcal{S}^\beta_{\underline{R}L,\underline{R}'L'}$ for which $|\underline{R} - \underline{R}'|$ is shorter than the distance to the second nearest neighbors, see appendix B.2 for details. Moreover, it is important to note that the β_ℓ values, optimized for simple crystalline structures, have been employed even for complex close-packed models, such as amorphous and approximants of quasicrystals, for instance see [Nowak 91] and [Windisch 94, Krajčí 99], respectively. The optimal β_ℓ-values depend only on the maximum orbital ℓ used in the basis, ℓ_{max}. These values are listed in table (5.1).

Thus, the hamiltonian matrix in the tight-binding LMTO representation is given by,

$$\underline{\mathcal{H}}^{\beta} = \underline{h}^{\beta} + \underline{\varepsilon}_{\nu} = \underline{C}^{\beta} + \sqrt{\underline{\Delta}^{\beta}}\;\underline{\mathcal{S}}^{\beta}\;\sqrt{\underline{\Delta}^{\beta}} \quad . \tag{5.13}$$

The TB-LMTO basis has been employed in supercell [Krajčí 99] and real space (recursion) [Hafner 93] methods to account for the electronic properties of approximants of quasicrystals. The $\underline{k}$-summation in the supercell methods provides the spectral fine structure of the state density that comes from long-range effects.

Supercell concept

The supercell concept gives us the possibility to study a material considering only the atomic order in a large unit-cell. Surface effects are avoided applying the periodicity of the supercell. This concept can be employed in models of amorphous and liquid phases where the structure models are also generated with periodic boundary conditions. Supercells have direct applications in realistic low order approximants of quasicrystals because they are crystals with more than 100 atoms in large unit-cells.

Thus, the lattice points $\underline{R}$ can be expressed in the form $\underline{R} = \underline{B} + \underline{t}$ where the vectors $\underline{B}$ denote the basis vectors while the vectors $\underline{t}$ are the translation vectors. Hence, the LMTO basis, can be transformed into a $\underline{k}$-dependent basis, $|\chi^{\alpha}_{\underline{B}L}(\underline{k})\rangle$ (the super-index α indicates the orbital basis), by

$$|\chi^{\alpha}_{\underline{B}L}(\underline{k})\rangle = \sum_{\underline{t}} |\chi^{\alpha}_{(\underline{B}+\underline{t})L}\rangle \; e^{i\underline{k}\underline{t}} \quad , \tag{5.14}$$

where $\underline{k}$ denotes a vector from the first Brillouin zone (1.BZ). Then, the eigenvalue problem is transformed[9] to $\{\, \underline{\mathcal{H}}^{\alpha}(\underline{k}) - \varepsilon^{\underline{k},(i)}\, \underline{\mathcal{I}} \,\}\; \underline{a}^{\underline{k},(i)} = 0$ with

$$\underline{\mathcal{H}}^{\alpha}(\underline{k}) = \underline{C}^{\alpha} + \sqrt{\underline{\Delta}^{\alpha}}\;\underline{\mathcal{S}}^{\alpha}(\underline{k})\;\sqrt{\underline{\Delta}^{\alpha}} \quad , \tag{5.15}$$

where,

$$S^{\alpha}_{\underline{B}'L',\underline{B}L}(\underline{k}) = \sum_{\underline{t}} S^{\alpha}_{\underline{B}'L',(\underline{B}+\underline{t})L} \; e^{i\underline{k}\underline{t}} \quad . \tag{5.16}$$

The electronic wave function of the eigenstate $\varepsilon^{\underline{k},(i)}$ can be expanded in the LMTO basis as,

$$|\Psi^{\underline{k},(i)}\rangle = \sum_{\underline{B}L} |\chi^{\alpha}_{\underline{B}L}(\underline{k})\rangle \; a^{\underline{k},(i)}_{\underline{B}L} \quad , \tag{5.17}$$

where $a^{\underline{k},(i)}_{\underline{B}L}$ are the eigenvectors of the Hamiltonian (5.15) corresponding to the eigenvalue $\varepsilon^{\underline{k},(i)}$.

---

[9] Of course, this procedure reduces the size of the matrices in the eigenvalue problem. One works only with atoms, $\underline{B}$, in the supercell instead of atoms, $\underline{R}$, in the whole crystals. For example, for hundred atoms in the supercell and nine orbitals (spd) per atom, the size of the Hamiltonian matrix (5.15) is 900×900.

The local density of states of the atomic sphere $\underline{B}$ can be calculated from $\widehat{n}_{\underline{B}}(\varepsilon) = \int_{(\underline{B})} d^3\underline{r}\, n(\underline{r},\varepsilon) = \sum_{\ell} n_{\underline{B}l}(\varepsilon)$, where,

$$n(\underline{r},\varepsilon) = 2\sum_{\underline{k},(i)} |\Psi^{\underline{k},(i)}(\underline{r})|^2 \delta(\varepsilon - \varepsilon^{\underline{k},(i)}) = -\frac{2}{\pi}\,\mathrm{Im}\, G^{+}(\underline{r},\underline{r};\varepsilon + i0) \quad . \tag{5.18}$$

This equation relates the Green function with the state density. The delta functions in (5.18) are replaced by gaussians, equation (3.6), which gives a smooth density of states. Moreover, deviations from the perfect structure are accounted for by this Gaussian broadening. The total density of states can be obtained as the sum over all local state densities, $\widehat{n}(\varepsilon) = (1/N_c)\sum_{\underline{B}}^{N_c} \widehat{n}_{\underline{B}}(\varepsilon)$ (here, N_c is the number of atoms in the supercell).

The spectral conductivity can be calculated employing the Kubo-Greenwood formula[10], equation (3.5), which is evaluated with the LMTO wave functions. In this formula, the matrix elements $\langle \Psi^{\underline{k},(i)} | v_{\mu} | \Psi^{\underline{k},(j)} \rangle$ are calculated following Hobbs *et al.* [Hobbs 95] and Arnold [Arnold 97]. This is not a straightforward task and will be briefly explained in appendix B.1.

Finally, it is worth noting that the summation of the $\underline{k}$ vectors in the 1.BZ can be performed in different ways. The tetrahedron [Jepsen 71] method and the special-point scheme [Baldereschi 73, Chadi 73] are the most common procedures used. The last one will be employed here and a description of it is presented in appendix B.1.

TB-LMTO cluster recursion method

The properties of the TB-LMTO basis were described above, in the following we present this basis in relation with the recursion procedure for $\underline{r}$-space calculations. Two reasons guide us to use the TB-LMTO basis together with the recursion procedure instead of the supercell method. Firstly, the existence of spikes which can influence the transport properties of quasicrystals, as discussed in chapter 4, can be tested employing $\underline{r}$-space cluster recursion methods. Thus, after comparing the LMTO-ASA supercell results with the TB-LMTO cluster recursion method, spurious spectral structure, that can arise from the $\underline{k}$-summation, should be identified. Secondly, recursion methods permit to work with structure models containing up to 1000-1500 atoms per cluster. This is not possible with the supercell concept.

However, approximants and quasicrystals have wide electronic valence bands, ∼12 eV, due to their high content of aluminium. Thus, a transformation to a basis that provides a Hamiltonian with more accuracy in $(\varepsilon - \varepsilon_{\underline{R}\ell,\nu})$ is required. Hence, for the recursion method the TB-LMTO basis must be transformed to the orthogonal LMTO basis ($\underline{\alpha} = \underline{\gamma}$), because, the Hamiltonian of the first one is accurate to first order in $(\varepsilon - \varepsilon_{\underline{R}\ell,\nu})$ whereas the Hamiltonian of the second one is accurate to second

---

[10] An additional summation over $\underline{k}$ vectors must be performed in (3.5) because of $\Psi^{\underline{k},(i)}$ and $\varepsilon^{\underline{k},(i)}$ depend on $\underline{k}$.

order in $(\varepsilon - \varepsilon_{\underline{R}\ell,\nu})$. Therefore, through the expansion [Andersen 87, Bose 88],

$$\underline{h}^{\gamma} = \underline{h}^{\beta}(1 + o^{\beta}\underline{h}^{\beta})^{-1} = \underline{h}^{\beta} - \underline{h}^{\beta}o^{\beta}\underline{h}^{\beta} + \underline{h}^{\beta}\underline{o}^{\beta}\underline{h}^{\beta}\underline{o}^{\beta}\underline{h}^{\beta} - \cdots \quad , \tag{5.19}$$

the nearly orthogonal Hamilton matrix, equation (5.12), is obtained. Note that the expansion (5.19) is more efficient to build directly the orthogonal Hamiltonian (5.12) because the structure constants in the TB-LMTO basis are the most localized and converge more rapidly (as explained above).

Similarly, a transformation of the potential parameters is given by [Andersen 87, Bose 88] (indices $\underline{R}\ell$ omited),

$$\frac{C^{\beta} - \varepsilon_{\nu}}{C^{\gamma} - \varepsilon_{\nu}} = \left(\frac{\Delta^{\beta}}{\Delta^{\gamma}}\right)^{1/2} = \frac{\beta - \gamma}{o^{\beta}\Delta^{\gamma}} = 1 + \frac{\beta - \gamma}{\Delta^{\gamma}}(c^{\gamma} - \varepsilon_{\nu}) \quad . \tag{5.20}$$

In this work, the TB-LMTO Hamiltonian will be transformed into the orthogonal LMTO Hamiltonian employing the expansion (5.19) up to the term $\underline{h}^{\beta}\underline{o}^{\beta}\underline{h}^{\beta}\underline{o}^{\beta}\underline{h}^{\beta}$ where convergence is reached. Then, this hamiltonian will be employed together with the recursion procedure to obtain the electronic properties (see below).

Recursion procedure

In the framework of electronic structure calculations, the goal of the recursion method [Haydock 80] is that it avoids the solution of the eigenvalue problem providing directly *projected state densities*,

$$\widehat{n}_{\varphi}(\varepsilon) = \lim_{\zeta \to 0}\left\{ -\frac{1}{\pi}\ \mathrm{Im}\ G_{\varphi,\varphi}(\varepsilon + i\zeta)\right\} \quad , \tag{5.21}$$

which are obtained from a diagonal element of the one-particle Green function $G(\varepsilon + i\zeta) = (\varepsilon + i\zeta - \mathcal{H})^{-1}$, with $\mathcal{H}$ a given Hamiltonian and ζ a positive infinitesimal. In equation (5.21), $\widehat{n}_{\varphi}(\varepsilon)$ reads density of states projected onto the state $|\varphi\rangle$, for example, if this state is a local atomic orbital ℓ at the site $\underline{R}$ then, the projected density of states is just the component ℓ of the local state density, $\widehat{n}_{\underline{R}\ell}(\varepsilon)$ (c.f. equation (5.18)). As was discussed in chapter 4, densities of states are important quantities because their spectral features can determine the transport.

The recursion procedure is a real-space technique to tridiagonalize a symmetric (Hermitian) matrix. This technique is related to the symmetric Lanczos method [Lanczos 50]. In our case, the symmetric matrix is the orthogonal LMTO Hamiltonian, $\underline{\mathcal{H}}^{\gamma} = \underline{h}^{\gamma} - \underline{\epsilon}_{\nu}$, which is obtained from the TB-LMTO one, equation (5.19).

The basic idea of the recursion method is simple: it defines a basis $\{|n\rangle\}$, called the Lanczos basis, in which the symmetric (Hermitian) Hamilton matrix adopts a tridiagonal form, $\underline{\mathcal{T}}$. Then, the corresponding one-particle Green function, $G(\varepsilon + i\zeta) =$

$(\varepsilon + i\zeta - \underline{\mathcal{T}})^{-1}$, can be expressed as a continued fraction,

$$G(z) = \cfrac{1}{z - a_1 - \cfrac{b_1^2}{z - a_2 - \cfrac{b_2^2}{\cfrac{\vdots}{z - a_n - \cfrac{b_n^2}{\cfrac{\vdots}{z - a_{n_{max}} - b_{n_{max}}^2\, t(z)}}}}}} \quad , \tag{5.22}$$

where $z = \varepsilon + i\zeta$, and $\{a_n, b_n\}$ are the diagonal, respectively, non-diagonal elements of the tridiagonal matrix $\underline{\mathcal{T}}$, see equation (B.39). n_{max} is chosen such that $n_{max} \ll N$, where N is the dimension of $\underline{\mathcal{H}}$. After inserting this continued fraction, equation (5.22), into (5.21) one obtains a simple form for the state density.

The recursion coefficients $\{a_n\}$ and $\{b_n\}$ depend on the state $|\varphi\rangle$. In fact, choosing an initial state $|1\rangle \equiv |\varphi\rangle$, the recursion procedure gives (see appendix B.2),

$$\begin{aligned} a_1 &= \langle 1|\mathcal{H}|1\rangle \\ b_1^2 &= \langle 1|(\mathcal{H} - a_1\mathcal{I})^\dagger(\mathcal{H} - a_1\mathcal{I})|1\rangle \\ |2\rangle &= \frac{1}{b_1}\Big\{(\mathcal{H} - a_1\mathcal{I})|1\rangle\Big\} \quad , \end{aligned} \tag{5.23}$$

together with $(n \geq 2)$

$$\begin{aligned} a_n &= \langle n|\mathcal{H}|n\rangle \\ b_n^2 &= \Big\{\langle n|(\mathcal{H} - a_n\mathcal{I})^\dagger - \langle n-1|b_{n-1}\Big\}\Big\{(\mathcal{H} - a_n\mathcal{I})|n\rangle - b_{n-1}|n-1\rangle\Big\} \\ |n+1\rangle &= \frac{1}{b_n}\Big\{(\mathcal{H} - a_n\mathcal{I})|n\rangle - b_{n-1}|n-1\rangle\Big\} \quad . \end{aligned} \tag{5.24}$$

As a result of this procedure, the new $\{|n\rangle\}$ form an orthogonal basis which is related to the original basis (in our case, orthogonal LMTO basis) by

$$|n\rangle = \sum_{\underline{R}L} u^n_{\underline{R}L} |\chi^\gamma_{\underline{R}L}\rangle \quad , \tag{5.25}$$

where the coefficients $u^n_{\underline{R}L}$ are the weights of each $|\chi^\gamma_{\underline{R}L}\rangle$. For example, if we want to calculate the component ℓ_1 of the local state density at $\underline{R}_1$, then our initial state $|1\rangle = |\varphi\rangle$ is obtained from (5.25) choosing $u^1_{\underline{R}_1\ell_1} = 1$, and $u^1_{\underline{R}L} = 0$ for all $\underline{R}L \neq \underline{R}_1 L_1$.

The local physics of the system is completely determined by $\{|n\rangle\}$ and the coefficients $\{a_n\}$ and $\{b_n\}$ which are fixed after choosing $|\varphi\rangle$ (the initial state $|1\rangle$). An one dimensional system has, in the tight-binding approximation (5.1), a three-diagonal Hamiltonian which is similar to $\underline{\mathcal{T}}$, (B.39). Therefore, the transformation (5.25) can

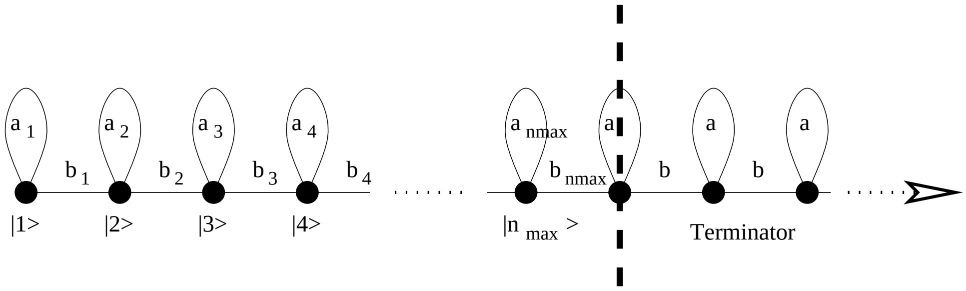

Figure 5.2: Schematic representation of the recursion procedure in an one-dimensional chain model. Choosing the first node $|1\rangle = |\varphi\rangle$ the coefficients a_n and b_n, and the states $|n\rangle$ can be determined, as shown in text. After some level n_{max} a terminator is employed. Drawing based on [Haydock 80].

also be seen [Haydock 80] as the mapping of the three-dimensional system onto a one-dimensional chain model, see figure (5.2).

Finally, $t(z)$ in (5.22) is a terminator function applied at the level n_{max}, see figure (5.2). $t(z)$ emulates the effect of the infinite tail of the continued fraction and makes the spectrum a continuous one. If after some level n_{max} one takes constant recursion coefficients: $a_i = a_{n_{max}} = a$ and $b_i = b_{n_{max}} = b$, the remainder infinite continued fraction can be performed analytically. Thus, the terminator can be written as

$$t(z) = -\frac{(z-a)}{2} \pm \frac{\sqrt{(z-a)^2 + 4b^2}}{2} \quad . \tag{5.26}$$

This terminator is called the *square-root* terminator. The Green function of a surface atom in an one-dimensional periodic system has just the form of $t(z)$, (5.26), where a is the site energy and b the hopping term. That means, its state density is given by, $\widehat{n}(\varepsilon) = \lim_{\zeta \to 0} \big[-(1/\pi) \text{ Im } t(\varepsilon + i\zeta) \big]$.

Normally, the coefficients a_n and b_n do not converge to determined values which can be employed for the terminator function. In this case, other more sophisticated ways to get the asymptotic values, a and b, from the know ones is required. The Beer and Pettifor [Beer 84], and Luchini and Nex [Luchini 87] terminators are the most common procedures.

Electronic diffusivity within the recursion method

Transport properties can also be determined employing the recursion procedure. If we have the electronic diffusivity then, the spectral conductivity can be calculated employing the Einstein relation (3.8). In fact, after rewriting the Kubo-Greenwood formula of the spectral conductivity (3.5), Bose showed that the electronic diffusivity, at the Fermi energy, can be calculated by [Bose 93],

$$D_{\mu,\mu}(\varepsilon_F) = \lim_{\zeta \to 0} \left\{ -\hbar \text{ Im } \Big[\langle \varepsilon_m | v_\mu \, G(\varepsilon_F + i\zeta) \, v_\mu | \varepsilon_m \rangle \Big]_{\varepsilon_m = \varepsilon_F} \right\} \quad , \tag{5.27}$$

where $\left[\quad\right]_{\varepsilon_m=\varepsilon_F}$ means an average over the eigenfunctions with energies $\varepsilon_m = \varepsilon_F$. Thus, the electronic diffusivity can be seen as the average of state densities projected onto states $v_\mu|\varepsilon_m\rangle$. That means, taking $|1\rangle \equiv |\varphi\rangle = v_\mu|\varepsilon_m\rangle/q$ as our initial state with $q^2 = \langle\varepsilon_m|v_\mu v_\mu|\varepsilon_m\rangle$, the recursion procedure, described above, can be employed[11].

Two problems arise with the determination of the initial state. Namely, the calculation of the velocity matrix v_μ and the eigenfunction $|\varepsilon_m\rangle$. The first one can be determined from $v_\mu = (i/\hbar)\ [\mathcal{H}, \mu]$, as explained in appendix B.2. The eigenfunction with energy $\varepsilon = \varepsilon_m$ can be obtained employing a modified recursion procedure, called *filter technique*, proposed by Stein and Krey [Stein 80], see appendix B.2.

At least, it is worth noting that numerical calculations of projected state densities, equations (5.21) or (5.27), are realized employing a fixed ζ which is very small but non-zero. The meaning of this is similar to the width of the Lorentz functions (3.7) employed in the Kubo-Greenwood formula (3.5).

Landauer-Büttiker Conductance

In the following, we present the way to calculate the conductance of a quasi-one dimensional system employing the Landauer/Büttiker approach [Büttiker 85]. A detailed description of the procedure can be found in [Kahnt 94, Kahnt 95, Löser 96]. In the following we present only a brief description of this method.

The electron scattering at a two-dimensionally periodic layer can be treated in a plane wave basis. The plane waves

$$\begin{aligned} \phi^{\alpha}_{\tau}(\varepsilon, k_{||}, r) &= \frac{1}{\sqrt{k_\tau}} e^{i\,\underline{k}^{\alpha}_{\tau}\cdot\underline{r}} \quad , \\ \underline{k}^{\alpha}_{\tau} &= \underline{k}_{||} + \underline{\tau} + \underline{\hat{e_z}}\ \alpha\ \kappa_\tau \quad , \\ \kappa_\tau &= \sqrt{\kappa^2 - (\underline{k}_{||} + \underline{\tau})^2} \quad , \end{aligned} \tag{5.28}$$

are characterized by the energy $\varepsilon = \kappa^2$ and by the parallel component of the wave vector $\underline{k}_{||}$ which is confined to the first Brillouin zone of the two-dimensional reciprocal lattice (lattice vectors $\underline{\tau}$). There exist two kinds of waves: propagating and evanescent waves for $\kappa^2 \geq (\underline{k}_{||} + \underline{\tau})^2$ and $\kappa^2 < (\underline{k}_{||} + \underline{\tau})^2$, respectively. The number of propagating waves is finite and the number of evanescent waves infinite. Such a layer transmits and reflects an incoming wave with wave-vector $\underline{k}_{||}$ into sets of outgoing waves on both sides of the layer (see the schematic process in figure (5.3)).

The planar scattering problem is solved in the framework of the muffin-tin scattered wave method where the energy dependent phase shifts are calculated self-consistently for the effective atoms of the LMTO-ASA supercell approach, see for instance [Arnold 97]. Thus, the transmission matrix, $t(d)$, of a bar (thickness d) can be obtained from $\underline{\mathcal{S}}^{sc} = i\kappa\underline{\mathcal{B}}[\underline{\mathcal{F}}^{-1} - \underline{\mathcal{G}}]^{-1}\underline{\mathcal{A}}$, the scattering matrix in the plane wave

---

[11] The use of the factor q in $|1\rangle \equiv |\varphi\rangle = v_\mu|\varepsilon_m\rangle/q$ is necessary because the recursion equations require $\langle 1|1\rangle = 1$. Hence, the obtained diffusivity must be finally multiplied by q^2.

representation[12].

Hence, the conductance of a bar (really slab, see below), is calculated through,

$$G(d) = \frac{2e^2}{h} Tr \left\{ t^{\dagger}(d)\, t(d) \right\} \quad . \tag{5.29}$$

The linear average of

$$R(d) = G^{-1}(d) = R_o + \left(\frac{d}{A} \right) \rho + \text{fluctuations} \quad , \tag{5.30}$$

provides the resistivity of the system [Kahnt 95].

This implementation is close to the low energy electron diffraction (LEED) approach, i.e. we have ideal-leads boundary conditions along the transport direction and periodic transverse boundary conditions. This transforms the bar into a slab (thickness d) in free space.

Finally, it is worth noting that the Landauer/Büttiker concept, in similar form as the previously presented methods, works for systems containing transition metals [Kahnt 95]. Of course, this is of interest for the study of realistic icosahedral quasicrystals containing transition metals.

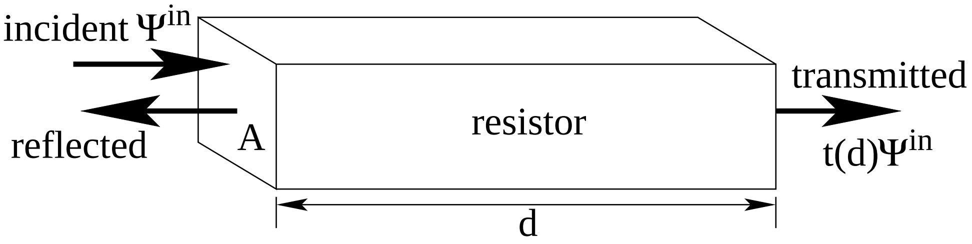

Figure 5.3: Schematic description of the Landauer/Büttiker model of conductance. Cross section A, and length d. The information necessary to obtain the conductance of the material is contained in the transmission matrix $t(d)$, see text for details.

---

[12] The matrix $i\kappa[\underline{\mathcal{F}}^{-1} - \underline{\mathcal{G}}]^{-1}$ is a result of the multiple scattering theory, where $\underline{\mathcal{F}}$ is the scattering-amplitude matrix and $\underline{\mathcal{G}}$ the structure constants. The matrices $\underline{\mathcal{A}}$ and $\underline{\mathcal{B}}$ provide the transformations of the amplitude vectors in the plane wave and angular-momentum representations: for the incident wave $|\Psi^{inc}\rangle = \mathcal{A}|\Psi^{inc}_{pw}\rangle$, and for the scattered wave $|\Psi^{sc}_{pw}\rangle = \mathcal{B}|\Psi^{sc}\rangle$ [Kahnt 94, Löser 96].

Chapter 6

The Al-Cu-Fe system

In the present chapter, we will show calculations of the electronic properties of Al-Cu-Fe approximants/quasicrystals taking into account the structural and chemical order. For this end, spectral properties are calculated employing *ab-initio* methods, see chapter 5. As was discussed in chapter 4.3, it is expected that the local chemical order (∼10-20Å) provides spectral features in approximant phases which can be rescaled to account for the related quasicrystal to explain its *anomalous* transport properties, see chapters 3 and 4.

The chapter is organized as follows. First, we will describe the structures of the investigated phases. In the next two sections, both the spectral and temperature dependent properties of the 1/1 approximant will be presented and compared with crystalline and amorphous phases. Thus, one can search for peculiar spectral features of the approximant phase. The icosahedral Al-Cu-Fe bulk quasicrystal is studied in the last section.

Structure models

Cockayne *et al.* [Cockayne 93] proposed a structure model for the 1/1 approximant of the icosahedral Al-Cu-Fe phase, hereafter called *the Cockayne model*, which has the following properties:

- A cubical cell with lattice constant $a = 12.3$Å and space group $P2_13$, see table (6.1).
- There are 128 atoms in the unit cell (80 Al, 32 Cu, and 16 Fe).
- One can discriminate 14 non-equivalent sites, see table (6.1).
- The basic cluster of this structure is the Bergman icosahedron (33 atoms) formed by a Cu atom in the center, an inner icosahedral shell (3 Fe and 9 Al) and an outer shell of 20 atoms (13 Cu and 7 Al).
- Each unit cell contains four overlapping Bergman icosahedra in a face-centered arrangement together with 20 glue atoms (16 Al and 4 Fe), see figure (6.1).

- The Fe atoms form a Fibonacci planar order (*lsllsl*... sequence with $l/s = \tau^* = (\sqrt{5}+1)/2$) in three perpendicular directions, see figures (6.1) and (6.9). We will come back to this point below.

The Cockayne model is preferred because the unit cell is strictly defined. Other models [Quiquandon 97, Takeuchi 00] are not fully defined.

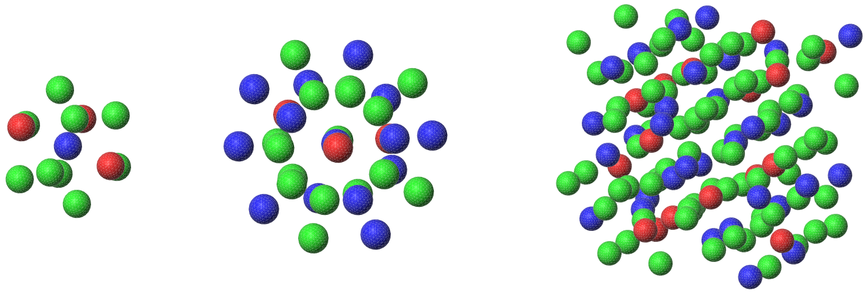

Figure 6.1: Cluster formation of the i-Al-Cu-Fe 1/1 approximant. From left to right, the inner icosahedron (1 Cu, 3 Fe, 9 Al), the Bergman cluster: 1 Cu atom in the center, an inner icosahedral shell and an outer shell of 20 atoms (13 Cu and 7 Al), and the 128 atoms in the unit cell: four overlapping Bergman clusters in a face-centered arrangement together with 20 glue atoms (16 Al, and 4 Fe). Note the planar arrangement of Fe atoms. Code: Fe (red), Cu (blue), Al (green).

The crystalline non-approximant phase employed here is the ω-Al_7Cu_2Fe with space group P4/mnc and lattice constants $a = b = 6.336$Å, and $c = 14.87$Å [Villars 91]. This non-approximant crystal has 40 atoms in the unit cell (28 Al, 8 Cu, and 4 Fe).

Table 6.1: Structure parameters of the 1/1 approximant of the i-Al-Cu-Fe [Cockayne 93]: Lattice constant $a = b = c = 12.3$Å, and Space Group $P2_13$. Atom types, symmetry sites, and coordinates (x,y,z) in (a,b,c)-units are presented.

Atom	Site	x/a	y/b	z/c	Atom	Site	x/a	y/b	z/c
Fe(1)	4a	0.843	0.843	0.843	Cu(1)	4a	0.336	0.336	0.336
Fe(2)	12b	0.540	0.348	0.672	Cu(2)	12b	0.036	0.836	0.150
Al(1)	4a	0.049	0.549	0.951	Al(6)	4a	0.543	0.043	0.457
Al(2)	12b	0.030	0.541	0.346	Cu(3)	12b	0.554	0.022	0.858
Al(3)	12b	0.226	0.857	0.475	Al(7)	12b	0.732	0.343	0.336
Al(4)	12b	0.247	0.850	0.833	Al(8)	12b	0.230	0.533	0.635
Al(5)	12b	0.732	0.029	0.159	Cu(4)	4a	0.348	0.848	0.652

On the other hand, modeling amorphous three-component systems is not a simple task, because, neither partial pair correlations nor the corresponding interaction potentials are known. Morse potentials have been applied to MacKay-type icosahedral Al-Mn phases [Tei-Ohkawa 93]. We employ the same potentials in a Monte-Carlo approach and obtain a model for amorphous AlFe.

It is worth noting that the last two structure models have similar compositions close to the 1/1 approximant, $Al_{62.5}Cu_{25}Fe_{12.5}$. The compositions for the non-approximant crystal, and the amorphous phase are $Al_{70}Cu_{20}Fe_{10}$, and $Al_{84}Fe_{16}$, respectively.

6.1 Spectral properties

Three energy scales

As was discussed in chapter 4, spectral structures of the order of ∼1 eV are proved important for the stability of the Hume-Rothery quasicrystalline (approximants), crystalline, and amorphous phases. The *anomalous* transport properties of quasicrystals (approximants) are attributed to very fine spectral features (*spikes* of the order of ∼10-20 meV), as consequences of the quasiperiodicity [Fujiwara 89, Fujiwara 93b]. However, the existence of spikes is under debate, see chapter 4.

In the following, the spectral features of the state density are discussed in three energy scales: i) the ∼1 eV scale, important for the stability, ii) the ∼10-20 meV scale, due to a combined effect of finite $\underline{k}$-space summation (artifact of the calculation) and the quasicrystalline structure (for the approximant), and iii) the ∼100 meV scale, which can explain *quantitatively* the *anomalous* transport of quasicrystals (approximants).

Calculations with high energy resolution are required to analyse spectral features of the order of ∼10-20 meV and higher. Figure (6.2) shows the total densities of states of the approximant (left), amorphous (middle), and non-approximant crystalline (right) phases. These calculations have been carried out employing the LMTO-ASA supercell method (see chapter 5) with an energy interval of ∼1 meV for the approximant, and ∼1.4 meV for the other phases. The DOS is smoothed with Gaussian broadening, half-width $\Sigma = 5$ meV, of the one-particle energies. Thus, all spectral features on a scale smaller than 10 meV are smeared out. Increasing the set of special points, $\{\underline{K}^{(n)}\}$, the number of the employed $\underline{k}$-points increases: following equation (B.22), 4, 20, 120 special $\underline{k}$-points are employed for $n =$2, 3, 4, respectively.

The results presented in figure (6.2) show that the state densities of the approximant as well as the amorphous and the non-approximant crystalline models are spiked. The spikes in the curves for both the metallic amorphous and the non-approximant crystal have no physical justification, because, neither *anomalous* properties nor elements of quasiperiodicity are given. Furthermore, one can see that after increasing the set of special points, the spiked structure is reduced. In similar form, for a given set of special points, the spiked structure reduces from the non-approximant crystal to the approximant. This is due to the number of atoms in the unit cell: the non-approximant crystal, the amorphous model, and the approximant contain 40, 100, and 128 atoms, respectively. These results are in agreement with the works of Zijlstra (three-dimensional Penrose tilings, [Zijlstra 01]) and Haerle and Kramer (toy models of simple cubic He crystals, [Haerle 98]), where it is shown that *unphysical*

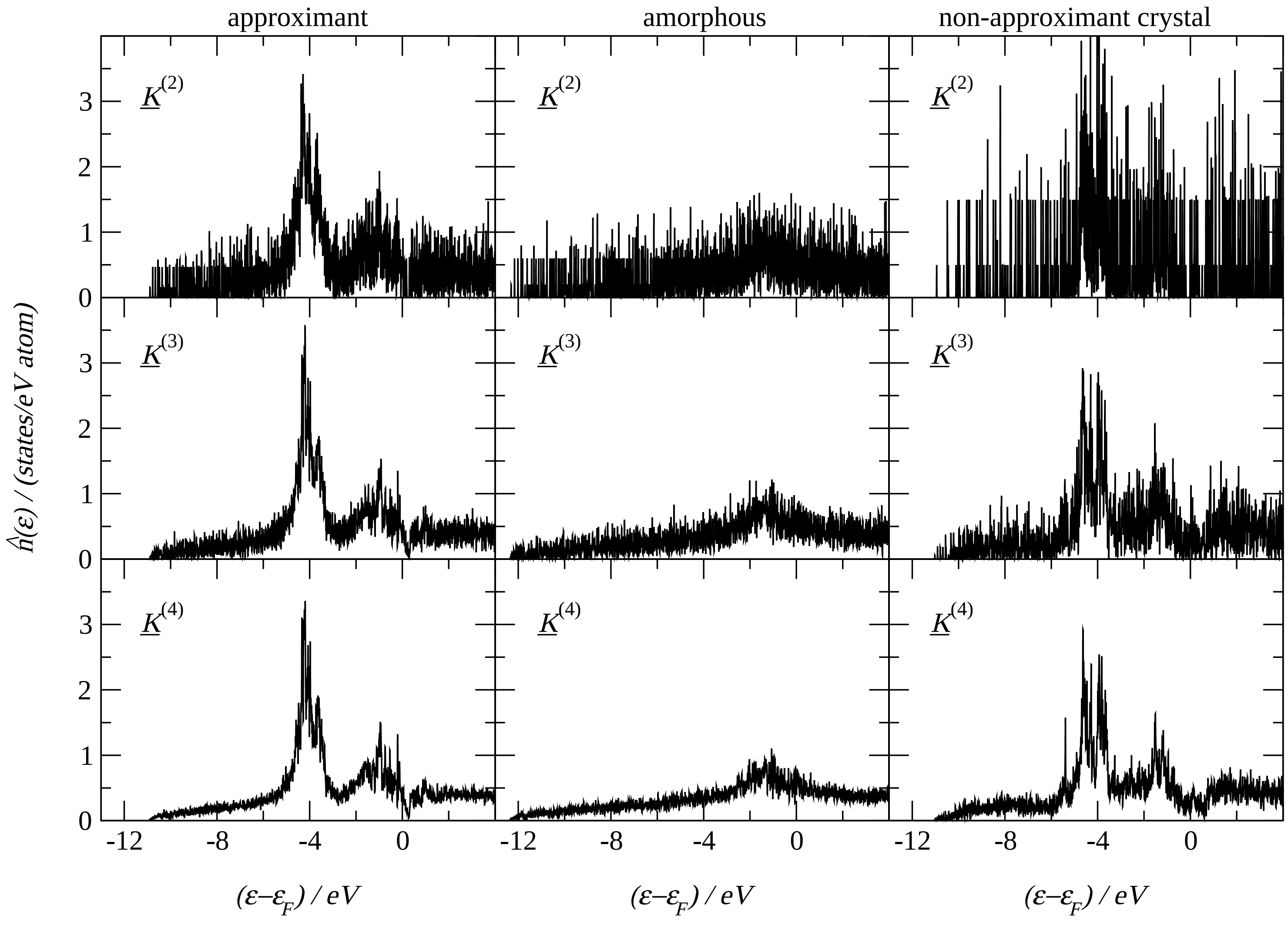

Figure 6.2: Total DOS calculated employing the LMTO-ASA supercell method with high energy resolution. The energy interval is 1 meV for the approximant, and 1.4 meV for the other phases. The DOS is smoothed with Gaussian broadening (half-width $\Sigma = 5$ meV) of the one-particle energies. The number of $\underline{k}$-points increases from top to bottom (see text).

spikes depend on the unit-cell size (number of atoms) and the number of $\underline{k}$-points employed. In the approximant phase, however, some fine structure is not an artifact of the calculation, as shown by Zijlstra [Zijlstra 01]. Moreover, scattered wave cluster techniques ($\underline{r}$-space calculations) indicate the presence of narrow spectral features in the state density due to long-range electronic interferences in the transition metal sub-systems of icosahedral quasicrystals/approximants [Trambly 97, Solbrig 00a]. This means, not all fine structure in approximants/quasicrystals is an artifact of the calculation. However, the separation of realistic spikes and those produced by computational limitations is not straightforward.

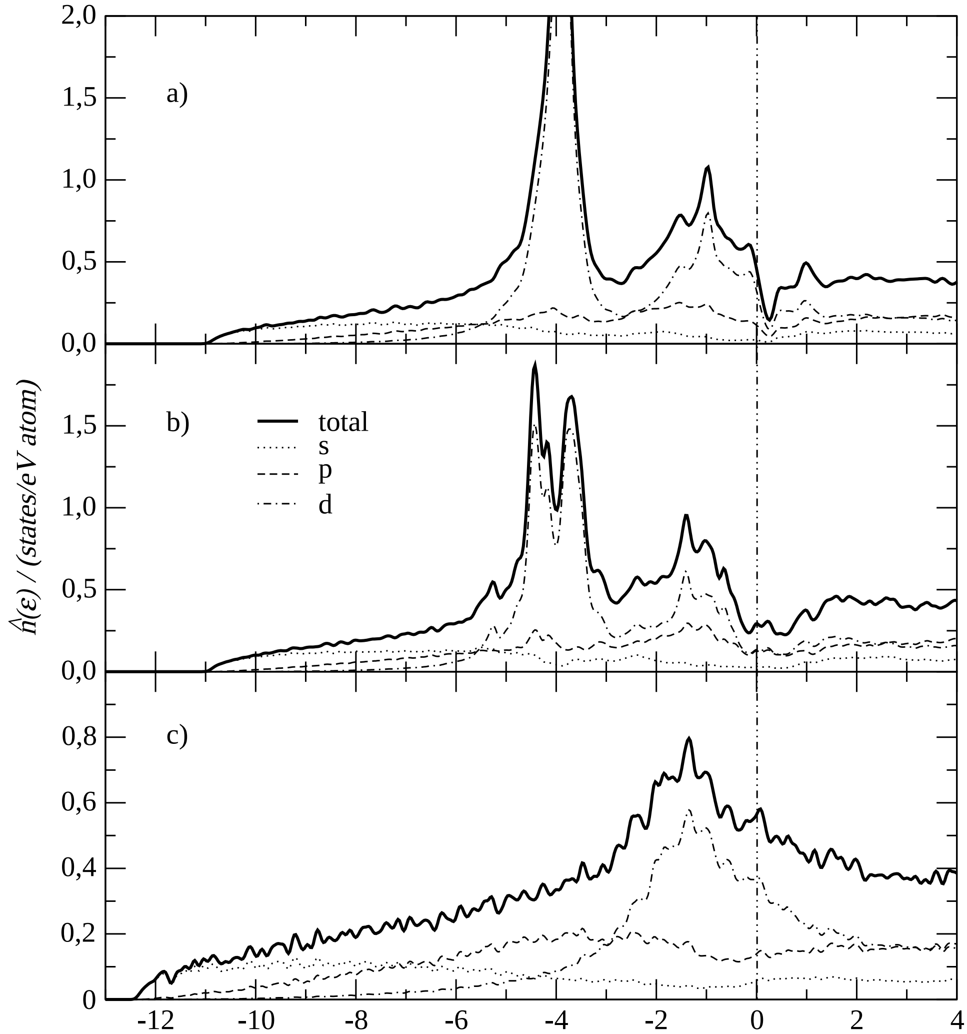

Figure 6.3: Total density of states of three different Al-Cu-Fe phases: a) the Cockayne model of the 1/1 approximant of the icosahedral phase, b) the non-approximant crystalline ω-phase, and c) the modeled amorphous phase. LMTO-ASA supercell calculations: $\underline{K}^{(3)}$ (for the crystalline non-approximant $\underline{K}^{(4)}$), energy interval of 20 meV, and Gaussian half-width of 15 meV.

On the other hand, following the discussion of chapter 4.3, one wants to identify spectral features of the approximant phase that should be presented in the quasicrystal, too. Furthermore, these narrow features must remain after increasing the temperature to be able to explain the *anomalous* transport properties.

One way to avoid the unphysical and/or unstable spikes is to perform a sequence of calculations with growing Gaussian broadening of the one-particle energies (reduction of the energy resolution). Thus, the unphysical and/or unstable spikes will not "survive" after increasing the "temperature" ($2\Sigma \simeq k_B T$). Hence, the remaining spectral feature can be considered as typical for the phase under study. In fact, LMTO-ASA supercell calculations with $\Sigma = 15$meV and energy interval of ~20 meV for the three phases are presented in figure (6.3). As expected, *spikes* are eliminated and spectral features from ~50 meV onwards can be identified. Hereafter, we avoid the spikes employing Σ (Γ) of the order of ~15-20 meV. Correspondingly, the energy interval is increased to ~10-20 meV to reduce the computational time.

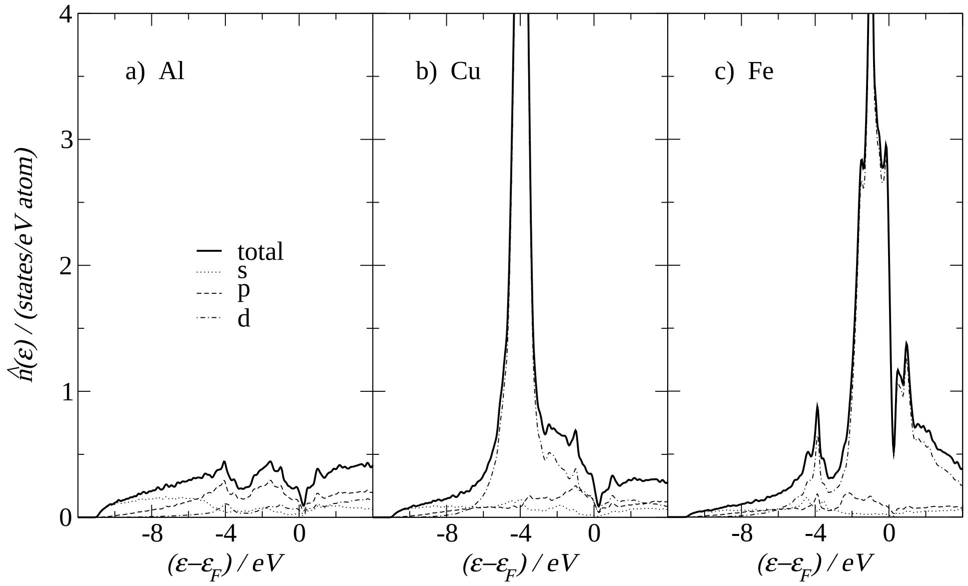

Figure 6.4: Al, Cu, and Fe partial state densities of the i-Al-Cu-Fe approximant phase. The peaks around 4 eV and 1 eV below the Fermi energy are due to d-Cu, and d-Fe orbitals, respectively. LMTO-ASA supercell calculations: $\underline{K}^{(3)}$, energy interval of 20 meV, and Gaussian half-width of 15 meV.

As can be seen in figure (6.3), a pseudogap of the order of ~1 eV is found in the approximant and the crystalline phase. This confirms that both phases are Hume-Rothery stabilized phases[1]. The pseudogap is enhanced by hybridization of sp-Al

---

[1] Really, the amorphous phase is also a Hume-Rothery phase. That means, it has also a pseudogap at the Fermi energy [Traverse 96]. The absence of this pseudogap in our results is attributed to our simple amorphous model (Monte-Carlo with Morse potentials). A more realistic model [Arnold 97] for the amorphous Al-Mn system shows that the DOS have indeed a Hume-Rothery pseudogap.

with d-Fe states. Figure (6.4) shows the partial (Al, Cu, and Fe) DOS of the i-Al-Cu-Fe approximant phase: i) the bottom of the valence band (from -12 eV to -6 eV) is free-electron-like and due to Al atoms, and ii) the peaks around -4 eV, and -1 eV are due to d-Cu, and d-Fe orbitals, respectively. These results are in agreement with previous LMTO-ASA calculations [Trambly 94, Trambly 95] and experimental results [Davydov 98].

In difference to the amorphous and the non-approximant crystal, the approximant phase has a narrow pseudogap of the order of ~150 meV, see figure (6.3). Note that this narrow pseudogap is also present on the partial state densities, see figure (6.4). In the following, we will discuss about the origin, stability, and influence of this spectral fine structure on the *anomalous* electronic transport of approximants/quasicrystals.

Transport depends on both the number and the character of carrier states

In relation with the discussion of chapter 3.2, here will be shown that not only the amount of participating states but also the kind of the states are important to determine the metallic or non-metallic character of the material considered. Furthermore, the influence on the resistivity of the narrow DOS-pseudogap in the approximant phase will be studied. For this end, the spectral properties, such as the resistivity, diffusivity, state density, and participation ratios, of the approximant phase are compared with the amorphous and the non-approximant crystalline phases.

The spectral conductivity/resistivity, and the electronic diffusivity are calculated employing the eigenvalues and eigenfunctions obtained from the LMTO-ASA supercell method together with the Kubo-Greenwood formula (3.5), and the Einstein relation (3.8), respectively. The participation ratio indicates the part of sites *participating* with a substantial amplitude in a wave function. It is defined as,

$$P(\varepsilon) = \frac{1}{N} \frac{\left(\sum_i c_i^2\right)^2}{\sum_i c_i^4} \quad , \tag{6.1}$$

where N is the number of sites per unit cell multiplied by the number of orbitals (e.g. 3 for s, p, d orbitals), and the c's are the coefficients in the orbital expansion of the electronic wave function, see equation (5.17) or (B.9). The participation ratio has two limiting cases: i) when only one coefficient c_i is different of zero, then $P(\varepsilon) \to 1/N$ (if $N \to \infty$ then, $P(\varepsilon) \to 0$), and ii) when each coefficient $c_i = 1/\sqrt{N}$, then $P(\varepsilon) \to 1$. The first case describes a pseudo-localized wave function (remember that the lattice periodicity does not permit to speak about true localization). The second case describes a wave function distributed homogeneously on all sites of the unit cell (considering the periodicity, over all crystal sites).

Figure (6.5) summarizes the results for the three phases: the approximant, amorphous, and the non-approximant crystal. The total DOS, shown in figure (6.3), is

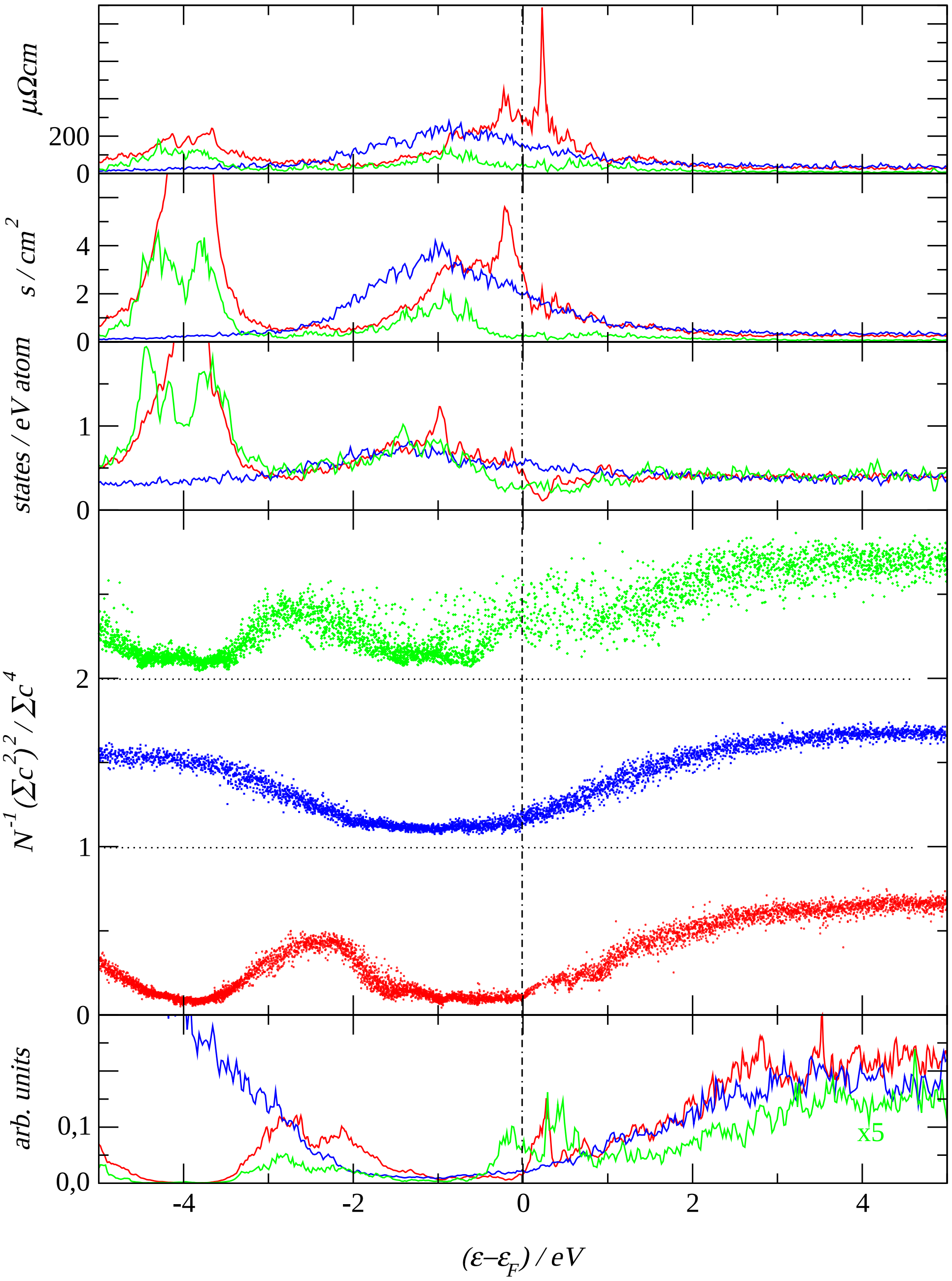

Figure 6.5: Spectral properties of Al-Cu-Fe phases. From top to bottom: resistivity, inverse of the diffusivity, density of states, participation ratios (each curve has been shifted upwards by 1), and a measure of the velocity matrix elements, σ/n^2, of the 1/1 approximant (red), amorphous (blue), and crystalline non-approximant (green) phases. LMTO-ASA supercell calculations: $\underline{K}^{(3)}$ (for the crystalline non-approximant $\underline{K}^{(4)}$), energy interval of 10 meV, and Lorentzian half-width of 20 meV.

here presented in the energy range ±5 eV around the Fermi energy. As expected, the spectral resistivity at the Fermi energy grows in the sequence non-approximant crystal, amorphous phase, approximant. A wide d-Fe peak around the Fermi energy is found in the amorphous and approximant phases. The d-Cu peak at 4 eV below the Fermi energy has no direct consequences for the transport, i.e. disorder, temperature, or deviations in the stoichiometry are not able to shift the Fermi energy down to these energies. A narrow peak, at 0.23 eV above the Fermi energy, in the approximant phase has no counterparts in the other phases. We believe that this spectral fine structure is responsible for the *anomalous* transport of approximants/quasicrystals, as will be shown below. The Fermi energy can well be shifted to this region by defects [Pierce 93a]. On the other hand, the electronic diffusivity at the Fermi energy of the approximant is $D \approx 0.36\ cm^2/s$ which is in reasonable agreement with experimental results such as $D \approx 0.3\ cm^2/s$ [Klein 91].

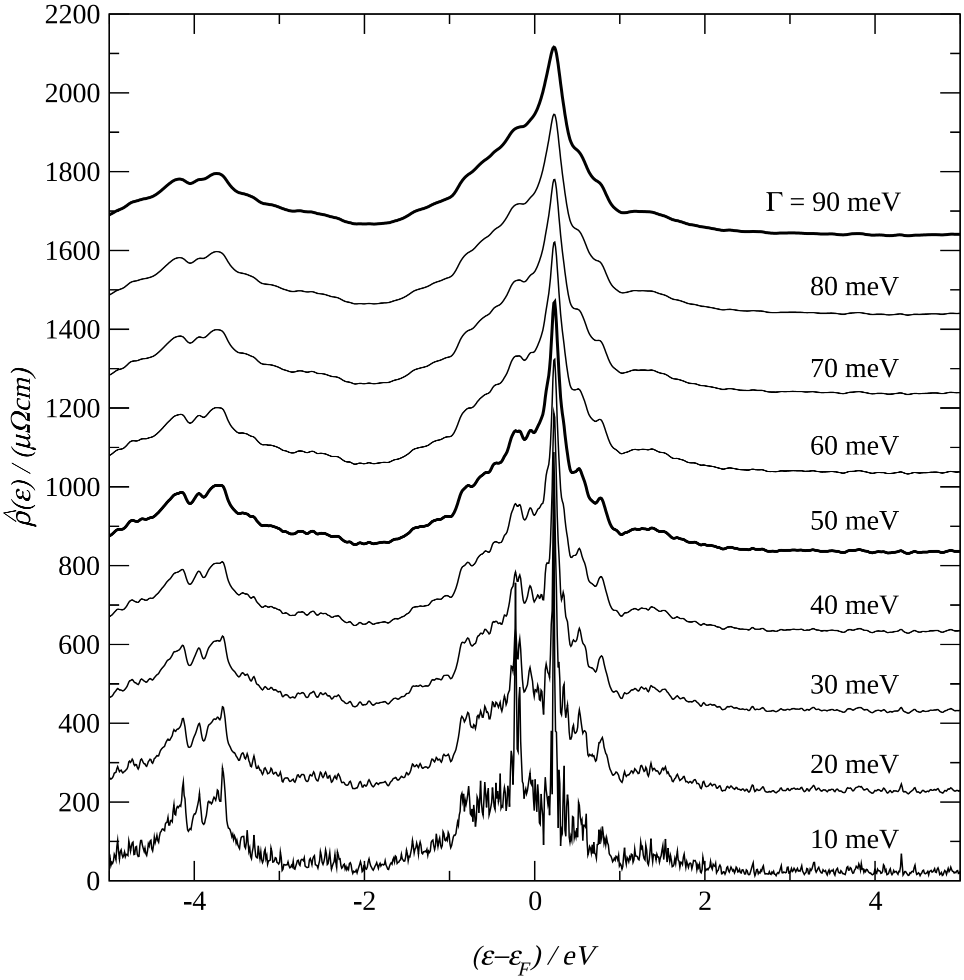

Figure 6.6: i-Al-Cu-Fe approximant, spectral resistivity calculated for growing Γ. Each curve has been shifted upwards by 200 $\mu\Omega cm$. LMTO-ASA supercell calculations: $\underline{K}^{(3)}$, energy interval of 10 meV.

The conductivities in a group of phases are Mott-like, i.e. $\widehat{\sigma} \sim \widehat{n}^2(\varepsilon_F)$, if they are controlled by the amounts of states which are available close to ε_F. The states themselves are equally composed. This is indicated by missing energy dependence of the on-energy shell velocity matrix elements, $\widehat{M}^2 \propto \widehat{\sigma}/\widehat{n}^2$, of each phase[2]. This measure of the velocity matrix elements is drawn in figure (6.5) for the three Al-Cu-Fe phases. It can be seen that $\widehat{\sigma}/\widehat{n}^2$ changes strongly with the energy, especially for the non-approximant crystal and the approximant. That means, they are not Mott-like systems. As expected, the velocity matrix elements follow the participation ratios: different compositions of states are indicated by the participation ratios (6.1), then, it is expected that both $P(\varepsilon)$ and $\widehat{\sigma}(\varepsilon)/\widehat{n}^2(\varepsilon)$ behave similarly. With respect to the participation ratios, note that the self-consistently determined ε_F lies exactly between d dominated states below ε_F, and sp dominated states above ε_F. Thus, participation of d-Fe orbitals give rise to rapid spectral changes of the character of states.

As was pointed out above, the main difference between the approximant phase and the other ones is the narrow peak, at 0.23 eV above ε_F, found on the spectral resistivity, see figure (6.5). We believe that this fine structure provides the *anomalous* transport properties of the approximant/quasicrystal in a wide temperature range. This can be realized increasing the Lorentzian broadening (half-width Γ) of the energy delta-functions, see equations (3.5) and (3.7). Figure (6.6) shows spectral resistivity curves of the approximant phase for a few selected Γ values[3]. Rising Γ causes the spectral fine structure to be smeared out. Note that the peak at 0.23 eV above ε_F survives increasing Γ but its height and width are lowered and enlarged, respectively. Figure (6.7) shows the inverse heights of the two prominent fine-structure peaks in figure (6.6) (at $\sim \pm 0.2$ eV), i.e. $\widehat{\rho}_{max}^{-1}$ plotted versus Γ. Two scaling regimes are found: i) $\widehat{\rho}_{max}^{-1} \propto \Gamma^{1/4}$ at large Γ, and ii) $\widehat{\rho}_{max}^{-1} \propto \Gamma^2$ below a cross-over, $\Gamma_{cr} \sim 5$ eV, for both peaks. As was discussed in chapter 3.2, the second regime is *unphysical* because Γ is less than the average level distance, $\delta\varepsilon$, and thus only the product of the two delta (Lorentz) functions in equation (3.5) appears in figure (6.7) below Γ_{cr}.

The extrapolation of the scaling at $\Gamma > \Gamma_{cr}$ down to $\Gamma \sim 0.1$ meV provides resistivities in the range of 1500-3000 $\mu\Omega cm$. Such resistivities may be reached in the quasicrystal at ~1.2 K provided that the level distribution of the 1/1 approximant can be transferred to the smaller energy scale (self-similarity). In fact, due to $\delta\varepsilon \propto 1/N_a$, with N_a the number of atoms in the unit cell, increasing the order of the approximant (and hence N_a), Γ_{cr} shifts to smaller values.

Following Fujiwara *et al.* [Fujiwara 96] (see the discussion of chapter 3.2), the Γ-dependence of $\widehat{\rho}_{max}^{-1}$ can be related to the anomalous transport. Then, comparing the behavior of $\widehat{\rho}_{max}^{-1}$ for $\Gamma > \Gamma_{cr}$ with $\widehat{\rho}_{max}^{-1} \propto \Gamma^{1-2\beta}$ (see equation (3.10)), one ob-

---

[2] The Kubo-Greenwood formula (3.5) can be rewritten as, $\widehat{\sigma} \propto \widehat{n}^2(\varepsilon)\widehat{M}^2(\varepsilon)$ where $\widehat{M}^2(\varepsilon) = \overline{|\langle i(\varepsilon)|v|j(\varepsilon)\rangle|^2}^{ij}$ is an average of the square of the velocity matrix elements $\langle i(\varepsilon)|v|j(\varepsilon)\rangle$. $|i(\varepsilon)\rangle$ is the electronic wave function with energy eigenvalue ε.

[3] Calculations with Gaussian broadening of the energy delta-functions provides similar results.

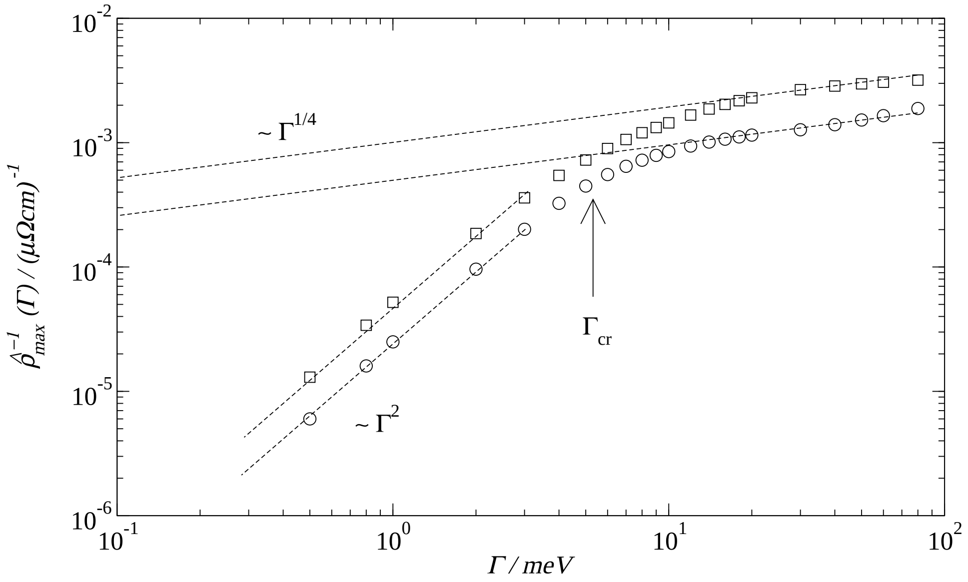

Figure 6.7: i-Al-Cu-Fe approximant, log-log plot of the inverse of resistivity-peaks, $\widehat{\rho}^{-1}_{max}$, versus Γ. For high values of $\Gamma > \Gamma_{cr}$, we find $\widehat{\rho}^{-1}_{max} \propto \Gamma^{1/4}$. Extrapolations of the $\Gamma > \Gamma_{cr}$ scaling down to $\Gamma \approx 0.1$ meV provides resistivities in the range of 1500-3100 $\mu\Omega cm$.

tains $\beta = 3/8$, which is less than $1/2$ (the diffusive case). That means, the electron propagates sub-diffusively[4]. Similar results have been found [Fujiwara 96, Roche 98] in sequence of approximants to the d-Al-Cu-Co quasicrystal.

Structure and the importance of the chemical order

It was shown above that the spectral fine structures in the approximant phase are connected with anomalous diffusion and rapid changes of the characters of the states. In the following we will see that the chemical order of the sub-system of Fe atoms is responsible for the narrow features of the spectral resistivity and the state density. It turns out that the quasiperiodic order alone cannot provides the *anomalous* transport properties expected in quasicrystals/approximants. A right chemical decoration is also necessary.

For this purpose, the original Cockayne model, OCM, will be modified only in its chemical decoration (the atomic positions remain unchanged). From the chemical decoration of the table (6.1), two alternative decorations are derived: i) the Al(4) positions are interchanged with the Fe(2) positions (modified Cockayne model 1, MCM1), and ii) the Fe atoms, Fe(1) and Fe(2), are decorated with Al atoms providing a two component Al-Cu system (modified Cockayne model 2, MCM2).

---

[4] For comparisons, similar scaling analysis was carried out in a 100 atom model of liquid aluminium at 950 K. In this case, the obtained $\beta \approx 0.725$ indicates a super-diffusive motion. Remember that $\beta = 1$ corresponds to ballistic transport.

The narrow peak of the spectral resistivity of OCM, related to a narrow pseudogap in the state density, is reduced on changing the decoration of the Fe atoms (MCM1), as shown in figure (6.8). The model MCM2 has low resistivities without fine spectral features around the Fermi energy. Correspondingly, the state density does not show pseudogaps. The behavior of the spectral resistivity of the MCM2 model is similar to the non-approximant crystal studied above, see figure (6.5). This confirms the importance of the Fe sub-system and it indicates also that quasiperiodicity alone cannot explain the high resistivities found in the Al-Cu-Fe approximant/quasicrystal. Similar results are also found in low order approximants of the icosahedral Penrose tiling (see appendix C).

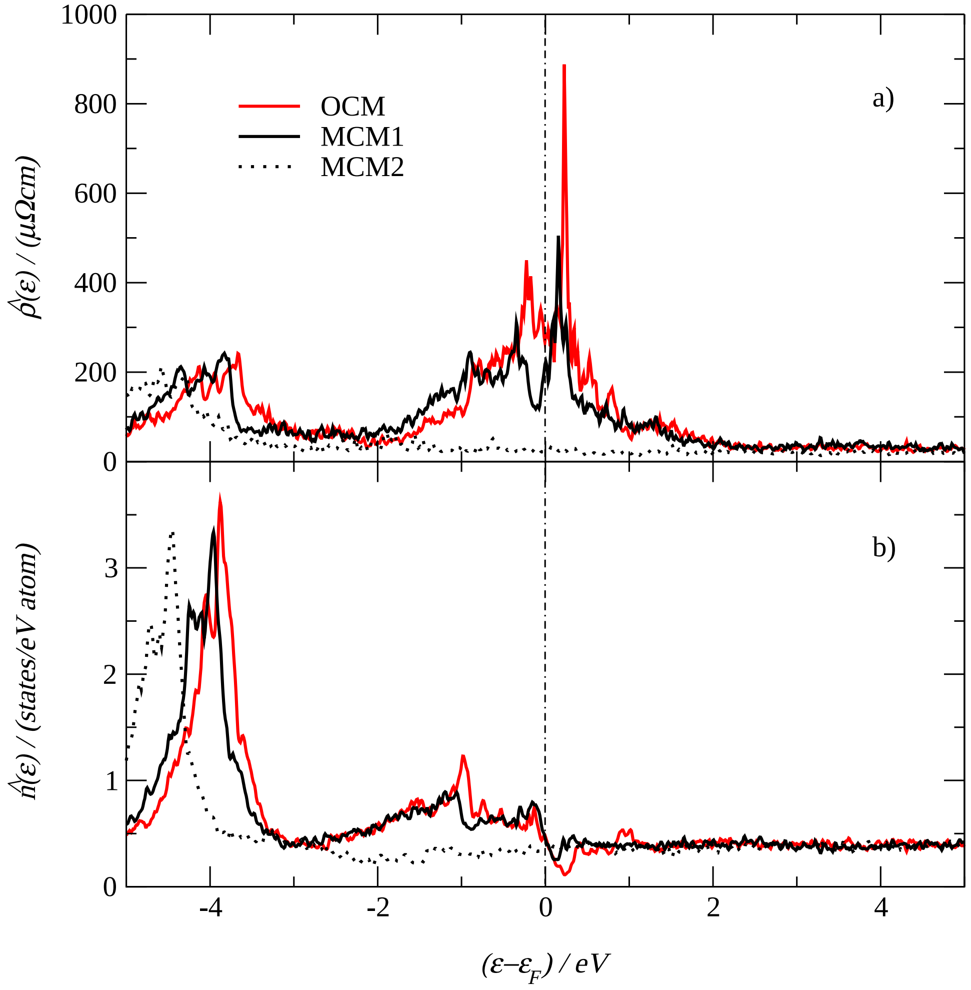

Figure 6.8: Spectral properties of different decorations models of the Al-Cu-Fe approximant. a) resistivities, and b) densities of states of different decorations models (OCM, MCM1, MCM2) of the 1/1 approximant phase, see text for details. LMTO-ASA supercell calculations: $\underline{K}^{(3)}$, energy interval of 10 meV, and Lorentzian half-width of 20 meV.

The results of figure (6.8) show that the spectral features are sensitive to the chemical decoration of the Bergman cluster, more precisely, to the structure of the Fe sub-system. In fact, surprisingly the Fe atoms form a Fibonacci-like (lsl with $l/s = \tau^* = (\sqrt{5}+1)/2$) planar order in three perpendicular directions (see figures (6.1) and (6.9)), which is destroyed on changing the decoration (models MCM1, MCM2). Moreover, the distance between two Fe atoms in the inner icosahedron of the Bergman cluster is ∼4.37 Å, which is reduced in MCM1 to ∼2.76 Å. In summary, fine structures of the spectral resistivity are due to a Fibonacci-like planar order without direct contact of Fe atoms. These result are in agreement with the recent work of Solbrig and Landauro [Solbrig 00a]. They employed a cluster recursion muffin-tin scattered wave method to show that long-range electronic interferences in the Fe sub-system (active atoms, strong scatterers) gives rise to narrow spectral features around the Fermi energy. The aluminium atoms are not active (weak scatterers) and only re-define the vacuum level. Confirming these results, cluster recursion techniques with TB-LMTO Hamiltonians do not show fine structure on the state density and electronic diffusivity due to the short-range character of this basis (c.f. figure (10.3)) as discussed in chapter 10.

This all should explain why in Al-TM quasicrystals the high resistivity depends strongly on concentration changes of transition metals with the d-resonance close to the Fermi energy and on the annealing treatments. There is an optimum concentration and/or annealing process where the Fe atoms are distributed as to hinder the transport. It is worth noting that the electronic transport of icosahedral quasicrystals without transition metals does not seem *anomalously* different to those of metallic systems (see [Poon 92], for instance). This indicates that anomalies on the transport of quasicrystals are due to transition metals.

Fibonacci-like stacking of transition metal atoms

In the following, we study the conductance of i-Al-Cu-Fe approximant bars employing the Landauer/Büttiker approach, described in chapter 5. Related attempts for two dimensional Penrose tilings deal with large length scales by means of one-orbital tight-binding approaches [Tsunetsuga 91, Yamamoto 95b]. As discussed in chapter 5, tight-binding models put emphasis on structure, chemical aspects are disregarded. The present study is closely related to the work of Solbrig *et al.* [Solbrig 00b] of the α-Al-Mn-(Si) approximant, where both aspects, structure and chemical order, are considered.

Moreover, the results obtained previously by means of the LMTO supercell method and the Kubo-Greenwood formula can be tested. In fact, two points considered in the previous results can be analysed: i) if the approximant cell is large enough to account for transport relevant coherence, and ii) the use of the same boundary conditions to the transport direction and to the transverse directions.

For this purpose, we prepare bars of the unit cell of the i-Al-Cu-Fe approximant: arbitrary length d, and cross-section $A = a^2$ (a is the lattice constant), see figure (6.9). The self-consistent effective atoms of the LMTO-ASA supercell approach are employed (energy-dependent phase shifts for Al, Cu, and Fe). Only the Fe atoms are strong scatterers close to the Fermi energy. Hence, the electronic transport must critically depend on the coherence in the Fe sub-system.

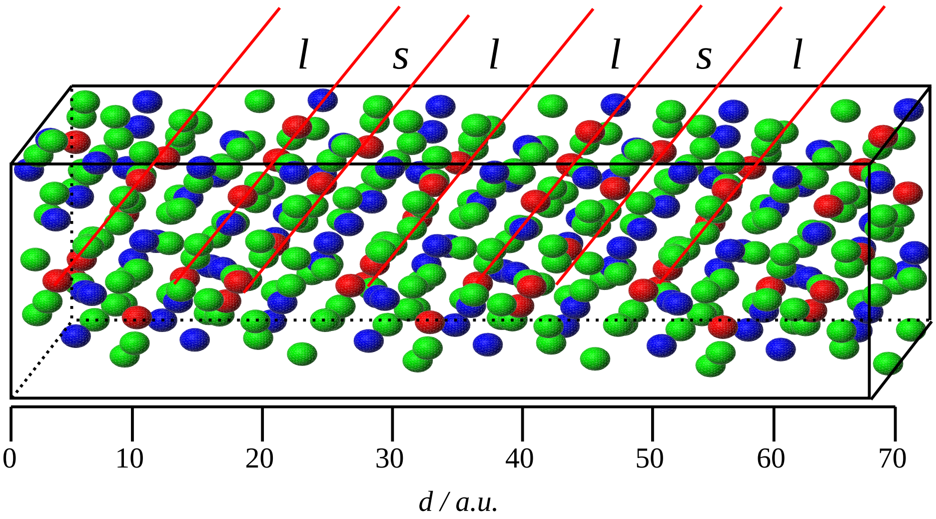

Figure 6.9: Bars of the i-Al-Cu-Fe approximant for Landauer/Büttiker calculations. Note the Fibonacci-like planar order of the Fe atoms: $lsllsl...$ with $l/s = \tau^* = (\sqrt{5}+1)/2$. This Fibonacci-like arrangement of Fe atoms is presented in three perpendicular directions. The box and lines are only guides for the eyes. 1 a.u.=0.529177 Å.

Figure (6.10) shows resistances $R = G^{-1}$ versus the length d in the valence band for different $k_{||}$-values which belong to the transverse two-dimensional Brillouin zone. Two regions can be found: one unit cell (up to ∼23 a.u.) and beyond the unit cell. In the first region, i.e. $0 < d/a.u. < 23$, we find: i) R rises stepwise once strong scatterers are added to the sample, i.e. Fe atoms in the d-Fe band. ii) The resistance scales ohmic-like on the average, $R = \rho(d/A)$.

Beyond the unit cell, i.e. $24 < d/a.u. < 55$, drastic changes appear for energies in the d-Fe band: i) Close to the Fermi energy (at ∼100 meV above it), non-ohmic resistance is found, $R \propto d^{\nu}$ with $\nu \simeq$2.1-3.1 (for one-dimensional Fibonacci lattices, this is directly related to the critical nature of the wave functions [Kohmoto 86]). In some cases (see figure (6.10)), an exponential behavior is found, which reminds localization in quasi-1D samples. Note that these localization trends start at remarkably small d. For other energies the ohmic-like behavior remain unchanged. This strong dependence of the resistance on the energy is closely related to rapid spectral changes of the character of states due to the fluctuating participation of d-Fe orbitals (c.f. figure (6.5)). ii) The peculiar behavior reduces drastically on introducing chemical disorder (change of the decoration, model MCM1). As discussed above, after changing the decoration, the Fibonacci-like order of Fe atoms (see figure (6.9)) is destroyed and the direct Fe-Fe contact reduces the resistance[5], see figure

---

[5] To test the importance of the decoration, we prepare slabs in a Fibonacci arrangement, which are decorated with Al or Fe atoms. The decoration with Al atoms (weak scatterers) provides

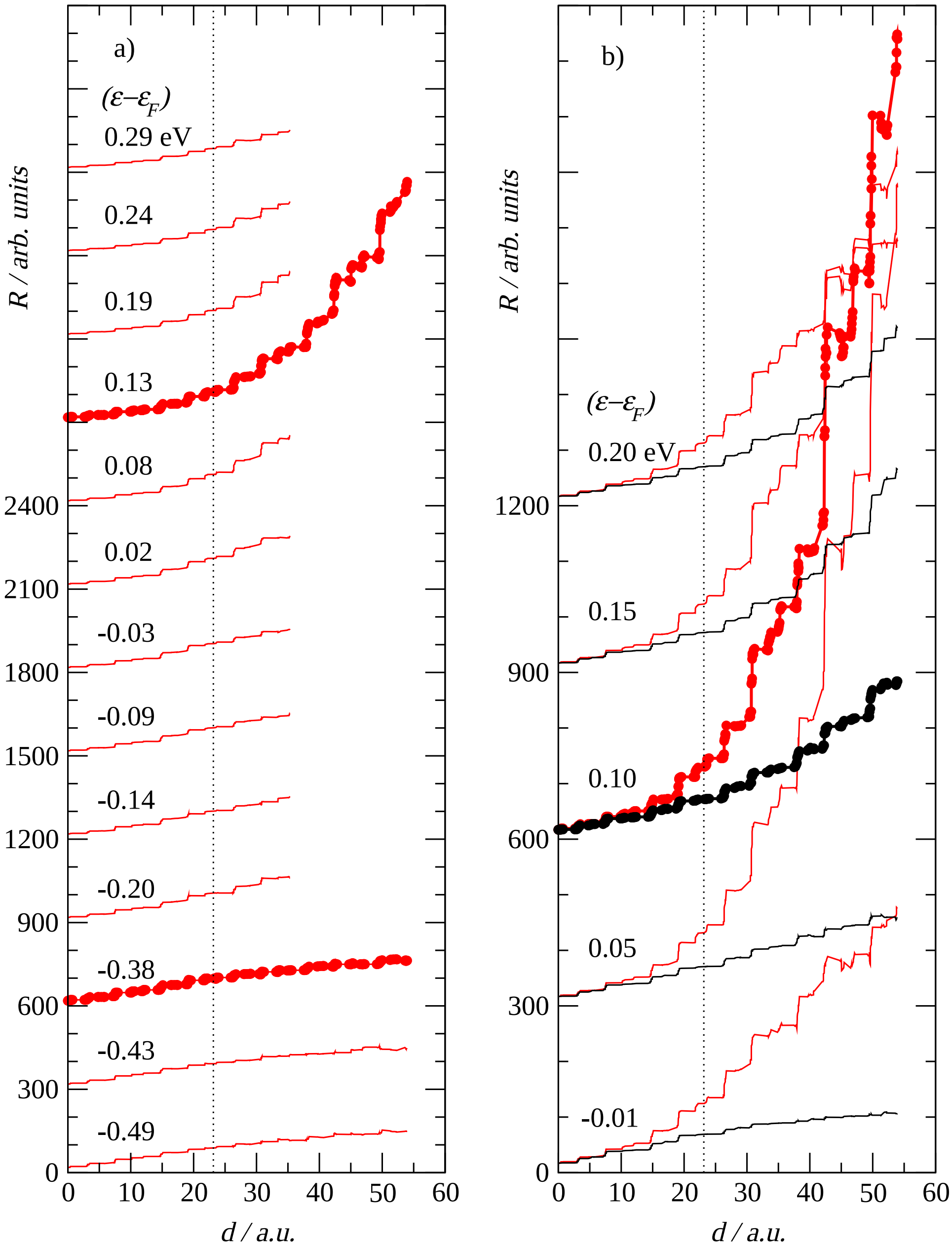

Figure 6.10: i-Al-Cu-Fe approximant, Landauer/Büttiker resistance for two different $\underline{k}_{||}$-values of the two-dimensional Brillouin zone: a) $\underline{k}_{||} = (0.370, 0.740)\pi/a$, and b) $\underline{k}_{||} = (0.875, 0.875)\pi/a$ (a is the lattice constant), at a few energies relative to ε_F (the Fermi energy obtained from the LMTO-ASA supercell method). Two decorations of the i-Al-Cu-Fe approximant are presented: the original Cockayne model (OCM, red), and the modified Cockayne model 1 (MCM1, black). Each curve has been shifted upwards by 300 (arb. units).

(6.10). These results are in agreement with the work of Solbrig *et al.* [Solbrig 00b] in the α-Al-Mn-(Si) approximant, where Fibonacci-like planar order of Mn atoms are responsibles for non-ohmic resistances, as described here.

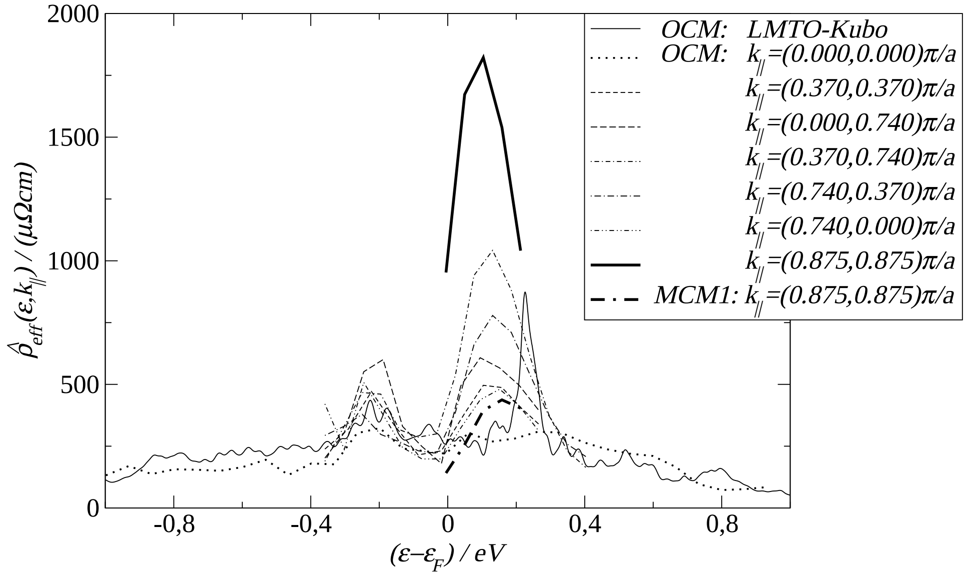

Figure 6.11: i-Al-Cu-Fe approximant, *"effective"* resistivities from the resistance scaling just beyond one unit cell for different $\underline{k}_{||}$-values. Two peaks are found similar to the LMTO-Kubo results. See text for details.

In the range 25-35 a.u. (just beyond one unit cell), the average slopes of the resistances are characterized in figure (6.11) by *"effective"* resistivities, $\widehat{\rho}_{eff}(\varepsilon, k_{||})$, which are not material properties in the common sense. They depend markedly on $\underline{k}_{||}$ and attain magnitudes of the order of $\sim$1800 $\mu\Omega cm$. Moreover, in comparison with LMTO-Kubo results, a two-peak feature is found. The peak positions are nearly independent of $\underline{k}_{||}$.

Correlated anomalies of transport coefficients

Two points will be discussed. The first one treats the relation between the spectral conductivity and the Hall coefficient. The second point refers to Fermi energy shifts caused by deviations in the stoichiometry or by defects in both structure and decoration. Thus, we will be able to study temperature dependence of electronic properties of the approximant/quasicrystal considering the narrow spectral features found above.

The narrow peak of the spectral resistivity in the i-Al-Cu-Fe approximant, figure

---

only ohmic-like resistances, whereas the decoration with Fe atoms (strong scatterers) provides a behavior similar to that described here for the i-Al-Cu-Fe approximant (decorations models OCM, MCM1). This indicates, once more, that the quasiperiodicity (Fibonacci order) alone can not explain the *anomalous* transport in quasicrystals: the right decoration is also required.

(6.5), is related to a specific 100 meV conductivity pseudogap ($\widehat{\sigma}(\varepsilon) = \widehat{\rho}^{-1}(\varepsilon)$) in addition to the ∼1 eV Hume-Rothery type feature. With a higher resolution, the energy range of the specific narrow pseudogap is reproduced in figure (6.12). Moreover, the Hall coefficient, $\widehat{R}_H(\varepsilon) = \widehat{\sigma}_H(\varepsilon)/\widehat{\sigma}^2(\varepsilon)$ [Cusack 87], is presented where equation (A.15) is employed as a spectral formula ($T \to 0$) with the *ansatz* (B is a magnetic field in the z-direction, correspondingly, the external and Hall electric fields are in the x-direction and in the negative y-direction, respectively)

$$\widehat{\sigma}_H(\varepsilon) = \widehat{\sigma}_{xy}(B,\varepsilon)/B \approx Q\left(-\frac{d\widehat{\sigma}(\varepsilon)}{d\varepsilon}\right) \quad . \tag{6.2}$$

It is worth noting that *ab-initio* calculations of the transverse electronic conductivity $\widehat{\sigma}_{xy}(B,\varepsilon)$ is not an evident task due to the *uncomfortable* form of the magnetic Hamiltonian (for instance see [Morgan 85, Cusack 87]). Moreover, it is not conclusively clear whether the magneto-transport can be explained as an on-the energy-shell transport, i.e. it should depend only of the nature of the states at the Fermi energy [Morgan 85, Itoh 92]. Note that in equation (6.2) off-shell information is included due to the energy derivatives.

The final step in equation (6.2) with the positive constant Q is not rigorous[6], as explained above. Originally Bush *et al.* [Bush 74] have suggested to relate R_H to the energy derivative of the state density. This has also proved successful for quasicrystals [Pierce 93a]. In an energy range where the spectral diffusivity, $\widehat{D}(\varepsilon)$, is almost constant (e.g. around the narrow peak of the spectral resistivity, see figure (6.5)) the Einstein relation (3.8), allows the transition to $d\widehat{\sigma}(\varepsilon)/d\varepsilon$ as proposed in equation (6.2).

It has been shown that several i-Al-Cu-Fe phases close to the quasicrystalline stoichiometry (12-13 at.% Fe) have almost the same electronic diffusivities [Sahnoune 92]. Very recently Houari *et al.* [Houari 00] have re-examined this problem. For substitutional disorder and weak scattering they confirm that the sign of R_H is related to -$d\widehat{n}(\varepsilon)/d\varepsilon$. With topological disorder and strong scattering, however, positive R_H instead occurred in connection with more localized electron states. The above ansatz accounts for such extensions via energy-dependent diffusivity. In other words, it is more realistic to employ the spectral conductivity in the *ansatz* (6.2) instead of the state density, because, the first one considers not only the amount of the states but also their character.

Figure (6.12) shows a conductivity pseudogap (width ∼100 meV) that is narrower than the corresponding DOS pseudogap (width ∼150 meV), and, in agreement with equation (6.2), $\widehat{R}_H(\varepsilon)$ changes its sign just at the conductivity minimum. In this energy region, the character of the electronic states varies rapidly from d-Fe dominated below the Fermi energy to *sp* dominated above (see the rapid varying participation ratios in figure (6.5)). In agreement with Houari's work [Houari 00] we find that

---

[6] In the framework of the Bloch-Boltzmann theory one can show [Solbrig] that Q accounts for a weak energy dependence of the diffusivity after neglecting off-diagonal transport quantities.

positive Hall coefficients occur where the states are more localized due to the high *d* content.

The Fermi energy of real approximant crystals may be shifted on the scale 100 meV with respect to ε_F^{sc} which is the self-consistent value of the perfect approximant. Such shifts are caused by deviations in the stoichiometry or by defects in both structure and decoration [Pierce 93a]. Solbrig *et al.* found [Solbrig 00b], for α-AlMn(Si) with defects in the Al *glue*, shifts of just this order. In the sections to follow we refer to the trial positions A and B of the *real Fermi energy* as indicated in figure (6.12). Note that there is experimental evidence [Lindqvist 93] for the Fermi energy to pass

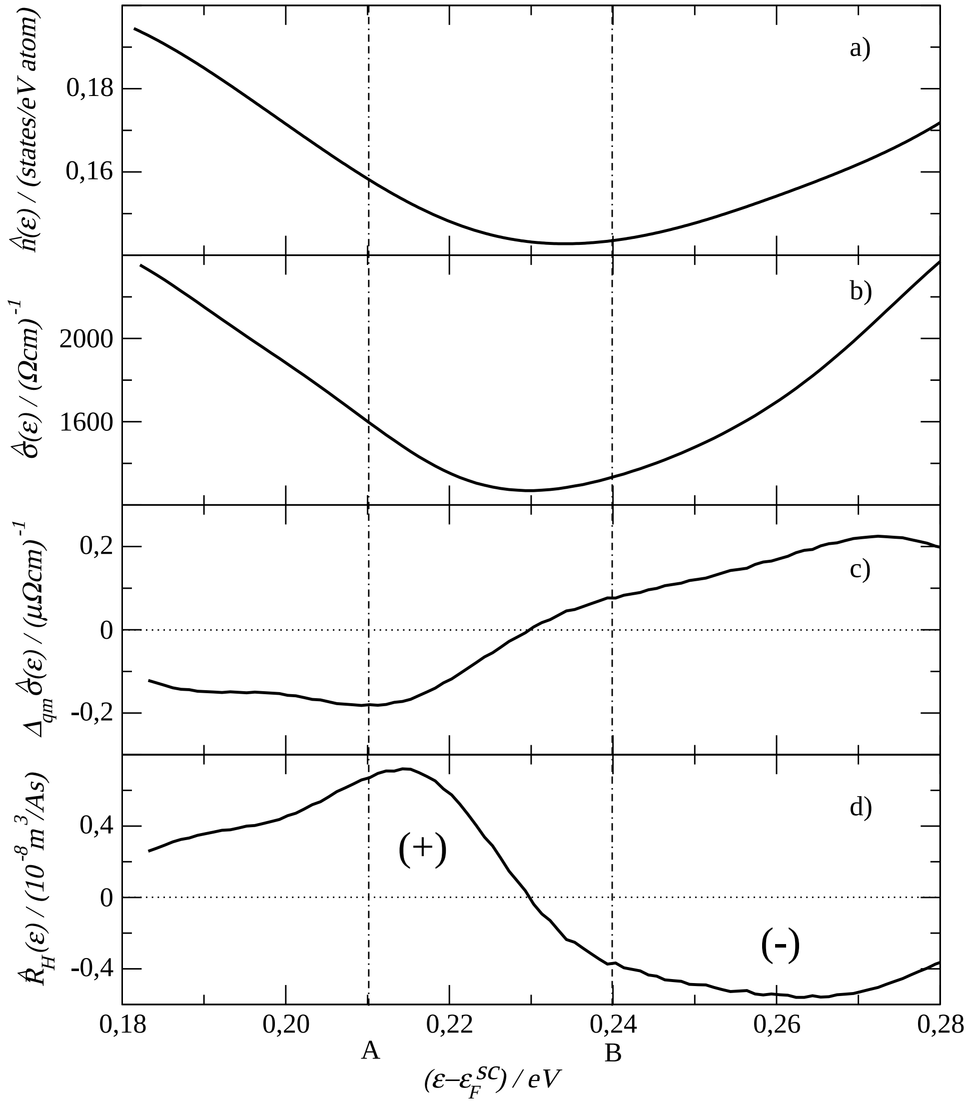

Figure 6.12: i-Al-Cu-Fe approximant, the range of the narrow pseudogap: a) total density of states, b) spectral conductivity, c) change of the spectral conductivity on the quantum mechanical energy scale, and d) the Hall coefficient (obtained for a chosen $Q = 6 \times 10^{-5} Am^2$). ε_F^{sc} is the self-consistent Fermi energy (obtained from LMTO-ASA supercell calculations).

a spectral conductivity minimum along a stoichiometric phase sequence. The Hall coefficient behaves just as shown in figure (6.12). Examples for type A and type B positions of the Fermi energy are $Al_{62.5}Cu_{24.5}Fe_{13}$ respectively $Al_{63.5}Cu_{24.5}Fe_{12}$ [Pierce 93a].

6.2 Temperature dependent properties of the approximant phase

Modeling the spectral resistivity

Models of the spectral conductivity have been employed to explain the temperature dependence of the transport coefficients, equations (A.11)-(A.15). The first one, is the simple conductivity minimum, equation (3.11), proposed by Mott [Mott 87]. It is employed to explain the thermally activated temperature dependence of the conductivity in systems in the metallic limit, see chapter 3.3.

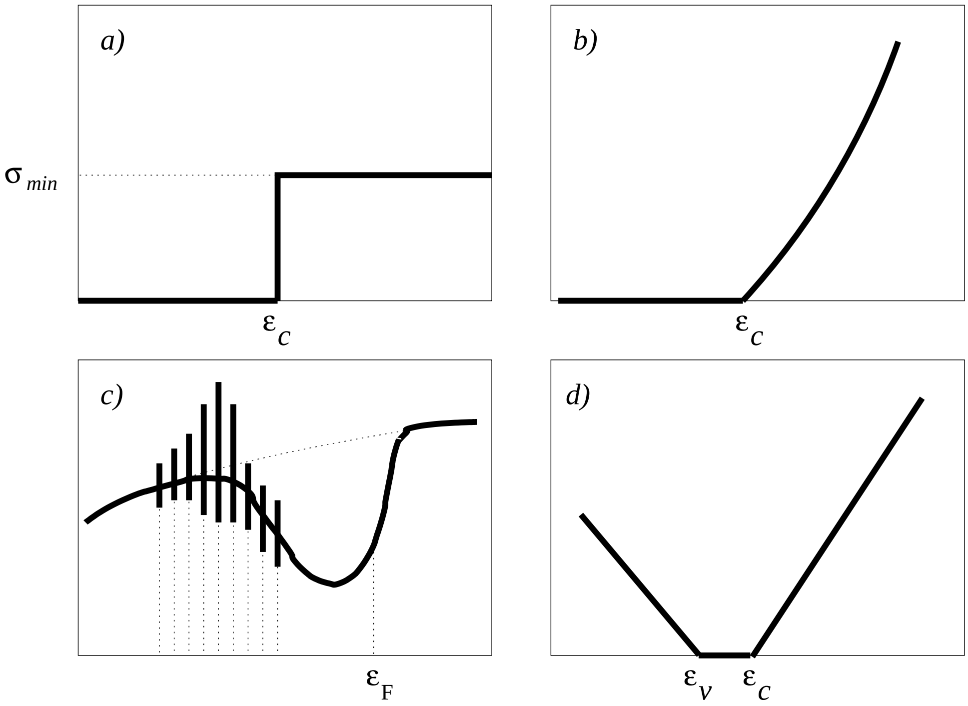

Figure 6.13: Schematic representation of different spectral conductivity models: a) the minimum metallic conductivity for thermally activated systems, b) a model for systems near the metal-insulator transition, c) a model for quasicrystals considering a self-similar *spiky* structure, and d) a model for liquid semiconductors. See text for details.

For systems with the Fermi energy around the mobility edge, ε_c, at which the metal-insulator transition occurs, one employs $\widehat{\sigma}(\varepsilon) = \sigma_0(\varepsilon - \varepsilon_c)^\nu$ for $\varepsilon \geq \varepsilon_c$, otherwise $\widehat{\sigma}(\varepsilon) = 0$, where σ_0 is a constant, and ν is the conductivity index [Enderby 94, Villagonzalo 99]. Experiments near the metal-insulator transition in amorphous materials show a similar behavior of the conductivity with concentration changes (for instance see [Lauinger 95]).

Enderby and Barnes [Enderby 90] employed a similar model for the spectral conductivity of liquid semiconductors at very high temperatures: $\widehat{\sigma}(\varepsilon) = \alpha_v(\varepsilon_v - \varepsilon)$ for $\varepsilon < \varepsilon_v$, and $\widehat{\sigma}(\varepsilon) = \alpha_c(\varepsilon - \varepsilon_c)$ for $\varepsilon > \varepsilon_c$, otherwise $\widehat{\sigma}(\varepsilon) = 0$, where α_v, α_c are constants. The energy gap, measured by $\varepsilon_g = \varepsilon_c - \varepsilon_v$, takes values from 0 to 500 meV [Enderby 90]. These different models are schematically shown in figure (6.13).

In quasicrystals, experiments [Pierce 93a, Pierce 93b] of temperature dependent conductivity and thermopower indicate the presence of a pseudogap (width ~0.1-0.2 eV) in the spectral conductivity. Pierce *et al.* fitted the conductivity employing a parabolic spectral conductivity, which simulates a spectral conductivity pseudogap [Pierce 93b]: $\widehat{\sigma}(\varepsilon) = A + B|\varepsilon - \varepsilon_F|^2$. The attempts to fit the thermopower give *arbitrary* results. However, the thermopower and Hall coefficient can be explained *qualitatively*.

Fujiwara employed a similar parabolic form for the spectral conductivity with an additional oscillating fine structure (sinusoidal form), which should simulate the *spiky* structure [Fujiwara 93a]: $\widehat{\sigma}(\varepsilon) = 1.5\{(\varepsilon - \mu)^2 + 1\} + sin\{1000/j(\varepsilon - \mu)\}$, where μ is the chemical potential. This model explains *qualitatively* the experimentally observed trends of the thermopower.

Recently, Maciá introduced a state density composed of three parts [Maciá 00a]: i) a free-electron-like form (due to the high content of aluminium) far away from the Fermi energy, ii) a parabolic form around the Fermi energy (simulates the Hume-Rothery pseudogap), and iii) a self-similar *spiky* structure modeled by sums of delta functions at certain energies, see figure (6.13). The spectral conductivity is obtained considering the Einstein relation (3.8) with energy independent diffusivity ($\widehat{D}(\varepsilon) = D_0$). This model was employed successfully to explain the conductivity of i-Al-Cu-Ru samples [Maciá 00a]. For this end, however, the *spiky* structure was chosen far away from the Fermi energy. Moreover, the inverse Matthiessen rule could not be found, as pointed out by Maciá [Maciá 00a].

In the following, we propose a model for the spectral resistivity (conductivity) based on the *ab-initio* results discussed in the previous section. This model explains not only *qualitatively* but also *quantitatively* the conductivity and thermopower. Moreover, studies of the Hall coefficient and the electronic thermal conductivity are also realized.

The Lorentzians model

In chapter 3.2, the importance of Kubo-Greenwood formulas has been discussed to perform *ab-initio* calculations of spectral properties of realistic quasicrystals. However, computational limitations do not allow $\underline{k}$-space calculations of approximants with more than a few 100 atoms per unit cell.

As discussed in chapter 4.3, we search in low order approximants for *significant spectral features* which should be present in the quasicrystal, too (similar structural and chemical local order, see chapter 4.3). In this sense, we can set up a model for the spectral resistivity of the approximant which reasonably reproduces the *ab-initio* results. Then, we hope that this modeled spectral resistivity, suitably scaled, can account for the quasicrystal to certain extent, provided that the model includes significant spectral features. Hence, this model can be applied to explain consistently not only the conductivity but also other electronic transport properties.

The scaling of the approximant based spectral resistivity model will be performed by means of the experimentally determined thermopower which is the most sensitive quantity in view of the spectral conductivity.

We suggest to model the spectral resistivity of the Al-Cu-Fe phases by means of Lorentzians. Each Lorentzian, $(\gamma/\pi)/[(\varepsilon-(\varepsilon_F^{sc}+\delta))^2+\gamma^2]$, is characterized by its height, $1/(\pi\gamma)$, and its position, δ, with reference to the self-consistently calculated Fermi energy, ε_F^{sc}. The model for the i-Al-Cu-Fe approximant (quasicrystal) phase requires two Lorentzians,

$$\widehat{\rho}(\varepsilon) = A\left\{\left[\frac{1}{\pi}\frac{\gamma_1}{(\varepsilon-(\varepsilon_F^{sc}+\delta_1))^2+\gamma_1^2}\right] + \alpha\left[\frac{1}{\pi}\frac{\gamma_2}{(\varepsilon-(\varepsilon_F^{sc}+\delta_2))^2+\gamma_2^2}\right]\right\} \quad , \qquad (6.3)$$

whereas one Lorentzian is sufficient for the amorphous phase ($\alpha = 0$ in equation (6.3)). Note that the spectral resistivity is modeled here instead of the spectral conductivity. The reason of this election is given in the Lorentzians model. In fact, the width of the narrow Lorentzian, $2\gamma_2$, can be directly related via $2\gamma_2\tau \simeq \hbar$ to a life time, τ, of the electron propagation.

Table 6.2: Parameters used to model the spectral resistivity of i-Al-Cu-Fe phases. Code: bulk quasicrystal (BQC), 1/1 approximant (APP), amorphous phase (AMP).

	A	δ_1	γ_1	α	δ_2	γ_2
	$\mu\Omega$cm eV	eV	eV		eV	eV
BQC	1047.00	-0.2	1.35	1.00	0.23	0.040
APP	650.00	-0.2	0.70	0.08	0.23	0.025
AMP	1138.83	-1.0	1.60	0.00	-	-

Table (6.2) presents the fitting parameters for both phases. Figure (6.14) shows the spectral resistivity of the i-Al-Cu-Fe approximant phase obtained from the *ab-initio* LMTO-Kubo formula and the model of the equation (6.3). Note that the peak at 0.2 eV below the self-consistently calculated Fermi energy is not explicitely considered, because, this peak is unstable and disappears on rising Γ (see figure (6.6)).

The spectral conductivity is obtained from $\widehat{\sigma}(\varepsilon) = \widehat{\rho}^{-1}(\varepsilon)$. Thus, the Lorentzians simulate two pseudogaps in the spectral conductivity: a wide Hume-Rothery pseudogap and a narrow pseudogap. In the following, we will show that the *anomalous*

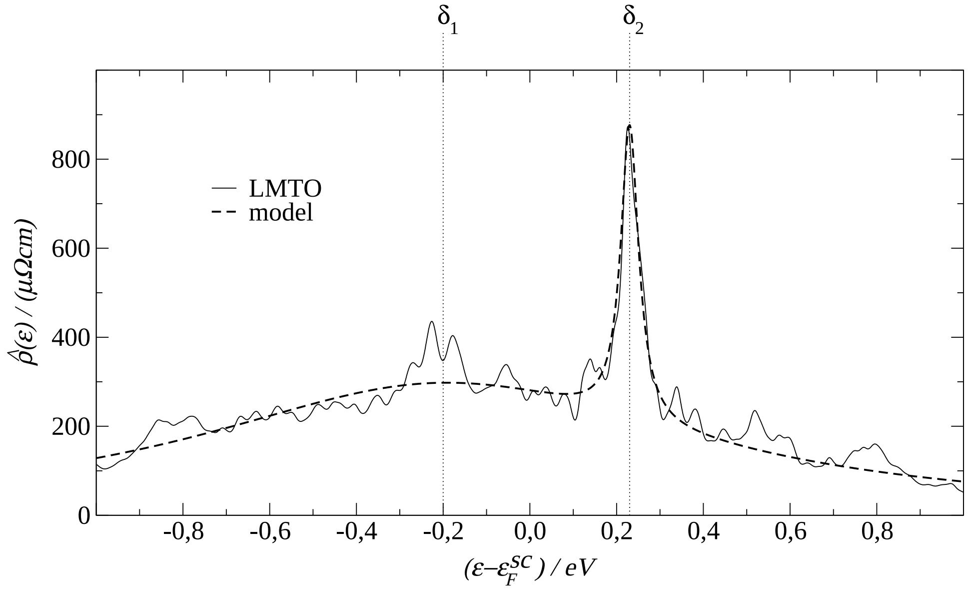

Figure 6.14: i-Al-Cu-Fe approximant, comparison of the *ab-initio* LMTO-Kubo (solid) and the modeled (dashes) spectral resistivity.

transport properties of the approximant (quasicrystal) can be explained considering this simple model for the spectral resistivity. For this purpose, we employ trial positions of the Fermi energy (e.g. A, B in figure (6.12)). The bulk i-Al-Cu-Fe quasicrystal will be studied in the next section. Comparisons with experiments prove the model successful.

Conductivity and inverse Matthiessen rule

The electronic transport behavior of quasicrystals differs clearly from that of metals: very low conductivities, strong composition and temperature dependence, and an inverse Matthiessen rule are the most prominent properties, see chapter 3. In the following, we will demonstrate that these properties can be explained when the Fermi energy lies around the narrow Lorentzian peak of the spectral resistivity, figure (6.14).

The temperature dependence of the conductivity is obtained from equation (A.11) together with (A.8), (A.9), and (A.10), and replacing the corresponding spectral resistivity (conductivity).

The temperature dependent conductivities of three Al-Cu-Fe phases are presented in figure (6.15). Evidently, the crystalline (non-approximant) and the approximant phases have opposite conductivity temperature coefficients. The amorphous model resembles rather the approximant phase, however, the $s_{4.2K} \equiv \sigma(4.2K)/\sigma(300K)$ are clearly different. For the amorphous phase, we find $s_{4.2K} = 0.997$. Experimental results are more indicative $s_{4.2K} = 0.93$ [Biggs 91]. In this respect, the amorphous model employed here is not realistic enough. For the approximant, we obtain $s_{4.2K} = 0.73$ and $s_{4.2K} = 0.57$ for type A, respectively, type B cases.

Moreover, figure (6.15) shows the conductivity increase $\sigma(T) - \sigma(300K)$ versus temperature for five trial Fermi energies within 10 meV environments of type A, type B, Fermi energies. A remarkable stability against small shifts of type B Fermi energies is found. This result is closely related to the inverse Matthiessen rule (3.1). Experimental verification has been reported for quasicrystals and approximants [Mayou 93] and even for transient amorphous phases [Madel 00].

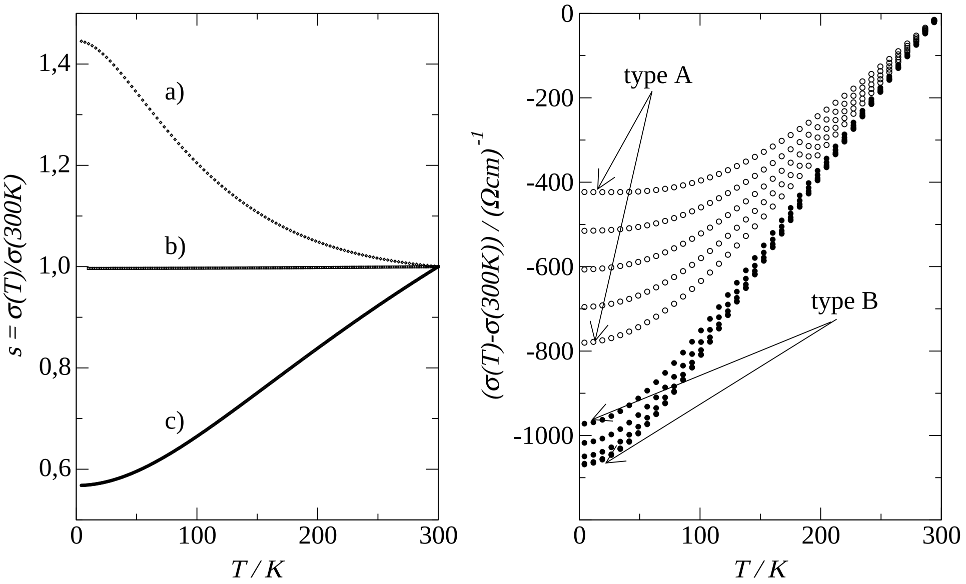

Figure 6.15: Left: temperature dependence of the relative conductivity, $s = \sigma(T)/\sigma(300K)$, for a) crystalline non-approximant phase, b) amorphous phase, and c) approximant phase (Fermi energy type B). Right: i-Al-Cu-Fe approximant, conductivity increase $\sigma(T) - \sigma(300K)$ versus temperature for five trial Fermi energies within 10 meV environments of A ○, B ●.

Applying the Sommerfeld expansion to equation (A.11), one obtains

$$\sigma(T) = \widehat{\sigma}(\varepsilon_F) + \frac{\pi^2}{6}(k_B T)\widehat{n}(\varepsilon_F) \cdot (k_B T)\left[\frac{d}{d\varepsilon}\left(\widehat{n}^{-1}\frac{d\widehat{\sigma}}{d\varepsilon}\right)\right]\Bigg|_{\varepsilon=\varepsilon_F} \quad . \qquad (6.4)$$

It is worth noting that this equation is valid in the low temperature regime (e.g. below ∼150 K for type B Fermi energies). The curves of figure (6.15) are obtained from the exact form, equation (A.11).

Equation (6.4) depends on two properties on the thermal energy scale: i) $(k_B T)\widehat{n}(\varepsilon_F)$ is the number of thermally accessible electron states close to the Fermi energy and ii) $(k_B T)(d\Delta_{qm}\widehat{\sigma}(\varepsilon)/d\varepsilon)_{\varepsilon_F}$ is the variation of $\Delta_{qm}\widehat{\sigma}(\varepsilon) \equiv \widehat{n}^{-1}(\varepsilon)d\widehat{\sigma}(\varepsilon)/d\varepsilon$ which describes the change of the spectral conductivity on the quantum mechanical energy scale ($\widehat{n}^{-1}(\varepsilon)$ level spacing). $\Delta_{qm}\widehat{\sigma}(\varepsilon)$ has a zero at the minimum of $\widehat{\sigma}(\varepsilon)$, and a point of inflection, too. The slopes of $\Delta_{qm}\widehat{\sigma}(\varepsilon)$ are positive for A, B type Fermi energies, which gives rise to positive conductivity temperature coefficients (figure (6.15)). The inverse Matthiessen rule, however, requires the slope of $\Delta_{qm}\widehat{\sigma}(\varepsilon)$ to be constant which is approximately fulfilled for B-type and slightly different Fermi energies which are close to the inflection point (c.f. figures (6.12) and (6.15)).

In other words, the inverse Matthiessen rule (3.1) is fulfilled when ε_F lies close to the spectral conductivity minimum.

Thermoelectric power and Hall coefficient

Small shifts of the Fermi energy may cause the thermopower to switch between large positive and large negative values. This has been proved experimentally for i-Al-Cu-Fe [Pierce 93a, Roth 99]. In the following, we will show that the spectral resistivity model behaves just like. Similarly, the correlations between the signs of the thermopower and the Hall coefficient, observed experimentally [Poon 92], are discussed.

The temperature dependence of the thermopower is obtained from equation (A.12), whereas the Hall coefficient is obtained from equation (A.15) and the *ansatz* (6.2).

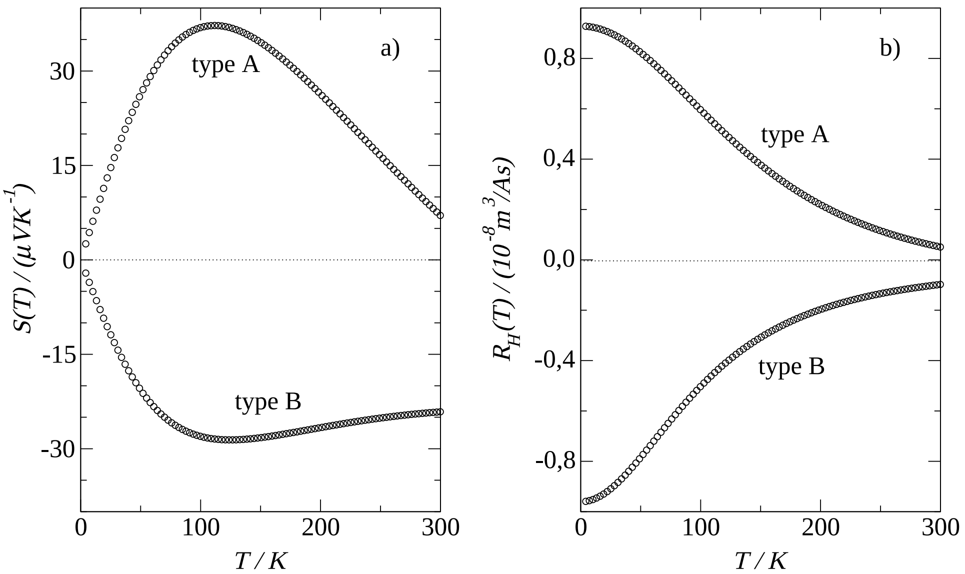

Figure 6.16: i-Al-Cu-Fe approximant, a) thermopower, and b) Hall coefficient, calculated using $Q = 6 \times 10^{-5} Am^2$, for two trial values of the Fermi energy (e.g. A, B). One can also see the correlation of the signs of both, $S(T)$ and $R_H(T)$, over the whole temperature range.

Figure (6.16) shows the thermopower and Hall coefficient for the i-Al-Cu-Fe approximant phase. Drastically different thermopower and Hall coefficient curves belong to the trial Fermi energies A and B, as expected experimentally [Pierce 93a, Roth 99]. Note that the energy difference of the two trial Fermi energies is about 30 meV, which should correspond to small concentration changes.

On the other hand, it has been observed experimentally that the signs of the thermopower and the Hall coefficient are correlated up to room temperature [Poon 92]. This correlation is established in the assumption for $\widehat{\sigma}_H(\varepsilon)$ based on (6.2). To prove this, suppose that the chemical potential $\mu(T)$, that appears in the calculation of the transport coefficients, is confined to the range of the narrow Lorentzian resistivity peak. Thus, equation (6.3) can be approximated to $\widehat{\sigma}(\varepsilon) = \widehat{\rho}^{-1}(\varepsilon) \approx \{\pi/(A\alpha\gamma_2)\}\{(\varepsilon - (\varepsilon_F^{sc} + \delta_2))^2 + \gamma_2^2\}$. Hence, the integrals in $\sigma(T)$, equation (A.11), $S(T)$, equation (A.12), and $R_H(T)$, equation (A.15), can be performed employing only this parabolic form of the spectral conductivity (narrow Lorentzian in the spectral resistivity). After some algebra, we obtain

$$\frac{S(T)/T}{R_H(T)\sigma(T)} = \frac{\pi^2}{3}\frac{k_B^2}{|e|}\frac{1}{Q} \quad . \tag{6.5}$$

The low-temperature limit of equation (6.5) is just the Mott formula [Mott 36],

$$S^{Mott}(T) = -\frac{\pi^2}{3}\frac{k_B^2}{|e|}\left[\frac{d\widehat{\sigma}/d\varepsilon}{\widehat{\sigma}}\right]\Bigg|_{\varepsilon=\varepsilon_F} T \quad . \tag{6.6}$$

Two conclusions can be drawn from equation (6.5): i) the signs of $S(T)$ and $R_H(T)$ are correlated in a wide temperature range (c.f. figure (6.16)), and ii) if sufficiently reliable data at low temperatures are available the parameter Q, equation (6.2), can be estimated.

Electronic thermal conductivity and Lorenz number

Experiments with quasicrystalline samples [Perrot 95] indicate that the electronic contribution amounts less than 5% of the total thermal conductivity, provided that the Wiedemann-Franz law holds for quasicrystals. For the i-Al-Cu-Fe approximant phase, at 10 K, we obtain the electronic thermal conductivity less than 10 % of the experimental total thermal conductivity at this temperature. The electronic thermal conductivity increases rapidly with the temperature and is nearly independent of the chosen Fermi energy (c.f. figure (6.17)).

At 300 K, the total thermal conductivity is dominated by the electronic contribution. The experimental results are ~1.3 W/m/K for the i-Al-Cu-Fe quasicrystal [Perrot 95] and ~4 W/m/K for the $Al_{13}Fe_4$ approximant phase [Perrot 95]. We find ~2.5 W/m/K for the electronic contribution of the i-Al-Cu-Fe approximant phase.

On the other hand, one can doubt about temperature-independent Lorenz numbers. Figure (6.17) shows $L(T)/L_0$, equation (A.14), as obtained with the two-Lorentzians model of the spectral resistivity for the i-Al-Cu-Fe approximant phase ($L_0 = (\pi^2/3)(k_B^2/e^2)$ is the Wiedemann-Franz Lorenz number). At low temperatures, the Lorenz number depends strongly on both the temperature and the chosen Fermi energy. In the limit $T \to 0$, the Lorenz number goes to the Wiedemann-Franz

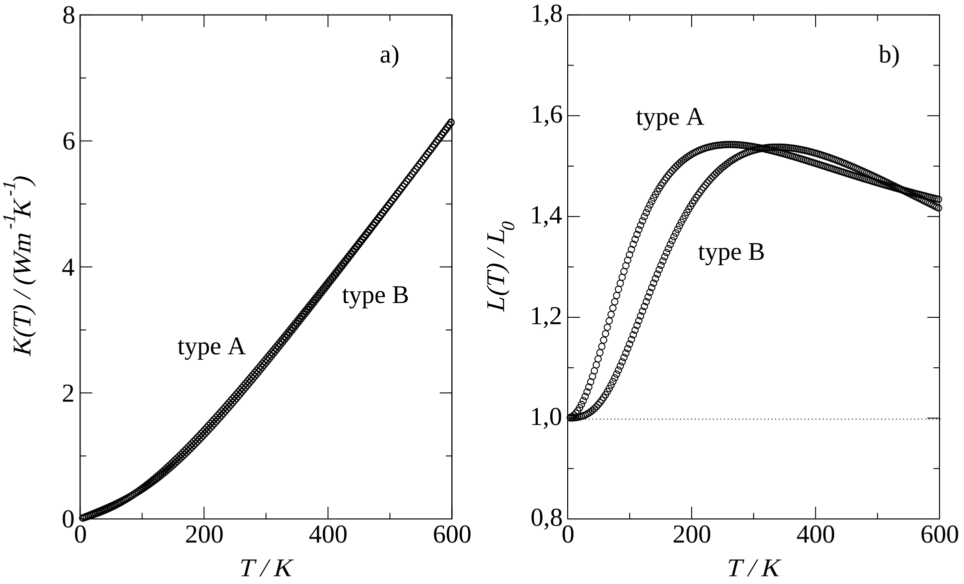

Figure 6.17: i-Al-Cu-Fe approximant, a) electronic thermal conductivity, and b) Lorenz number, for two trial values of the Fermi energy (e.g. A, B). The electronic thermal conductivity is not sensitive to the chosen Fermi energy. The Lorenz number depends strongly on the temperature. $L_0 = (\pi^2/3)(k_B^2/e^2)$ is the Wiedemann-Franz Lorenz number.

Lorenz number as obtained employing the Sommerfeld expansion of equation (A.14) for low temperatures,

$$L(T) = L_0 \left[1 - \frac{\pi^2}{15} \left(5 \left(\frac{\widehat{\sigma}'_F}{\widehat{\sigma}_F} \right)^2 - 8 \frac{\widehat{\sigma}''_F}{\widehat{\sigma}_F} \right) (k_B T)^2 \right] \quad , \tag{6.7}$$

where $\widehat{\sigma}'_F$, and $\widehat{\sigma}''_F$, are the first and second energy derivative of the spectral conductivity evaluated at the Fermi energy.

6.3 The i-Al-Cu-Fe bulk quasicrystal

In this section we will show that the relevant spectral fine structure, for the i-Al-Cu-Fe phase, is the narrow peak (pseudogap) of the spectral resistivity (conductivity), see figure (6.14) and the discussion of chapter 4.3. Thus, in the following, we intend to obtain the parameters for the Lorentzians spectral resistivity model (6.3) which fits the corresponding experimental [Pierce 93b] conductivity and thermopower of the i-$Al_{62.5}Cu_{25}Fe_{12.5}$ bulk quasicrystal.

The fit procedure

We proceed as follows:

1) The Lorentzians are centered at just the same energies as in the i-Al-Cu-Fe approximant (table (6.2)). Thus, the parameters δ_1, δ_2 are fixed.

2) In the definition of ξ (c.f. equation (A.10)) one can replace $\widehat{n}(\varepsilon)$ by $\widehat{\sigma}(\varepsilon)$, provided that spectral variation of the diffusivity is neglected. Then, we can relate ξ to the thermopower using the Mott formula (6.6) in the following way $\xi = -0.5|e|(S^{Mott}(T)/T)$. Using experiments [Pierce 93b] at low temperatures one obtains $\xi = 0.12 \times 10^{-6} eV/K^2$. This is used as our initial value.

3) A and γ_1 belong to the wide Lorentzian and their influence become important at high temperatures. Then, we chose the values of the approximant phase (table (6.2)) as the initial ones.

4) The parameters α and γ_2 are the critical ones: α and γ_2 are changed in the range 0.1-10.0, respectively, 10-100 meV, in small steps.

5) Thus, ε_F is fixed employing the condition that the spectral resistivity (6.3) provides approximately the experimental resistivity at 4 K, $\widehat{\rho}(\varepsilon_F) \approx \rho_{4K}^{exp}$ (the error considered is less than 5%).

6) For a given set of parameters, one can obtain the conductivity (A.11), and thermopower (A.12) for each temperature.

7) Hence, the final set of parameters are those that provide the minimal χ^2 statistics ($(\delta S)^2 = 1$),

$$\chi^2 = \sum_{T}^{N_{data}} \frac{\{S^{exp}(T) - S^{fit}(T; \xi, A, \gamma_1, \alpha, \gamma_2)\}^2}{(\delta S)^2} \quad , \tag{6.8}$$

where S^{exp} is the experimental thermopower [Pierce 93b] and S^{fit} is the calculated thermopower, equation (A.12). The temperature range considered goes from ~4 K up to 300 K.

Note that for the calculation of χ^2, equation (6.8), we employ the thermopower instead of the conductivity because of the sensitivity on the spectral resistivity of the first one. This provides more accuracy in the results.

We obtain $A = 1047\,\mu\Omega cm$, $\gamma_1 = 1.35$ eV, $\alpha = 1.0$, and $\gamma_2 = 40$ meV (c.f. table (6.2)). The Fermi energy is found 10 meV above the centre of the narrow Lorentzian, and $\xi = 0.1 \times 10^{-6} eV/K^2$, which is close to the initial value of $\xi = 0.12 \times 10^{-6} eV/K^2$. As pointed out in 3), the influence of the parameters A and γ_1 become important at high temperatures. The present basis of experimental data (thermopower up to 300 K [Pierce 93b]) is not yet wide enough to provide precise results for A, γ_1. Thermopowers beyond 300 K are required.

Figure (6.18) shows the results of our model in comparison with experiments. For the conductivity the agreement is good up to 600 K. The inset shows the thermopower up to 300 K where experimental results are available. Extrapolating this model to high temperatures we obtain a zero thermopower at ~326 K and $S(600K) \approx 41.8\mu V/K$, which depends on the exact values of A and γ_1, as discussed above. Moreover, in difference to the conductivity, the thermopower is strongly sensitive to ξ.

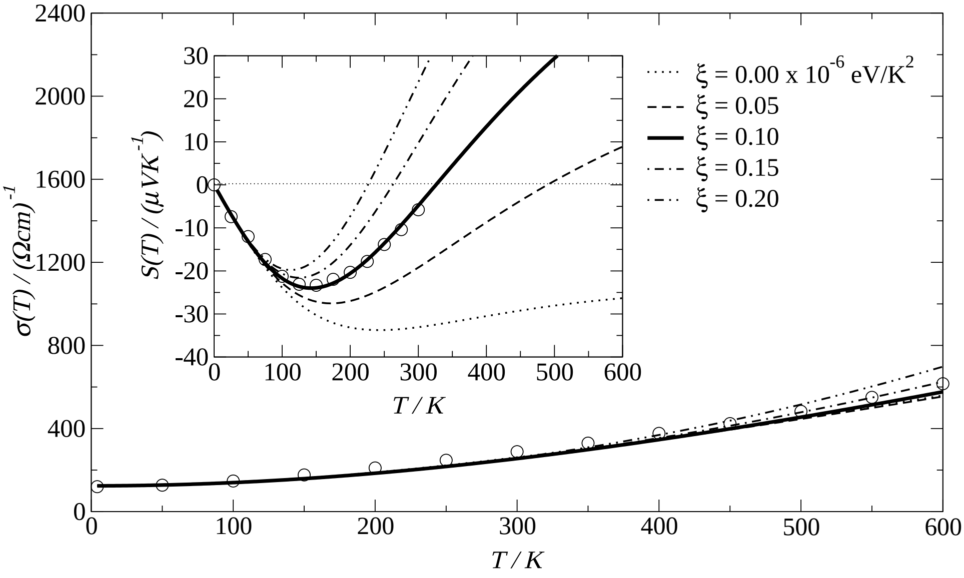

Figure 6.18: i-Al-Cu-Fe bulk quasicrystal, temperature dependence of the conductivity and thermopower (inset) employing the resistivity Lorentzians model with different ξ values (lines) and from a few selected experimental points ($\circ$) after [Pierce 93b].

Other results of the employed model are: i) $\sigma_{0K} \approx 123.8(\Omega cm)^{-1}$ and $s_{0K} = 0.485$ (see figure (6.18)), ii) the Hall coefficient behaves like the thermopower, i.e. we find transitions from negative to positive values around 322 K (see figure (6.19)), iii) with $Q = 2 \times 10^{-5} Am^2$ we obtain the Hall coefficient comparable with experiments [Lindqvist 93] ($R_H(4.2K) \approx -1.85 \times 10^{-8} m^3/A/s$), iv) at 300 K, the electronic contribution to the thermal conductivity is ~0.46 W/m/K, and v) $L(300K)/L_0 = 2.42$ (see figure (6.19)).

Discussion

The fact that γ_2 is larger than the obtained for the approximant becomes clear if we take into account the results of the previous sections. Rising temperature must reduce the fine structure (see figure (6.7)). The 40 meV are thus to be interpreted as the average width up to 300 K. Recently, Madel [Madel 00] has applied our model to experimental results of thin film quasicrystalline and transient amorphous Al-Cu-Fe phases. As an indication of minor structural perfection, the low-temperature resistivity, ρ_{4K}, was less than obtained for the bulk quasicrystal [Pierce 93b], c.f. table (6.3). The corresponding Lorentzian resistivity models should reveal that the spectral features which are specific for the quasicrystal grow up towards the bulk quasicrystal. We take $x = \alpha\gamma_1/\gamma_2$ (the relative height of the narrow Lorentzian) as a criterion. Table (6.3) shows the expected behavior: increasing ρ_{4K} indicates that the spectral feature of the quasicrystalline phase gets more pronounced as x grows.

Fujiwara *et al.* [Fujiwara 96, Roche 98] deal with the temperature dependence of the conductivity employing both the anomalous Drude conductivity (3.9), and

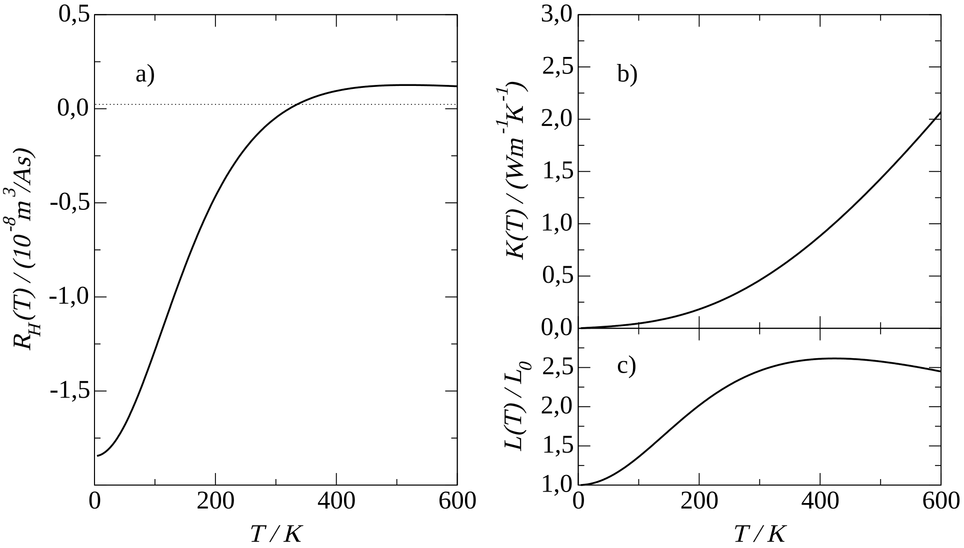

Figure 6.19: i-Al-Cu-Fe bulk quasicrystal, temperature dependence of a) the Hall coefficient with $Q = 2 \times 10^{-5} Am^2$, b) the electronic thermal conductivity, and c) the Lorenz number.

the Bloch-Grüneisen law (describes the electron-phonon coupling), they show that $\sigma(T) \propto T^{1.25}$. In fact, a fit of the i-Al-Cu-Fe bulk quasicrystal provides $\sigma(T) = 92.52 + 0.1667\,T^{1.25}$, which is comparable with the conductivity (experiment and model) shown in figure (6.18). However, as discussed in chapter 3.2, the validity of the Bloch-Grüneisen law requires of a more convincing justification to be applied in quasicrystals.

Table 6.3: Criterion to classify the different Al-Cu-Fe phases. Code: transient amorphous phase annealed at 600 K (TAM), approximant phase with ε_F type A (APP1), approximant phase with ε_F type B (APP2), thin film quasicrystal (TFQC), and bulk quasicrystal (BQC). See text for discussions (the parameters of TAM and TFQC used to calculate x have been taken from Reference [Madel 00].

	TAM	APP1	APP2	TFQC	BQC
x	0.945	2.24	2.24	7.76	33.75
ρ_{4K} ($\mu\Omega cm$)	455	623	782	2333	8078

Chapter 7

The Al-Pd-Re system

The electronic properties of the i-Al-Pd-Re quasicrystal were discussed in chapter 3.3. As yet, they are the most resistive quasicrystals due to strong electronic scattering and interference. Moreover, the question about the existence of insulating samples and the transport mechanism remain open.

In the following, we will study the spectral properties of different approximant models of i-Al-Pd-Re. In the same way as demonstrated for i-Al-Cu-Fe (see chapter 6), the temperature dependence of the conductivity is modeled. The results are in agreement with experiments.

7.1 Approximant models and spectral properties

As yet, crystallographic structure data and the proper chemical decoration of the low order approximants are not completely determined. Thus, i-Al-Pd-Mn approximant models have been employed for i-Al-Pd-Re, both with similar diffraction patterns. In fact, Krajčí and Hafner calculated the spectral conductivity of hypothetical approximant models of i-Al-Pd-Re (from i-Al-Pd-Mn) employing the Bloch-Boltzmann and Kubo-Greenwood formula [Krajčí 99, Krajčí 01]. They found, in the 1/1 approximant model, a semiconducting gap (width ∼150 meV) that is very sensitive on the details of the atomic structure and chemical order. However, this real gap disappears for high order approximants. Moreover, participation ratios indicate the presence of critical electronic states around the Fermi energy.

As discussed in chapter 3.2, the employment of Kubo-Greenwood formulas is important to describe the electronic properties of high resistive systems, such as the i-Al-Pd-Re quasicrystal. Moreover, the importance of realistic models together with the right chemical decoration was also discussed in chapter 6. In the following we will calculate spectral and temperature dependent properties of *test structure models* of i-Al-Pd-Re 1/1 approximants.

For this purpose, we employ the structure model of the 1/1 approximant of i-Al-Pd-Mn [Sugiyama 98a] and i-Al-Cu-Fe [Cockayne 93] (c.f. table (6.1)). Two models will be treated in the following. The first one is obtained from the i-Al-Pd-Mn 1/1 approximant replacing Mn atoms by Re atoms. This provides the model for the i-$Al_{73.2}Pd_{12.2}Re_{14.6}$ approximant. Note that this hypothetical 1/1 approximant is not the same as used by Krajčí and Hafner [Krajčí 99, Krajčí 01]. The second one is obtained from the i-Al-Cu-Fe approximant replacing Fe(1), Fe(2), and Cu(1) by Re atoms, and Cu(2), Al(6), and Cu(4) by Pd atoms (see table (6.1)). Additionally, the lattice constant was changed from 12.3Å to 12.45Å. This provides our model for the i-$Al_{68.8}Pd_{15.6}Re_{15.6}$ approximant.

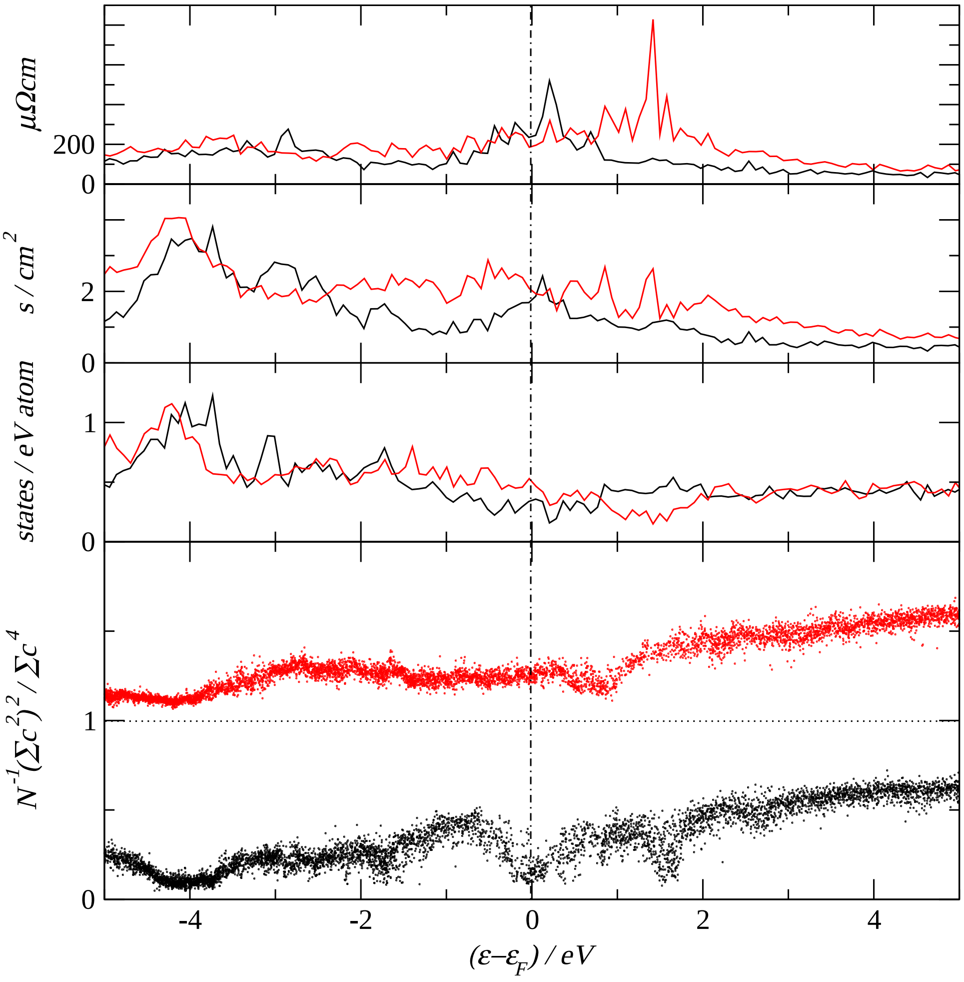

Figure 7.1: Spectral properties of two test structures of the hypothetical 1/1 approximant of the i-Al-Pd-Re: after the i-Al-Pd-Mn (black) and after the i-Al-Cu-Fe (red), see text for details. From top to bottom: spectral resistivity, inverse of the electronic diffusivity, state density, and participation ratios (each curve has been shifted upwards by 1). LMTO-ASA supercell calculations with $\underline{K}^{(3)}$, and Lorentzian half-width of $\Gamma = 20$ meV.

Figure (7.1) shows the spectral properties of these two hypothetical 1/1 approximants. In concordance with the analysis of chapter 6 and the results of Krajčí and Hafner [Krajčí 99], the spectral fine structure depends strongly on both, structure and chemical decoration[1]. Participation ratios depend strongly on the energy, especially close to the Fermi energy. In many cases the spectral resistivity peaks are related with rapidly varying characters of the electronic states.

It seems that this strong sensitivity to the chemical environment is a property of approximants/quasicrystals (specially for i-Al-Pd-Re). For comparison, decoration changes in the crystalline Hume-Rothery $\mathrm{Al}_{12}\mathrm{Re}$ phase (crystallographic data has been taken from [Villars 91]) show nearly the same spectral properties. Indeed, figure (7.2) shows similar state densities for the $\mathrm{Al}_{12}\mathrm{X}$ phase, with $\mathrm{X} = \mathrm{Re}, \mathrm{Cr}, \mathrm{Mn}, \mathrm{Fe}$: the Fermi energy moves in a (nearly) rigid state density pseudogap on changing the transition metal. Moreover, Re atoms behave isoelectronic with Mn atoms. This is not the case of the approximant models presented here (c.f. figure (7.1)).

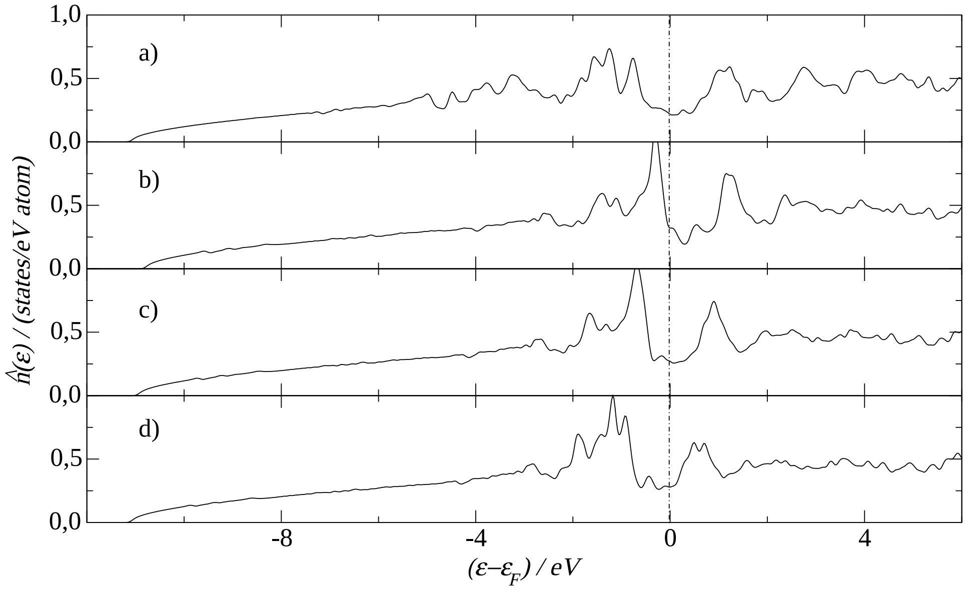

Figure 7.2: Density of states of the a) $\mathrm{Al}_{12}\mathrm{Re}$ Hume-Rothery crystalline system. Re atoms are changed by b) Cr, c) Mn, and d) Fe atoms in $\mathrm{Al}_{12}\mathrm{Re}$. LMTO-ASA supercell calculations with $\underline{K}^{(5)}$, and Gaussian half-width of $\Gamma = 15$ meV.

In summary, in view of the strong structural and chemical dependences of the spectral properties, additional studies of i-Al-Pd-Re approximants are feasible only when sufficient crystallographic data exist. At the close of the present work, Tamura and Takeuchi showed [Tamura 01] that the cubic $\mathrm{Al}_{43}\mathrm{Re}_{10}\mathrm{Si}_4$ phase, with lattice constant $a = 12.85\text{Å}$, is the 1/1 approximant of the i-Al-Pd-Re quasicrystal. This approximant is structurally similar to the 1/1 approximant of the i-Al-Mn-Si quasicrystal, the α-Al-Mn-Si phase.

---

[1] Spectral properties of other three decoration models with the same structures, i-Al-Pd-Mn or i-Al-Cu-Fe, confirm this result. Moreover, changes of the lattice constant drives the Fermi energy. Figure (7.1) shows only the most relevant results.

7.2 Modeling the conductivity

Some prominent peaks in the spectral resistivity of i-Al-Pd-Re approximants indicate that the Lorentzians resistivity model, equation (6.3), could be applied (c.f. figure (7.1)). On the other hand, experiments [Haberkern 00a] show a conductivity pseudogap after changing the Al content of i-Al-Pd-Re samples. The Hall coefficient changes its sign just around of this conductivity minimum. Comparisons of these results with those found for i-Al-Cu-Fe (c.f. figure (6.12)) indicate that the Lorentzians resistivity model can be applied in the same way as in the i-Al-Cu-Fe phase (see chapter 6).

For i-Al-Pd-Re we model directly the transport properties of the quasicrystal because, as yet, there is not feasible models for low order approximants (see the discussion of the previous section). In this sense, we proceed as follow: i) we take the Lorentzians resistivity model of the i-Al-Cu-Fe phase, equation (6.3), ii) the parameters A, δ_1, δ_2, and γ_1 are not critical, hence, they are fixed at the same values employed for the i-Al-Cu-Fe bulk quasicrystal (c.f. table (6.2)), iii) the other parameters, γ_2, ε_F, and ξ are chosen as to reproduce reasonably the experimental conductivity [Haberkern 00a, Haberkern 00b] up to 900 K. In difference to the fit procedure used for i-Al-Cu-Fe bulk quasicrystal, in this case the χ^2 test, equation (6.8), is realized employing the conductivity instead of the thermopower (insufficient experimental data). The parameters are listed in table (7.1).

Table 7.1: Parameters used to model the spectral resistivities. The values $A = 1047\mu\Omega\mathrm{cmeV}$, $\delta_1 = -0.2eV$, $\delta_2 = 0.23eV$, and $\gamma_1 = 1.35eV$ are fixed from the i-Al-Cu-Fe bulk quasicrystal (c.f. table (6.2)). $x = \alpha\gamma_1/\gamma_2$. For the sample with 7.5 at. % Re, ρ_{4K} was obtained after extrapolating the model from $T > 100K$ up to zero Kelvin (see text for details).

composition	α	γ_2 meV	$(\varepsilon_F - \delta_2)$ meV	ξ 10^{-6} eV/K^2	x	ρ_{4K} $\mu\Omega cm$
$Al_{74.6}Pd_{19.3}Re_{6.1}$	0.4043	95.0	5.6	0.10	5.75	1635
$Al_{74.2}Pd_{19.6}Re_{6.2}$	0.4795	75.0	34.4	0.05	8.63	1977
$Al_{73.8}Pd_{19.9}Re_{6.3}$	0.5484	70.0	-20.0	0.00	10.58	2742
$Al_{72.2}Pd_{21.1}Re_{6.7}$	1.9628	25.0	-20.0	0.00	105.99	24286
$Al_{72.3}Pd_{20.2}Re_{7.5}$	3.8642	42.1	-22.0	0.10	123.91	25500

Figure (7.3) shows the results of the modeled conductivity in comparison with experiments. The modeled temperature and composition dependence of the experimental conductivity is in good agreement with experiments. As discussed in chapter 6.3, sufficiently reliable experimental data of the thermopower can provide more refined results. That means, the parameters presented in table (7.1) can change to obtain consistent results for both transport coefficients (conductivity and thermopower): for example, the difference $(\varepsilon_F - \varepsilon_F^{sc}) - (\delta_2 - \varepsilon_F^{sc})$ in table (7.1) can change its sign depending on the thermopower sign.

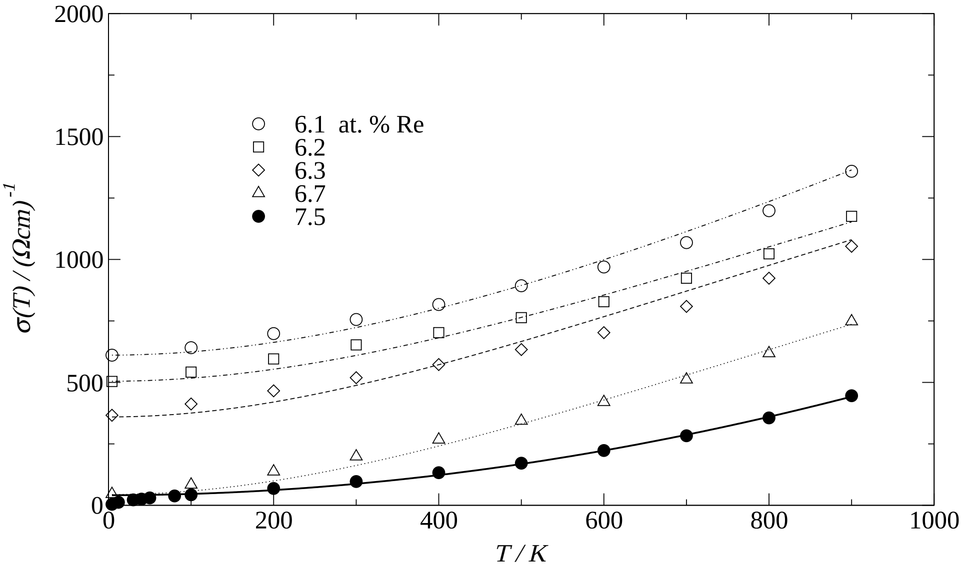

Figure 7.3: Temperature dependence of the conductivity employing the resistivity Lorentzians model (lines) and from a few selected experimental points (after [Haberkern 00a]) of i-Al-Pd-Re thin-film quasicrystals with different at. % Re content.

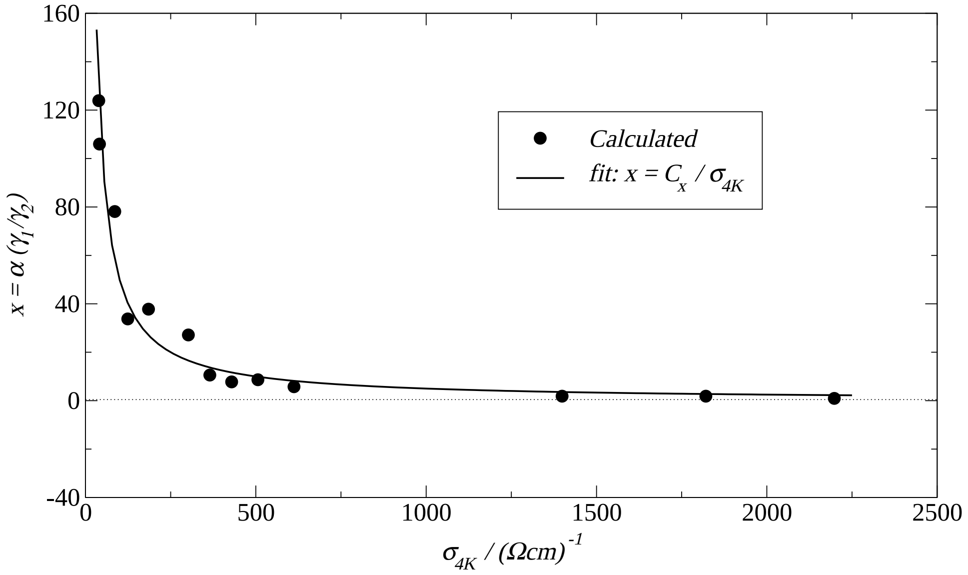

Figure 7.4: Dependence of the parameter $x = \alpha\gamma_1/\gamma_2$ (characterize the resistivity Lorentzians model) with the conductivity at 4 K. The calculated values (circles) can be fitted with $x = C_x/\sigma_{4K}$ (solid line), where $C_x = 5000\ (\Omega cm)^{-1}$.

Below 100 K, the conductivity of the more resistive sample (7.5 at. % Re) can not be reproduced with the model. In fact, assuring a good agreement for $T > 100$ K, the Lorentzians model of the spectral resistivity provides always a finite conductivity at zero Kelvin. From experiments [Haberkern 00a], there are strong indications that this sample becomes insulator towards zero Kelvin.

Hence, if this sample is an insulator, then the spectral conductivity must have a real gap around the Fermi energy. To test this ansatz, we fit the experiments below 100 K, to the Mott spectral conductivity, equation (3.11), which provides $\sigma(T) = \sigma_{min} exp\{-(\varepsilon_c - \mu)/k_B T\}$. In fact, for temperatures below 100 K, this *gap*-model for the spectral conductivity fits the experiments with $\sigma_{min} = 50(\Omega cm)^{-1}$, and $\varepsilon_c - \mu = 1.723$ meV.

Really, this agreement can not be taken for proof of thermally activated transport. There are also indications for variable-range hopping transport (3.13) in i-Al-Pd-Re [Delahaye 98]. However, our results support the idea of a temperature dependent action of certain spectral conductivity features.

In this sense, it is expected that the Lorentzians spectral resistivity model alone can not be applied (at low temperatures) to insulating samples. Quasicrystals with such very low (or zero) conductivities require a modified spectral resistivity (conductivity) model, as dicussed above. This is shown in figure (7.4), where the parameter $x = \alpha\gamma_1/\gamma_2$ (see chapter 6.3) is plotted versus the conductivity at 4 K, σ_{4K}. The values of x are taken from all fitted materials shown in the present work (see tables (6.3), (7.1), and (9.1)). One can see that x grows rapidly when σ_{4K} decreases: at zero conductivity (insulating samples), x diverges.

Chapter 8

Optical conductivity

This chapter deals with the influence of spectral fine structures on the optical properties of approximants/quasicrystals. For this purpose, we study the optical conductivity, $\tilde{\sigma}(\omega)$, which is a complex quantity. Its real part, $\sigma_1(\omega)$, is due to electrons in the valence band, whereas the imaginary part is provided by core polarization[1]. In the following, we will study only the real part of the complex optical conductivity.

It is known that two main processes contribute to the optical conductivity. Namely, intraband and interband transitions. Depending on the system, one of these processes may dominate. For instance, in metals the optical conductivity can be described as given by intraband processes only. It is determined by the frequency-dependent (or AC) Drude conductivity (see for example [Ashcroft 76]),

$$\tilde{\sigma}(\omega) = \frac{\sigma_0}{1 - i\omega\tau} \quad , \tag{8.1}$$

where σ_0 is the DC Drude conductivity given at zero frequency, and τ is a relaxation time. Thus, at very low frequencies, the optical conductivity (real part) shows the so-called Drude-peak (half-width $1/\tau$).

However, the optical conductivity of quasicrystals/approximants is far from the metallic behavior. The more relevant results found experimentally are [Homes 91, Bianchi 97, Basov 94a, Basov 94b]: i) At very low frequencies, both the absence of a Drude peak and a linear increase with frequency are observed. This should be due to the small number of carriers (low density of states at the Fermi energy). ii) For i-Al-Cu-Fe, a well defined peak at very low frequencies, $\hbar\omega \simeq$32 meV, may be explained by interaction with phonons, or by interband transitions in a *spiky* state density. iii) At high frequencies, $\hbar\omega \simeq$1-3 eV, the optical conductivity reaches its maximum. Beyond this maximum its behavior is typical of most metals.

Different models were proposed to explain the *anomalous* behavior of the optical conductivity of quasicrystals/approximants. There is no accordance about the mechanism that dominates in the optical conductivity. Burkov *et al.* [Burkov 92] presented

---

[1] The imaginary part of the optical conductivity is related with the real part of the dielectric constant.

a model for the optical conductivity where interband transitions should dominate. In fact, within the nearly free-electron model, and in terms of the *large number* of reciprocal lattice vectors $\underline{K}$ (multiplicity 42 for icosahedral quasicrystals) that take part in the Hume-Rothery mechanism of stability, $K \approx 2k_F$, they show that

$$\sigma_1(\omega) = \sigma_G \frac{\omega^2\tau^2}{(1+\omega^2\tau^2)^2} \quad , \tag{8.2}$$

where σ_G is a constant which depends on the state density in pseudogaps, and τ is a phenomenological relaxation time. Equation (8.2) explains the experiments [Homes 91] after employing pseudogap widths of the order of 0.5 eV and $\tau \simeq 0.5 \times 10^{-15}s$. Numerical calculations for the α-Al-Mn-Si approximant also indicate the interband transitions as the dominant mechanism [Fujiwara 93b].

Explanations of the experimentally observed optical conductivity due only to intraband transitions was given by Smith [Smith 01]. For this purpose, the author generalizes the Drude formula (8.1) based on Poisson statistics for the probability of collisions. Thus, the absence of the Drude-peak is explained due to predominant backscattering.

On the other hand, if the electron propagates subdiffusively the absence of the Drude-peak and the increase of the optical conductivity with frequency (at low values) can be explained, as shown by Mayou [Mayou 00]. In fact, if the electronic wave packets spread with an anomalous diffusion law $L(t) \propto t^\beta$ where $0 < \beta < 1$ ($\beta = 0.5$ means normal diffusivity), then the optical conductivity is given by [Mayou 00],

$$\tilde{\sigma}(\omega) = \sigma_\beta \left(\frac{\tau}{1 - i\omega\tau}\right)^{2\beta-1} \quad , \tag{8.3}$$

where σ_β is a coefficient involving the scaling parameter β, and τ is a time beyond which the propagation becomes diffusive. Equation (8.3) is in close relation with the anomalous Drude conductivity (3.9), discussed in chapter 3.2. Thus, for $\beta = 1$ the simple Drude optical conductivity (8.1) is recovered, whereas for $\beta \leq 0.5$ a plateau or a dip is obtained, which explains *qualitatively* the experiments for low frequencies.

As seen, there is not a conclusive explanation of the *anomalous* behavior of the optical conductivity. In the following, we calculate the optical conductivity of low order approximants, and (for comparison) amorphous phases. A model which explains the optical conductivity of quasicrystals is also presented.

Basic concepts

The real part of the optical conductivity can be obtained from the Kubo-Greenwood formula (see a brief deduction in appendix A.1),

$$\sigma_1(\omega) = \int d\varepsilon \left(-\frac{f(\varepsilon+\hbar\omega,\mu,T) - f(\varepsilon,\mu,T)}{\hbar\omega}\right) \widehat{\sigma}(\varepsilon, \varepsilon+\hbar\omega) \quad , \tag{8.4}$$

where $f(\varepsilon,\mu,T)$ is the Fermi-Dirac distribution function (A.9) and

$$\widehat{\sigma}(\varepsilon,\varepsilon+\hbar\omega)=2\frac{\pi\hbar e^2}{\Omega}\sum_{i,j}|\langle j|v|i\rangle|^2\delta(\varepsilon+\hbar\omega-\varepsilon_j)\delta(\varepsilon-\varepsilon_i) \quad . \tag{8.5}$$

When $\omega \to 0$ the optical conductivity (8.4) goes to the DC conductivity (A.11) at temperature T, as shown in appendix A.1.

However, many authors [Zhao 90, Hobbs 95, Arnold 97] used an explicite form of equation (8.4), where the integration is realized. Hence, the optical conductivity (real part) can be written as

$$\sigma_1(\omega) \;=\; 2\frac{\pi\hbar e^2}{\Omega}\sum_{i,j}|\langle i|v|j\rangle|^2\,\frac{f(\varepsilon_i,\mu,T)-f(\varepsilon_i+\hbar\omega,\mu,T)}{\hbar\omega}\,\delta(\varepsilon_i-\varepsilon_j+\hbar\omega) \quad . \tag{8.6}$$

We will use this equation in the *ab-initio* calculations presented in the next section. The wave function $|i\rangle$, and eigenvalue ε_i are calculated employing the LMTO-ASA supercell method (described in chapter 5), in similar form as realized in [Hobbs 95, Arnold 97]. In practice, the delta function is broadened by Lorentzians (3.7) with half-width Γ, see the discussion of chapter 3.2 for the Kubo-Greenwood conductivity, equation (3.5).

8.1 Ab-initio optical conductivity of low order approximants

The structure models of the low order approximants studied here (Al-Cu-Fe, Al-Cu-Ru, Al-Pd-Mn, and Al-Mn-Si) are described in appendix D.

The optical conductivity of the i-Al-Cu-Fe approximant is presented in figure (8.1). Two Fermi energies are employed: the self-consistently calculated, ε_F^{sc}, and the type B which lies around the narrow conductivity pseudogap, see figure (6.12). As expected, when the frequency goes to zero, the optical conductivity goes to the DC conductivity. At low frequencies, the optical conductivity decreases when the state density decrease: $\widehat{n}(\varepsilon_F^{sc}) = 0.47\ (eV)^{-1}$, and $\widehat{n}(B) = 0.12\ (eV)^{-1}$. This is more indicative after comparing it with the amorphous phase: $\widehat{n}(\varepsilon_F^{sc}) = 0.55\ (eV)^{-1}$, which is ∼4.6 times higher than the state density of the approximant phase (Fermi energy type B). Fermi energy shifts causes no considerable differences for frequencies $\hbar\omega > 500$ meV.

An increase of the optical conductivity with the frequency is also observed. Experimentally [Homes 91], a maximum is found at $\hbar\omega \approx 1.3$ eV in the i-Al-Cu-Fe quasicrystal. For the approximant, we found the maximum at $\hbar\omega \approx 2.3$ eV. Above the optical conductivity maximum, there are not differences between the approximant and amorphous phases: the behavior is similar to most metals. This is expected because spectral fine structure on the state density (respectively, spectral

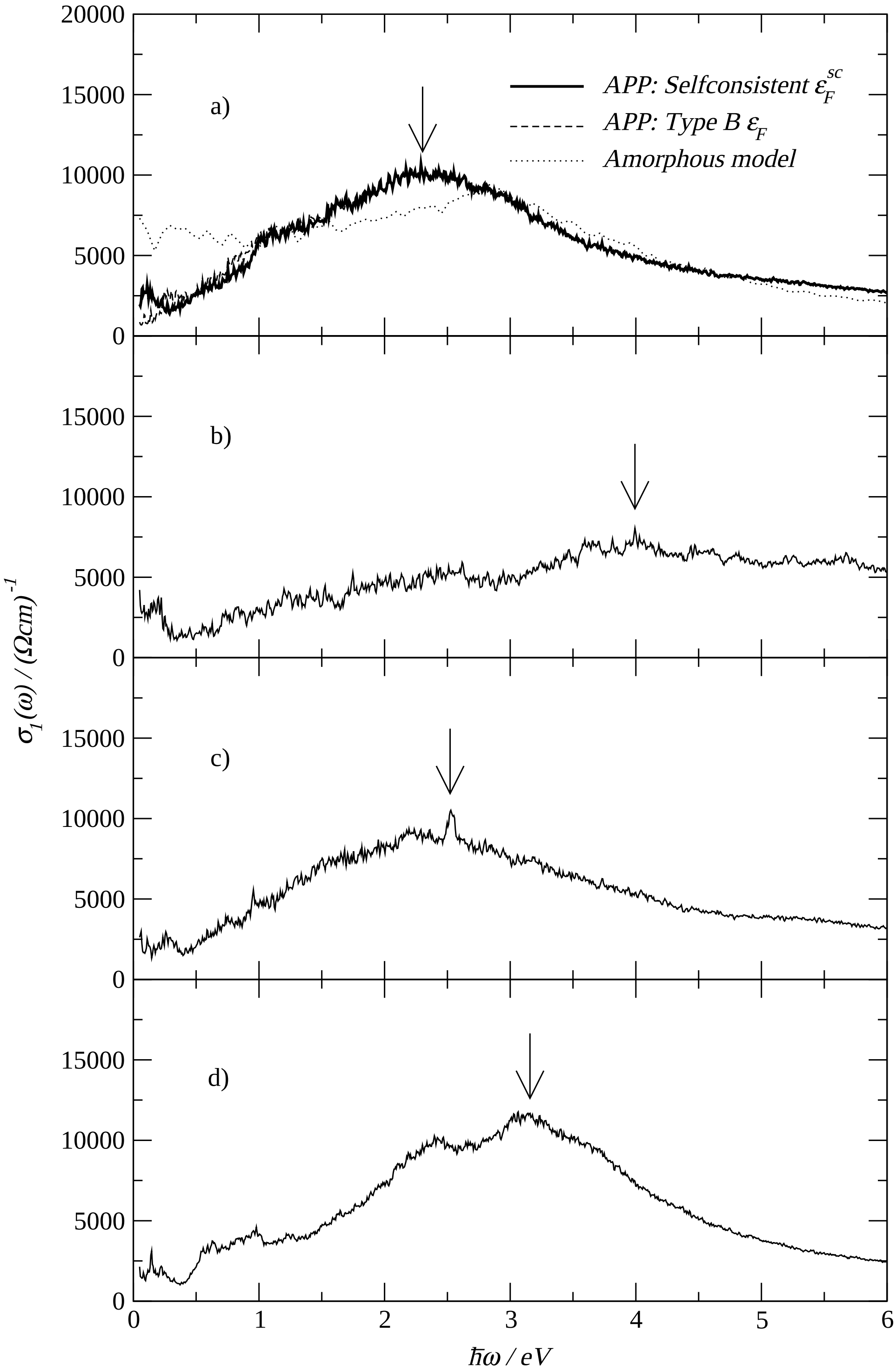

Figure 8.1: Optical conductivity of icosahedral approximants calculated at $T = 0$ K. a) Al-Cu-Fe phases, approximant (APP) and amorphous model, b) Al-Cu-Ru, c) Al-Pd-Mn, and d) α-Al-Mn-(Si). The arrows indicate the frequency at which the optical conductivity becomes maximal. See text for details.

conductivity), present only in approximants/quasicrystals, is important only for low frequencies.

In chapter 6, we have found that the electron propagates sub-diffusively with scaling parameter $\beta = 3/8$ for the i-Al-Cu-Fe approximant (see figure (6.7)). This explains also the increase of the optical conductivity at low frequencies, as shown by Mayou [Mayou 00]. In fact, he shows that for small disorder ($\omega\tau \gg 1$), equation (8.3) reduces to $\sigma_1(\omega) \propto \omega^{1-2\beta}$. In the case of the i-Al-Cu-Fe approximant, that means $\sigma_1(\omega) \propto \omega^{1/4}$ which explains *qualitatively* the increase of the optical conductivity with the frequency.

The optical conductivity of the γ-Al-Cu-Ru, α-Al-Pd-Mn, and α-Al-Mn approximants are also presented in figure (8.1). For very low frequencies, up to 250 meV, the different optical conductivity behaviors indicate different spectral fine structures on the state density (respectively, spectral conductivity). At low frequencies, the optical conductivity increases (nearly) linearly with the frequency. The optical conductivity maximum lie between ∼2-4 eV, depending of the approximant. Beyond these maximums, the behavior is typical of most metals. These results are *qualitatively* in good agreement with experiments in quasicrystals (c.f. figure (8.2), see also [Homes 91, Bianchi 97, Basov 94a, Basov 94b]). The *quantitative* differences may be attributed to the structural and/or chemical differences between the approximant and the real quasicrystal. In the next section, we will propose a model for the optical conductivity of quasicrystals which can explain *quantitatively* the experiments.

Based on equation (8.6), a possible explanation of the optical conductivity of quasicrystals/approximants is as follows. At low frequencies, the electron must jump from states of similar energies, that means, the electron travels over large distances. Therefore, spectral fine structures imply that the velocity matrix elements are large and hence the optical conductivity increases (this is the case of quasicrystals). When spectral fine structures are not present or their influence is not remarkable (high frequencies), then the optical conductivity reduces.

8.2 Modeling the optical conductivity of quasicrystals

Two remarkable aspects of the optical conductivity of quasicrystals have been discussed in the previous section: at low frequencies a linear increase, and at high frequencies a typical metallic behavior. This gives rise to relate it to the Lorentzians resistivity model (6.3). In fact, this model has a narrow and a wide Lorentzian. The first one is considered typical of approximants/quasicrystals. The second one is considered of Hume-Rothery origin (phase stability) and thus common with amorphous phases. Hence, the low (high) frequency dependent optical conductivity should be explained by the narrow (wide) Lorentzian. In the following, we will check this idea.

For this purpose, we employ the *ansatz*

$$\widehat{\sigma}(\varepsilon,\varepsilon+\hbar\omega) \approx A_{\sigma_1}\sqrt{\widehat{\sigma}(\varepsilon)\ \widehat{\sigma}(\varepsilon+\hbar\omega)} \tag{8.7}$$

to model the optical conductivity, equation (8.4). The *ansatz* (8.7) is not more than a geometrical average of spectral conductivities at two different energies, ε and $\varepsilon+\hbar\omega$. We believe that this is the most simple approach to $\widehat{\sigma}(\varepsilon,\varepsilon+\hbar\omega)$. In fact, equation (8.7) considers, at least, spectral information at two different energies. Furthermore, the limit $\hbar\omega \to 0$ provides the DC conductivity (apart from a factor A_{σ_1} of order unity). The meaning of A_{σ_1} will be discussed below.

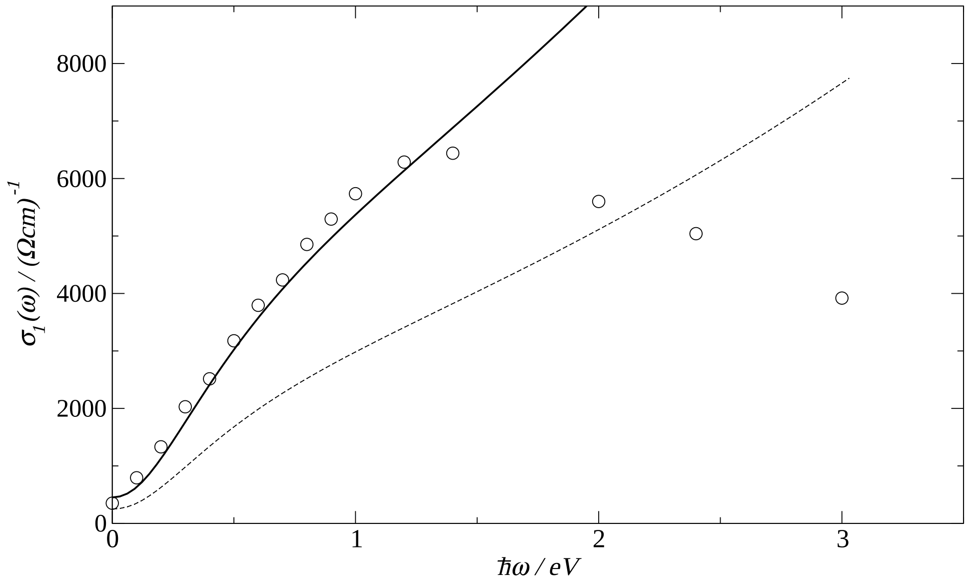

Figure 8.2: i-Al-Cu-Fe bulk quasicrystal, optical conductivity employing the resistivity Lorentzian model (lines) with different parameter sets (see text for details) and from a few selected experimental points (○) after [Homes 91] (the temperature is 295 K).

To compare this model with experiments we proceed as follows: i) the experimental optical conductivity [Homes 91], at 295 K, of the i-$Al_{63.5}Cu_{24.5}Fe_{12}$ quasicrystal is used for comparisons (circles in figure (8.2)), ii) the parameters used to model the spectral resistivity (conductivity) are those given in table (6.2) for i-$Al_{62.5}Cu_{25}Fe_{12.5}$ bulk quasicrystal (no additional fit is employed), and iii) two different values of A_{σ_1} are used in equation (8.7): 1 (figure (8.2), dashed lines) and 1.8 (figure (8.2), solid lines).

For low frequencies (below $\hbar\omega \approx 1.3$ eV), the modeled optical conductivity with $A_{\sigma_1} = 1.8$ is in good agreement with experiments. The results employing $A_{\sigma_1} = 1$ are lower. These differences may be attributed to the different chemical compositions between our modeled (12.5 at. % Fe) and the measured (12 at. % Fe) quasicrystal. Moreover, the optical conductivity is not sensitive to temperature changes (up to 300 K) or slight Fermi energy changes. Numerical calculations show that these differences are remarkable only for frequencies below ~250 meV.

For frequencies above $\hbar\omega \approx 1.3$ eV the model is not more applicable. For such frequencies, it is expected that the character of the states with energies ε and $(\varepsilon + \hbar\omega)$ changes strongly, which is not considered in the *ansatz* (8.7). To include this in our model we could introduce the information provided by the participation ratios, equation (6.1), defining[2], for example, $A_{\sigma_1}(\varepsilon_F, \varepsilon_F + \hbar\omega) \equiv A_{\sigma_1}(\hbar\omega) \equiv P(\varepsilon_F)/P(\varepsilon_F + \hbar\omega)$. In fact, for the i-Al-Cu-Fe approximant, this function decreases strongly after increasing $\hbar\omega$ (c.f. figure (6.5)). Thus, the experimentally observed optical conductivities can be *qualitatively* reproduced. The way to rescale this function to the quasicrystal is not obvious. This requires a more detailed study.

Finally, we want to analyse the influence of the narrow Lorentzian (modeled spectral fine structure) on changing only the parameter α (see equation (6.3)). Thus, after increasing α, $x = \alpha(\gamma_1/\gamma_2)$ increases (remember that x characterizes the quality of the quasicrystal, see figure (7.4)). At low frequencies, figure (8.3) shows that after increasing α (spectral fine structure) the observed optical conductivity can be reproduced. Note that for $\alpha = 0$ the optical conductivity behaves similar to the amorphous model (c.f. figure (8.1)). The reasons for the disagreement at frequencies higher than $\hbar\omega \approx 1.3$ eV were discussed above.

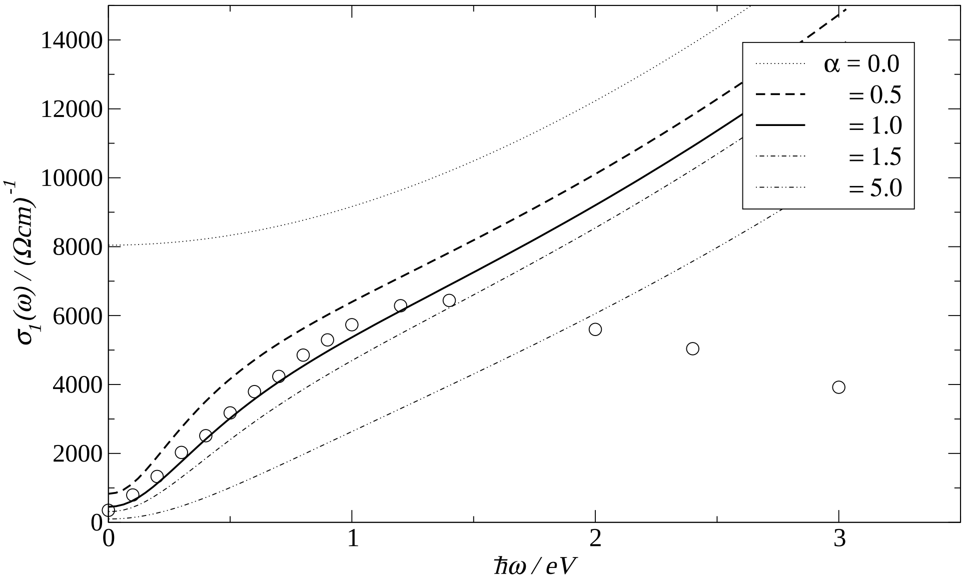

Figure 8.3: i-Al-Cu-Fe bulk quasicrystal, optical conductivity employing the resistivity Lorentzian model (lines) for different α values ($\alpha = 0$ means absence of the narrow Lorentzian) and fixed $A_{\sigma_1} = 1.8$. For comparisons, a few selected experimental points (○, [Homes 91]) are also drawn.

---

[2] This definition assures that one obtains the DC conductivity for $\hbar\omega \to 0$ ($A_{\sigma_1}(0) = 1$).

Chapter 9

A numerical study of icosahedral quasicrystals as thermoelectric materials

A good thermoelectric material should conduct electricity well and heat poorly. Thus, a thermoelectric device is efficient the more the larger is its *figure of merit*, Z. The figure of merit is given by the dimensionless expression,

$$\theta \equiv Z \cdot T = \frac{\sigma S^2}{K_t} T \quad , \tag{9.1}$$

where T is the temperature, S is the thermopower, σ is the electrical conductivity, and the total thermal conductivity, K_t, is given by the sum of the electronic, K, and lattice, K_L, parts.

For instance, Lenoir *et al.* [Lenoir 98] found in $Bi_{1-x}Sb_x$ alloys $\theta \approx 0.42$, around 60 K, and $\theta \approx 0.3$, around 300 K, for different x values. Similarly, half-Heusler LnPdSb structures have values of $\theta \approx 0.06$ at room temperature [Mastronardi 99]. Moreover, skutterudites ($\theta \approx 1.4$ at 600 K, [Sales 96]), Y_2O_3 porous ceramics ($\theta \approx 1$ at 950 K, [Koumoto 97]), or Tl_2SnTe_5 semiconductors ($\theta \approx 0.85$ at 400 K, [Sharp 99]) present θ values very close to the *practical upper limit* $\theta = 1$.

Quasicrystals are possibly qualified to provide good thermoelectric materials due to the inherently low thermal conductivity, 1-3 W/mK, which is less sensitive to small composition changes and the high thermopowers ($\sim 80\mu V/K$ in some cases [Pope 99]) as well as the broad conductivity range, 0.01-5000 $(\Omega cm)^{-1}$. Experimental studies show low values compared with the best-known thermoelectric materials (see above). For i-Al-Pd-Mn, Pope *et al.* found $\theta \approx 0.08$ at room temperatures [Pope 99]. In the case of i-Al-Cu-Fe, the absolute values of θ are less than 0.003 [Bilušić 01]. However, it is reasonable to expect that manipulating the composition, synthesis, or annealing conditions, higher θ values may be obtained, as pointed out in [Pope 99, Maciá 00b].

Recently Maciá studied theoretically the prospectives of quasicrystals as thermoelectric materials [Maciá 00b, Maciá 01]. Employing a two-dip spectral conductivity model, $\sigma(\varepsilon) \equiv \lambda_1\delta(\varepsilon - \varepsilon_1) + \lambda_2\delta(\varepsilon - \varepsilon_2)$, he obtains *optimal* θ values which are remarkably high compared with the usual non-metallic thermoelectric materials. Moreover, Maciá proposed the binary Cd-Yb quasicrystal, and the dodecagonal quasicrystalline chalcogenide TaTe phase as two promising candidates to be applied as thermoelectric devices [Maciá 01].

In the following, we study the spectral and temperature dependent properties of the i-Al-Cu-Ru quasicrystal. After comparing these results with those for i-Al-Cu-Fe (chapter 6), some conclusions about the figure of merit of aluminium based icosahedral quasicrystals/approximants can be drawn.

9.1 Modeling the transport coefficients of the i-Al-Cu-Ru quasicrystal

Ab-initio spectral properties of the approximant phase

The γ-Al-Cu-Ru approximant [Sugiyama 98b] with lattice constant $a = 15.38$Å and 248 atoms per unit cell has been constructed employing the crystallographic data of table (D.1). Then, by means of the LMTO-ASA supercell method (see chapter 5), we calculate the electronic state density, diffusivity, resistivity, and participation ratios. The results are drawn in figure (9.1).

The state density has the following properties: i) a wide pseudogap around the Fermi energy (width ∼1.5 eV), ii) two peaks around 4 eV and 1.5 eV below the Fermi energy due to Cu and Ru atoms, respectively (similar to i-Al-Cu-Fe, c.f. figures (6.4) and (6.5)), and iii) narrow pseudogaps of the order of ∼100 meV. In the spectral resistivity, a narrow peak around ∼0.275 eV is found. This narrow peak is related with a state density (and diffusivity) minimum. At -4 eV, the diffusivity is very low, ∼0.25 cm^2/s, which is related with low participation ratios. Around the Fermi energy, the participation ratio changes strongly.

These results show that the amount of the states alone can not explain high resistivities. The character of the states, expressed in the diffusivity, is also important. The rapid change of this character, also expressed in the participation ratios, provides fine structure of the spectral resistivity.

Transport coefficients of the i-Al-Cu-Ru quasicrystal

The spectral resistivity of the γ-Al-Cu-Ru approximant can be modeled by a wide and a narrow Lorentzian, in similar form as for i-Al-Cu-Fe (see chapter 6.3). In the temperature range to be considered here (up to 300 K), only the spectral features of the spectral resistivity (conductivity) around the Fermi energy (±1 eV) are important (c.f. figure (6.14)). Really, there are other narrow peaks between 0.5 and 1 eV above of the Fermi energy. They could be included into the modeling by ad-

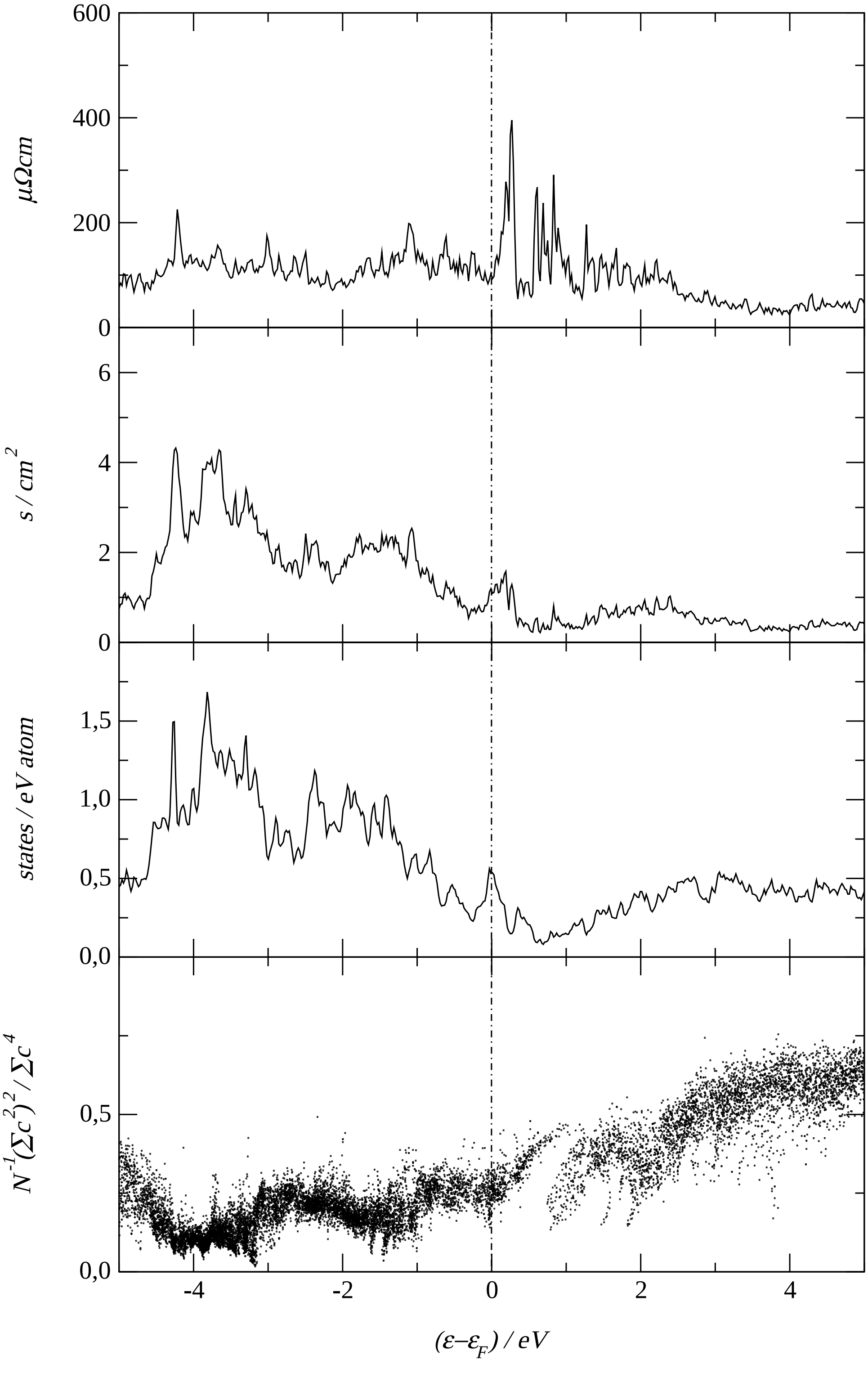

Figure 9.1: Spectral properties of the γ-Al-Cu-Ru approximant. From top to bottom: spectral resistivity, inverse of the electronic diffusivity, state density, and participation ratios. LMTO-ASA supercell calculations with $\underline{K}^{(3)}$, and Lorentzian half-width of $\Gamma = 20$ meV.

ditional Lorentzians. However, numerical comparisons show that the contributions are small. Thus, for simplicity, in the present study we consider again only a wide and one narrow Lorentzian.

Hence, this spectral resistivity can be employed to model the conductivity and thermopower obtained experimentally [Pierce 93a]. The fitting procedure is similar to that employed for i-Al-Cu-Fe (see chapter 6.3). The parameters are listed in table (9.1). As explained in chapter 6, the Fermi energy of the real quasicrystal may be shifted on the scale 100 meV with respect to the self-consistently calculated Fermi energy of the approximant. Here, as expected, the real Fermi energies lie in the narrow Lorentzian.

Table 9.1: Parameters used to model the spectral resistivities. $A = 471.25\mu\Omega\text{cmeV}$, $\delta_1 = -1.1eV$, $\delta_2 = 0.275eV$, and $\gamma_1 = 1eV$. $x = \alpha\gamma_1/\gamma_2$.

composition	α	γ_2 meV	$(\varepsilon_F - \delta_2)$ meV	ξ 10^{-6} eV/K^2	x	ρ_{4K} $\mu\Omega cm$
$Al_{64}Cu_{20}Ru_{15}Si_1$	1.9	70	-35	-0.140	27.140	3310
$Al_{68}Cu_{17}Ru_{15}$	1.7	45	11	0.120	37.780	5397
$Al_{65}Cu_{20}Ru_{15}$	2.5	32	4	0.127	78.125	11585

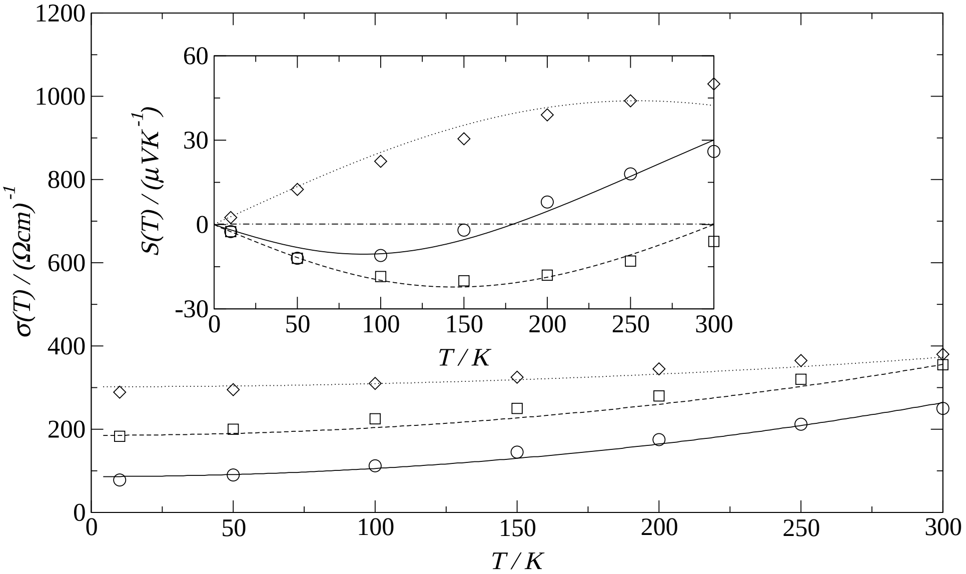

Figure 9.2: i-Al-Cu-Ru bulk quasicrystal, temperature dependence of the conductivity, and thermopower (inset), employing the resistivity Lorentzians model (lines) and from a few selected experimental points after [Pierce 93a]. Code: $Al_{64}Cu_{20}Ru_{15}Si_1$ (◇, dots), $Al_{68}Cu_{17}Ru_{15}$ (□, dashed), and $Al_{65}Cu_{20}Ru_{15}$ (○, solid).

A good agreement between the experimental [Pierce 93a] and modeled temperature dependent conductivities and thermopowers is found, see figure (9.2). Moreover, one can employ the modeled spectral resistivities to calculate other transport coefficients. Figure (9.3) shows the temperature dependent Hall coefficient, electronic thermal conductivity, and Lorenz number.

The temperature dependent trends of the Hall coefficient correspond to those found experimentally [Pierce 93a]. Note the sign correlation of the Hall coefficient with the thermopower (c.f. figures (9.2) and (9.3)). This is expected from the *ansatz* (6.2) and equation (6.5). However, for the $Al_{64}Cu_{20}Ru_{15}Si_1$ sample, a negative Hall coefficient with a positive thermopower is experimentally found [Pierce 93a].

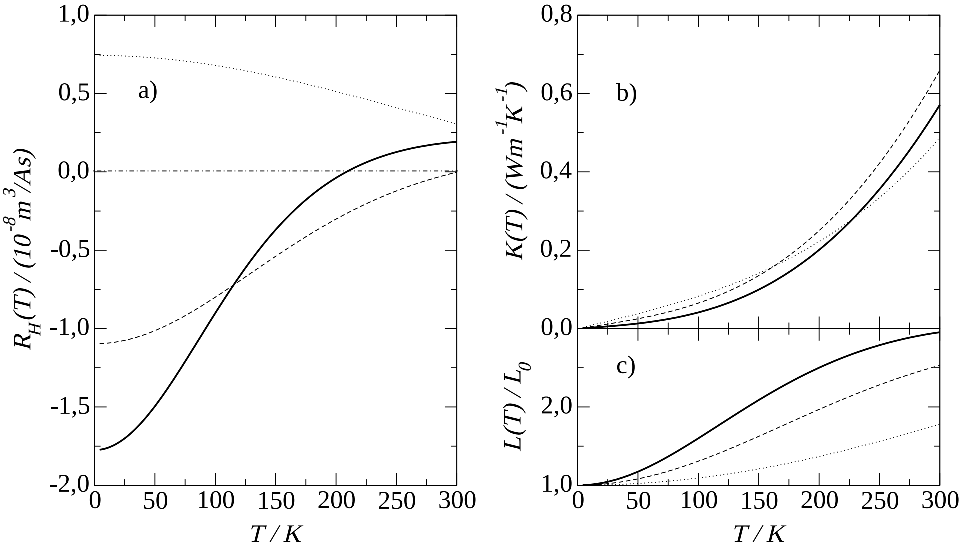

Figure 9.3: i-Al-Cu-Ru bulk quasicrystal, temperature dependence of a) the Hall coefficient with $Q = 2 \times 10^5 Am^2$, b) the electronic thermal conductivity, and c) the Lorenz number. Code: $Al_{64}Cu_{20}Ru_{15}Si_1$ (dots), $Al_{68}Cu_{17}Ru_{15}$ (dashed), and $Al_{65}Cu_{20}Ru_{15}$ (solid).

The electronic part of the thermal conductivity for the i-Al-Cu-Ru samples is very low ($\sim$0.6 W/mK at 300 K) and (nearly) composition independent. On the other hand, the Lorenz number depends strongly on both, the temperature and the composition (for the most resistive sample $L(300K) \approx 3L_0$, where L_0 is the Wiedemann-Franz Lorenz number). These results are very similar to those found for i-Al-Cu-Fe (c.f. figure (6.19)).

9.2 Modeling the figure of merit of icosahedral quasicrystals

As explained at the beginning of this chapter, the figure of merit of a device should be as large as possible for effective thermoelectric generation. Correspondingly θ, equation (9.1), should be of the order unity. In the following, we evaluate the electronic contribution to θ (denoted by θ_e), which is obtained replacing the total thermal conductivity by its electronic part in equation (9.1).

The electronic contribution to θ for i-Al-Cu-X ($X = \mathrm{Fe}, \mathrm{Ru}$) quasicrystals and approximants is shown in figure (9.4). Note that θ_e is calculated employing the transport coefficients previously modeled without additional inputs (see figures (6.15), (6.16), (6.17), (6.19), (9.2) and (9.3)).

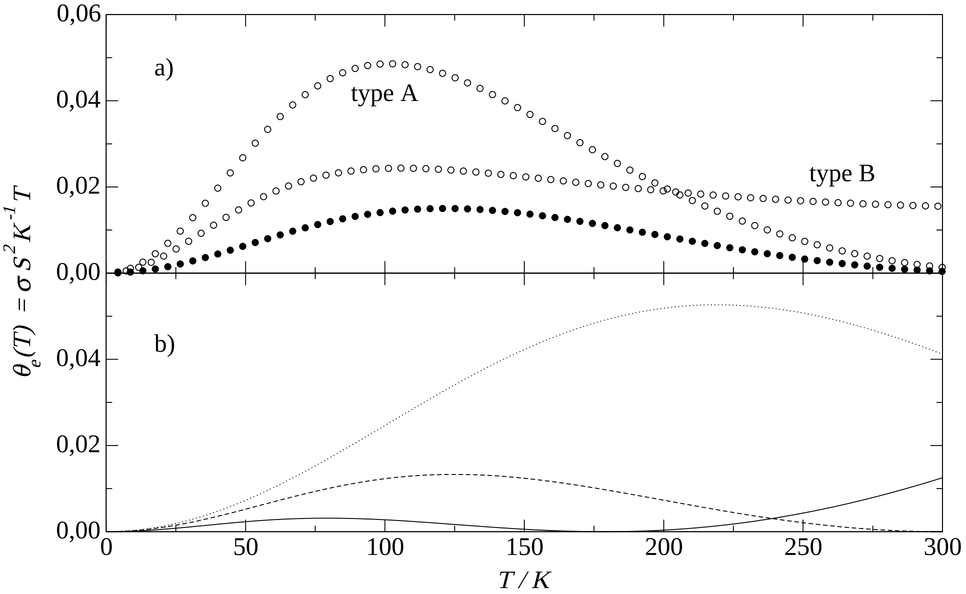

Figure 9.4: The figure of merit of icosahedral quasicrystals/approximants. a) i-Al-Cu-Fe phase: the approximant phase (○) with two trial Fermi energies (e.g. A,B) and the bulk quasicrystal (●). b) i-Al-Cu-Ru bulk quasicrystals. Code: $\mathrm{Al_{64}Cu_{20}Ru_{15}Si_1}$ (dots), $\mathrm{Al_{68}Cu_{17}Ru_{15}}$ (dashed), and $\mathrm{Al_{65}Cu_{20}Ru_{15}}$ (solid). See text for details.

As expected, θ_e depends strongly on the chemical composition through the conductivity, and specially the thermopower. The electronic thermal conductivity is nearly composition independent, c.f. figure (9.3). Moreover, θ_e has a strong temperature dependence (it follows mainly $S(T)^2$). The absolute values of θ_e are less than 0.06. After considering the lattice contribution to the thermal conductivity, θ can be one order of magnitude smaller than θ_e, because the lattice contribution to the thermal conductivity is at least one order of magnitude higher than the electronic part.

Considering the values of θ obtained here, one can say that the best-quality quasicrystals are not appropriate to be employed as thermoelectric devices. In fact, i-Al-Pd-Re samples should have θ values below 0.01 [Maciá 01]. Similarly, the recently discovered binary Cd-Yb quasicrystal present θ values of the order of 0.012 at room temperatures (experimental values of the transport coefficients has been taken from [Pope 01]).

Figure (9.4) shows that the highest θ values are provided by approximants (see the case of i-Al-Cu-Fe) or by disordered (more conductive) quasicrystals (see the case of i-Al-Cu-Ru). Finally, it is worth noting that it is hard to say, from the results presented here, if quasicrystals are, or are not, good thermoelectric materials. Much more detailed studies in different quasicrystals/approximants, under different conditions, are necessary to answer this question.

Chapter 10

Filtered electronic wave functions and transport

Filtered electronic wave functions

In this chapter we present some electronic wave functions filtered at certain energies. These filtered wave functions are obtained employing the TB-LMTO hamiltonian and the filter technique ($\underline{r}$-space method, see appendix B.2) on a spherical 1000 atom cluster model of the i-Al-Cu-Fe 1/1 approximant (Cockayne model [Cockayne 93]). The convergence of the filter procedure was discussed in appendix B, see figure (B.2).

The square amplitude per site in the orbital expansion of the electronic wave function is given by $|c_i|^2 = \sum_L |c_{i,L}|^2$ (the sum is performed over the L-orbitals, in this case $1s$, $3p$, and $5d$ orbitals). In figure (10.1) are presented the square amplitudes, $|c_i/c_{max}|^2$ (c_{max} is the largest amplitude), of the wave function at the corresponding energies. These square amplitudes are shown as spheres of different colors and radii. For example, the red spheres indicate that the probability to find the electron in that site is high.

Similar to the participation ratios, equation (6.1), we have two limiting cases: i) When only one coefficient c_k is different of zero, then $|c_k/c_{max}|^2 = 1$ only for $i = k$, otherwise zero (only one red sphere should be drawn). ii) When each coefficient $c_i = 1/\sqrt{N}$, then $|c_i/c_{max}|^2 = 1$ for all i (each site is drawn with a red sphere). The first case describes a localized[1] wave function. The second case, on the other hand, describes a wave function distributed homogeneously on all sites (extended wave functions).

Hence, one can see in figure (10.1) that the electronic wave functions are strongly energy dependent around the Fermi energy. Far away from the Fermi energy, trends toward extended wave functions are observed. At the Fermi energy, high square amplitudes are found at certain sites, which are not necessarily close together. In fact, a detailed analysis shows that high square amplitudes are placed at the Fe

---

[1] Remember that for approximants true localization can not be found due to the periodicity of the system.

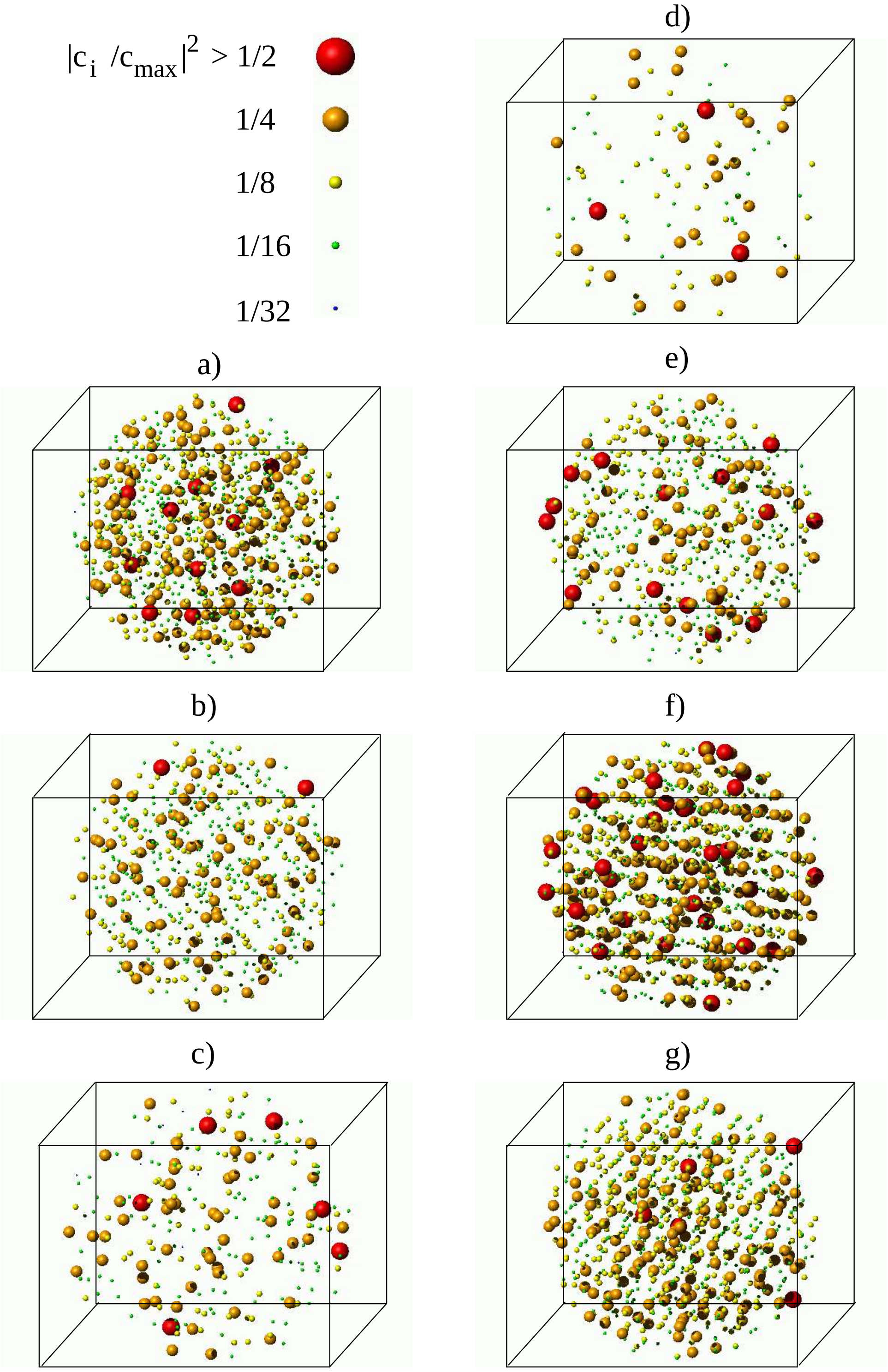

Figure 10.1: i-Al-Cu-Fe approximant, square amplitudes of electronic wave functions filtered at different energies: a) 8.024 eV, b) 8.704 eV, c) 9.384 eV, d) 10.064 eV (Fermi energy), e) 10.744 eV, f) 11.424 eV, and g) 12.104 eV. TB-LMTO basis and filter technique applied to a spherical cluster of the i-Al-Cu-Fe approximant (Cockayne model, [Cockayne 93]). The boxes are only guides for the eyes.

sites. More precisely, the d-component of the square amplitudes at the Fe sites are very high in comparison with other ℓ-components and other sites, see figure (10.2).

It is worth noting that these filtered wave functions do not follow *completely* the crystal symmetry and periodicity of the approximant (the 1000 atom cluster contains $\sim$8 unit cells). This should be due to the initial state in the filter procedure, which is a random combination of the TB-LMTO local orbitals (see equation (B.41)). This choice, of course, does not consider the periodicity of the approximant.

The participation ratios, calculated from equation (6.1) employing these filtered electronic wave functions, are shown in figure (10.2). As expected, at low energy resolution, these results are *qualitatively* comparable with those obtained from the LMTO-ASA supercell method (c.f. figure (6.5)).

Electronic wave functions (energies close to the Fermi energy) with high amplitudes only at the Fe-sites (as shown above) should explain *qualitatively* the high resistivity and the strong composition dependence of approximants/quasicrystals. In fact, electronic states with such wave functions have low diffusivities (due to the d-orbitals) providing high resistivities. Moreover, after increasing the content of Fe atoms, the number of sites of high wave function amplitudes increases. Correspondingly, the conductivity increases.

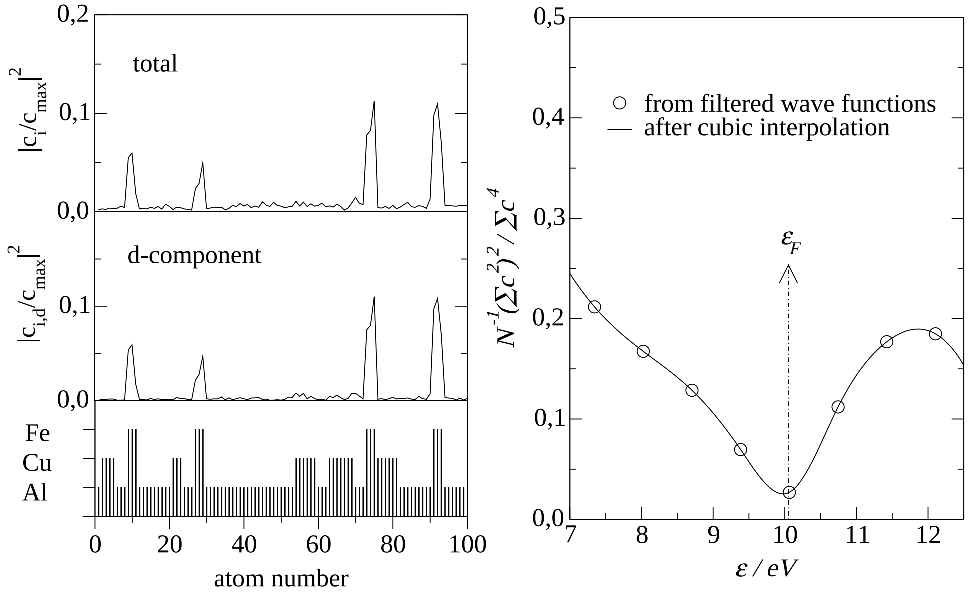

Figure 10.2: i-Al-Cu-Fe approximant. Left: square amplitudes of the filtered wave functions at the Fermi energy. High amplitudes are placed at the Fe-sites (see the atom-labels at the bottom). Moreover, these amplitudes are mainly due to the d-component. The atoms are numbered from the inner atom (1) to the most outer atom (1000), in figure are shown only the 100 innermost (the different heights indicate the type of the atom). Right: participation ratios around the Fermi energy obtained from the filtered wave functions.

Electronic transport

The electronic diffusivity can be calculated employing the TB-LMTO cluster recursion method and filtered wave functions at the Fermi energy as explained in chapter 5. The state density is calculated from equation (5.21), the electronic diffusivity is obtained from equation (5.27) employing ten different wave functions at the Fermi energy for the average, and the conductivity is calculated from the Einstein relation, equation (3.8).

Figure (10.3) shows the state density, inverse of the diffusivity, and the spectral resistivity. Spectral structure in the scale ~100 meV can not be found. The reason for this is two-fold. i) The local atomic environments are terminated beyond ~43 neighbors in the TB-LMTO hamiltonian (the increase of neighbors does not provide better results, this is due to the *tight-binding* character of the Hamiltonian[2]). On the other hand, as shown in chapter 6, spectral fine structures are due mainly to the Fe sub-system which produce long-range electronic interferences. These length scales are not reached by the TB-LMTO Hamiltonian. ii) The number of recursion coefficients and the cluster size employed are other factors that limit the energy resolution of the results.

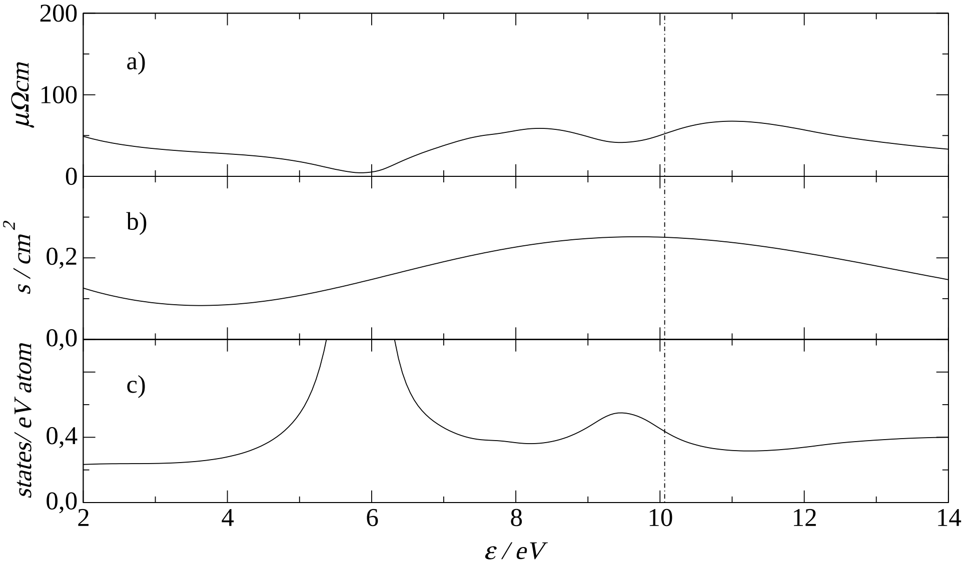

Figure 10.3: i-Al-Cu-Fe approximant. a) spectral resistivity, b) inverse of the electronic diffusivity, and c) state density obtained from the TB-LMTO cluster recursion method and filtered wave functions (see text for details). The number of recursion coefficients employed are 10 for the diffusivity, and 10, 20, and 30 for the s, p, and d orbital-depending state densities, respectively. The terminator employed here is there proposed by Beer and Pettifor [Beer 84] for the state density, and by Luchini and Nex [Luchini 87] for the diffusivity. The vertical line indicates the energy (Fermi energy) where the electronic wave function is filtered.

---

[2] More precisely, the TB-LMTO structure constants are short-ranged, see equations (B.27) and (B.28). Hence, the increase of neighbors will not improve the results considerably.

At low energy resolution, the agreement with the LMTO-ASA supercell method is *qualitatively* good. The state density shows two peaks at 4 eV and 1 eV below to the Fermi energy, which are due to the Cu and Fe atoms, respectively. Around the Fermi energy a wide pseudogap is also observed. The inverse of the diffusivity and the spectral resistivity can be described by a wide Lorentzian in similar form as for the LMTO-ASA supercell results (c.f. figure (6.14)). The absence of a narrow peak is expected from the discussion above.

The absence of a resistivity peak at 4 eV below the Fermi energy (as seen in LMTO-ASA supercell results, figure (6.5)) is expected because of the filter procedure, which provides the electronic diffusivity at the filtered energy only, c.f. equation (5.27).

A possible reason for the low resistivity at the Fermi energy (compared with LMTO-ASA supercell calculations, see figure (6.5)) is the approximation employed for the velocity matrix, equation (B.31), which neglects the overlap of the TB-LMTO basis.

Chapter 11

Summary and outlook

Summary

The present work deals with the influence of spectral fine structure on the electronic properties of quasicrystals/approximants. In fact, considering spectral fine structures of the order of ∼100 meV, a *consistent* explanation of the optical and temperature dependent properties of icosahedral quasicrystals containing transition metals could be achieved.

It was shown that three scales are present in the state-density/spectral-conductivity of these materials: i) A wide pseudogap, scale ∼1 eV, is common to other phases and is due to the Hume-Rothery mechanism of stability and hybridization effects. ii) Spectral features of the order of ∼100 meV are responsible for the *anomalous* electronic transport properties of quasicrystals/approximants. iii) Spikes (spectral features of the order of ∼10 meV) arise from both, computational limitations (small number of $\underline{k}$-points for Brillouin zone integrations) and elements of quasiperiodicity. However, spikes disappear after simulating the increase of the temperature by Lorentzian level broadening. That means, they are not stable and do not contribute to the transport.

The similarity of the electronic properties of approximants and quasicrystals indicates that extended quasiperiodicity[1] alone should not explain the electronic properties of quasicrystals. The right chemical order is also important. Therefore, in the present work *ab-initio* methods, which consider also the chemical order, have been employed to search for spectral features that are able to explain the electronic transport properties of quasicrystals/approximants. The idea is as follow: the *ab-initio* spectral resistivity of small approximants are modeled by Lorentzians. Thus, this model must consider the important spectral features of the basic cluster, its decoration, and its arrangement in the unit cell. In view of a related quasicrystal, which have similar local order, the model parameters have been fitted to a few reliable experimental data. Then, other experimental findings can be explained within this model. In fact, employing the Lorentzians model for the spectral resistivity,

---

[1] It puts only attention to the quasiperiodicity by itself neglecting the chemical decoration of the different components, see chapter 5.

equation (6.3), the temperature dependence of the conductivity, the thermopower, the Hall coefficient, and the electronic thermal conductivity have been explained for the icosahedral Al-Cu-Fe bulk quasicrystal, see chapter 6.3.

Futhermore, the inverse Matthiessen rule, equation (3.1), could be explained. It is fulfilled for systems that have the same constant slope of $\Delta_{qm}\widehat{\sigma}(\varepsilon)$ with respect to the energy. $\Delta_{qm}\widehat{\sigma}(\varepsilon)$ describes the change of the spectral conductivity on the quantum mechanical energy scale (level spacing). The sign correlations between the Hall coefficient and the thermopower, found in various quasicrystals/approximants, can also be considered by means of equation (6.5). Contrary to the Wiedemann-Franz law, it was numerically shown that the Lorenz number depends strongly on both, the temperature and the Fermi energy.

The origin of spectral features on the $\sim$100 meV scale, which was modeled by a simple narrow Lorentzian on the spectral resistivity, is a result of long-range electronic interferences of the transition metals. In fact, the Fe atoms (in the case of i-Al-Cu-Fe) build a Fibonacci-like planar order in three perpendicular directions which hinder the transport. After changing the Fe atom positions, the Fibonacci-like planar order is destroyed, and hence, the fine structure reduces. That means, there is an ideal transition metal concentration and decoration where the Fibonacci-like planar order is obtained. This explains the strong composition dependence of the transport properties. Moreover, these narrow features are related with anomalous diffusion. Indeed, it was shown that the transport regime in the narrow Lorentzian resistivity peak must be sub-diffusive. Correspondingly, Landauer/Büttiker calculations show that for such energies the resistance increases exponentially with the length of the sample. After changing the decoration of the transition metal sub-system a (nearly) ohmic-like behavior is found.

Comparing the spectral properties of approximants with Hume-Rothery crystals (non-approximants), one finds that not only the amount of states but also the kind of them are important for the transport. On other words, icosahedral quasicrystals containing transition metals are not Mott-like systems. As discussed in chapter 3.2, in these cases the use of Kubo-Greenwood formulas is necessary.

A possible scenario for the metal-insulator transition in the i-Al-Pd-Re quasicrystal was also discussed. To explain the temperature dependent conductivity (below 100 K) of the more resistive samples a modified spectral conductivity, which contains a real gap, should be necessary. After changing the Re concentration or increasing the temperature (above 100 K) the real gap closes to a pseudogap and the transport can be explained by the usual Lorentzians model for the spectral resistivity.

The low frequency optical conductivity has also been explained by the presence of spectral fine structure. Based on the Lorentzians model for the spectral resistivity, we have modeled the optical conductivity of quasicrystals. The results are in good agreement with experiments (see figure (8.2)). However, for high frequencies the model is not more applicable: the strong changing character of the states for different energies (which is not considered in equation (8.7)) becomes important.

Finally, in chapter 9 was also discussed the applicability of icosahedral quasicrystals as thermoelectric devices. The results presented here could not provide a conclusive answer to this question.

Outlook

In the following we comment on a few questions which remain open and that can be matter of further discussions in a next work.

A more complete understanding of the *ansätze* for the spectral Hall conductivity, equation (6.2), and for the model for the optical conductivity, equation (8.7), is expected. The validity and/or limitations of such *ansätze* are given mainly comparing the results with experiments, however, a more realistic theoretical background should be found.

A systematic study of the spectral properties of approximants of different orders is urgently required. Thus, one could find characteristic spectral features that change their absolute values only after increasing the order of the approximant, as expected in our rescaling procedure for the Lorentzians model of the spectral resistivity. As discussed in chapter 5, the LMTO-ASA supercell cell method is limited to low order approximants, and the TB-LMTO cluster recursion method cannot provide spectral features of the order of ∼100 meV (see chapter 10). The muffin-tin scattered-wave method together with the recursion procedure can work with large clusters (of the order of ∼5000 atoms) and can also provide fine spectral features as expected for quasicrystals. Calculations in low order approximants show spectral features of this order [Solbrig 00a].

Since the proposal of the generalization of the Boltzmann-Gibbs statistics by Tsallis [Tsallis 88], many authors have applied this new formalism to different situations, where for instance, long-range interactions, sub-diffusive transport, and multifractal behavior of the electron are present (see [Tsallis 99] and references therein). These features are typical for quasicrystals/approximants, in this sense, it will be interesting to test the influence of Tsallis statistic on the transport coefficients of quasicrystals. For instance, Oliveira shows [Oliveira 00] that under the Tsallis statistics some quantities, such as the specific heat, exhibit new terms (in comparison with the usual Fermi-Dirac statistics) after employing the Sommerfeld expansion.

Appendix A

Transport parameters from the linear response formulas

A.1 Kubo-Greenwood conductivity

In the following we will present a brief derivation of the Kubo-Greenwood conductivity based on [Mott 87]. For rigorous deductions the reader is referred, for instance, to [Mahan 90, Nolting 97].

In the framework of the linear response theory for an electron in an external electric field, $\underline{\hat{e}}_z E cos(\omega t)$, the Fermi golden rule provides the transition rate for one electron to make a transition from an initial state $|i\rangle$ (energy ε_i) to a final state $|j\rangle$ (energy ε_j) as,

$$\gamma_{ji}(\omega) = \frac{2\pi}{\hbar} e^2 |E|^2 |\langle j|z|i\rangle|^2 (\delta(\hbar\omega - \varepsilon_{ji}) + \delta(\hbar\omega + \varepsilon_{ji})) \quad , \tag{A.1}$$

where, $\varepsilon_{ji} = \varepsilon_j - \varepsilon_i$. The mean rate of energy loss is given by,

$$P = \frac{1}{2} \sum_{i,j} \varepsilon_{ji} \left\{ (1 - f_j) f_i \gamma_{ji} - (1 - f_i) f_j \gamma_{ij} \right\} \quad , \tag{A.2}$$

where, f_i is the Fermi-Dirac distribution function (A.9) with energy ε_i. Hence, inserting (A.1) into (A.2) and after some algebraical reductions one obtains,

$$P = \left\{ \pi\hbar e^2 \sum_{i,j} |\langle j|v|i\rangle|^2 \frac{f_i - f_j}{\hbar\omega} \delta(\hbar\omega - \varepsilon_{ji}) \right\} |E|^2 \quad , \tag{A.3}$$

where, v is the z-component of the velocity operator.

On the other hand, Ohm's law gives $P = \sigma_1(\omega)\Omega|E|^2$ (Ω is the volume of the system), then comparing with (A.3) the AC conductivity can be expressed by,

$$\sigma_1(\omega) = 2\frac{\pi\hbar e^2}{\Omega} \int d\varepsilon \left\{ \sum_{i,j} |\langle j|v|i\rangle|^2 \left(-\frac{f_j - f_i}{\hbar\omega} \right) \delta(\varepsilon + \hbar\omega - \varepsilon_j) \right\} \delta(\varepsilon - \varepsilon_i) \quad . \tag{A.4}$$

The prefactor 2 consider both spin-components. Considering that in the limit $\omega \to 0$, $-(f_j - f_i)/(\hbar\omega) \to -(\partial f/\partial\varepsilon)$, the temperature dependence of the DC conductivity is given by,

$$\sigma(T) = \int d\varepsilon \left(-\frac{\partial f}{\partial \varepsilon}\right) \widehat{\sigma}(\varepsilon) \quad . \tag{A.5}$$

$\widehat{\sigma}(\varepsilon)$ is the spectral conductivity,

$$\widehat{\sigma}(\varepsilon) = 2\frac{\pi\hbar e^2}{\Omega} \sum_{i,j} |\langle i|v|j\rangle|^2 \, \delta(\varepsilon - \varepsilon_i)\delta(\varepsilon - \varepsilon_j) \quad . \tag{A.6}$$

In the limit $T \to 0$, we obtain $-(\partial f/\partial\varepsilon) \to \delta(\varepsilon - \varepsilon_F)$, and from equation (A.5) finally $\sigma(0) = \widehat{\sigma}(\varepsilon_F)$, the spectral conductivity at the Fermi energy.

A.2 Relation between the kinetic and transport coefficients

Kinetic coefficients

Currents $\mathbf{J}_i$ are a results of *forces* $\mathbf{X}_i$ on the system. For example, an uniform electric field, $\mathbf{E}$, and a temperature gradient, ∇T, produce electric currents, density $\mathbf{j}$, and thermal currents, density $\mathbf{j}^q$. Then, the response of a system to $\mathbf{E}$ and ∇T up to *linear* order can be written (considering that there is no concentration gradient) as [Callen 85],

$$\begin{aligned} \mathbf{j} &= \quad \mathcal{L}_{11}\mathbf{E} - \frac{1}{|e|T}\mathcal{L}_{12}\nabla T \\ \mathbf{j}^q &= \frac{1}{|e|}\mathcal{L}_{21}\mathbf{E} - \frac{1}{e^2T}\mathcal{L}_{22}\nabla T \quad . \end{aligned} \tag{A.7}$$

The kinetic coefficients $\mathcal{L}_{ij}$ are the key to calculate the transport coefficients. The Onsager relations specify that in the absence of a magnetic field $\mathcal{L}_{12} = \mathcal{L}_{21}$. However, in general the Onsager relationships are not valid for any arbitrary choice of currents and forces. A criterion for choosing the forces and currents has been given by de Groot [de Groot 52]. Following Mahan [Mahan 90], in a nonequilibrium process, there is a net generation of entropy, so that $\partial \mathsf{S}/\partial t > 0$ (S is just the part of the entropy which is generated nonreversibly). If one requires that this be expressed as

$$\frac{\partial \mathsf{S}}{\partial t} = \sum_i \mathbf{J}_i \cdot \mathbf{X}_i \quad ,$$

then the Onsager relations are valid. This is the case for equation (A.7).

The coefficients $\mathcal{L}_{ij}$ are correlation functions of current operators. They are obtained using the Chester-Thellung-Kubo-Greenwood formulation of the linear response theory [Chester 61, Kubo 57, Greenwood 58]. For non-interacting particles, they are reduced to,

$$\mathcal{L}_{ij}(T) = (-1)^{i+j} \int d\varepsilon \ \widehat{\sigma}(\varepsilon) \ (\varepsilon - \mu)^{i+j-2} \ \left(-\frac{\partial f(\varepsilon, \mu, T)}{\partial \varepsilon} \right) \tag{A.8}$$

where

$$f(\varepsilon, \mu, T) = \frac{1}{e^{(\varepsilon - \mu)/k_B T} + 1} \tag{A.9}$$

is the Fermi-Dirac distribution function, and

$$\mu(T) \approx \varepsilon_F - \xi T^2 \tag{A.10}$$

is the chemical potential with $\xi = (\pi^2/6)[(d\widehat{n}/d\varepsilon)/\widehat{n}]_{\varepsilon_F} k_B^2$ [Ashcroft 76].

Transport coefficients

In the absence of ∇T, the conductivity is the proportionality constant between the electric current density and the electric field (Ohm's law). Thus, taking $\nabla T = 0$ in equation (A.7),

$$\sigma(T) = \mathcal{L}_{11}(T) \quad . \tag{A.11}$$

Note that equations (A.5) and (A.11) express the same result.

The electric field generated by a finite temperature gradient in an open circuit is known as the Seebeck effect. Thus, the proportionality constant between the electric field and the temperature gradient is called the thermoelectric power or thermopower. Taking $\mathbf{j} = 0$ in equation (A.7),

$$S(T) = \frac{1}{|e| T} \frac{\mathcal{L}_{12}(T)}{\sigma(T)} \quad . \tag{A.12}$$

Note that due to the temperature gradient, measures of the thermopower requires of a reference sample whose thermopower is known. For instance, superconductors can be employed (at low temperatures) for such a measure because they have zero thermopower [Ashcroft 76].

Fourier's law gives the relation between the thermal current density and the temperature gradient, $\mathbf{j}^q = K(-\nabla T)$, where K is the thermal conductivity. Thus, taking $\mathbf{j} = 0$ in equation (A.7), the electronic part of the thermal conductivity is written as,

$$K(T) = \frac{1}{e^2 T} \mathcal{L}_{22}(T) - T\sigma(T) \ S(T)^2 \quad . \tag{A.13}$$

The Lorenz number, written as

$$L(T) = \frac{K(T)}{T \ \sigma(T)} \quad , \tag{A.14}$$

should be temperature independent if the empirical Wiedemann-Franz law holds. The validity of this law for quasicrystals is analyzed in the present work.

On the other hand, the magneto-transport is less clearly understood. As yet, even the question is not conclusively answered whether it can be explained as an on-the energy-shell transport [Morgan 85, Itoh 92]. In presence of a weak magnetic field, B, the Hall coefficient is phenomenologically defined as $R_H = \sigma_{xy}(B)/(B\sigma^2)$ [Cusack 87]. However, the non-diagonal conductivity (also called Hall conductivity), σ_{xy}/B, is cumbersome of handling [Morgan 85]. A possible expression for the Hall coefficient is given by a Hall conductivity, σ_H, which depends of diagonal transport quantities only (see equation (6.2)). Hence, one can write

$$R_H(T) = \frac{1}{\sigma^2(T)}\sigma_H(T) = \frac{1}{\sigma^2(T)}\int d\varepsilon\ \widehat{\sigma}_H(\varepsilon)\ \left(-\frac{\partial f(\varepsilon,\mu,T)}{\partial\varepsilon}\right) \quad . \tag{A.15}$$

Finally, it is important to mention that all system-dependent features necessary to calculate the transport coefficients, equations (A.11)-(A.15), are provided by $\widehat{\sigma}(\varepsilon)$, respectively, $\widehat{\sigma}_H(\varepsilon)$. That means, comparisons between different materials should be made at the level of their spectral properties.

Appendix B

Supplement of the employed methods

B.1 LMTO-ASA supercell method

KKR-ASA secular equation and energy independent basis

In the following, the Korringer-Kohn-Rostoker secular equation (5.7) will be obtained after solving the Schrödinger equation (5.2) for a muffin-tin potential (5.4) within the atomic sphere approximation ($S_{\underline{R}} = S_{\underline{R}}^{WS}$).

The muffin-tin potential divides the space in the form shown in figure (5.1). Due to the fact that the potential is spherically symmetric, it is useful to employ spherical coordinates. In the same form, the solutions, called partial waves, can be expressed as $\phi_{\underline{R}L}(r_{\underline{R}}, \varepsilon) \equiv \phi_{\underline{R}\ell}(r_{\underline{R}}, \varepsilon) Y_L(\hat{\underline{r}}_{\underline{R}})$, which is a product of a radial, $\phi_{\underline{R}\ell}$, and angular, $Y_L(\hat{\underline{r}}_{\underline{R}})$ (spherical harmonics), part. Thus, the radial part of the Schrödinger equation inside the sphere $\underline{R}$ ($r < S_{\underline{R}}$) can be written as,

$$\left\{ -\frac{\partial^2}{\partial r^2} - \frac{2}{r}\frac{\partial}{\partial r} + \frac{\ell(\ell+1)}{r^2} + V_{\underline{R}}(r) - \varepsilon \right\} \phi_{\underline{R}\ell}(r, \varepsilon) = 0 \quad . \tag{B.1}$$

This equation can be solved numerically. Three items are worth noting, i) equation (B.1) must be solved selfconsistently with the muffin-tin potential (5.4) which is a function of the charge density (5.3), ii) the energy ε is a parameter which is fixed to the eigenvalue of the system when the boundary conditions at the atomic surface $S_{\underline{R}}$ are realized, and iii) the partial waves fulfill the normalization condition for the radial amplitude, $\int_0^{S_{\underline{R}}} dr\, r^2\, |\phi_{\underline{R}l}(r, \varepsilon)|^2 = 1$, where $\phi_{\underline{R}\ell}(r, \varepsilon) \propto r^\ell$ for $r \to 0$.

Next one has to solve the Schrödinger equation in the interstitial region. However, due to the complicate shape of the interstitial region, this is not a straightforward task. Effective is to solve the Schrödinger equation in the absence of any atomic sphere. Under the ASA, one puts the kinetic energy in the interstitial region zero and thus the problem reduces to solve the Laplace equation, $\nabla^2 \Psi(\underline{r}) = 0$. Hence, the Laplace equation, centered at $\underline{R}$ and expressed in spherical coordinates, has two types of solutions: regular ones (Bessel function $J_L(r_{\underline{R}}) \equiv J_\ell(r) Y_L(\hat{\underline{r}}_{\underline{R}})$) and singular ones (Neumann function $K_L(r_{\underline{R}}) \equiv K_\ell(r) Y_L(\hat{\underline{r}}_{\underline{R}})$) according to the asymptotic behavior for $r \to 0$. Their radial parts are written as,

$$J_\ell(r) = \frac{1}{2(2\ell+1)} \left(\frac{r}{w}\right)^\ell \quad \texttt{and} \quad K_\ell(r) = \left(\frac{w}{r}\right)^\ell \quad , \tag{B.2}$$

where w is usually the average Wigner-Seitz radius (5.5).

The expansion theorem [Andersen 84a, Skriver 84] give us the possibility to describe the irregular solution $K_L(r_{\underline{R}})$, centered at $\underline{R}$, as a combination of regular solutions $J_{L'}(r_{\underline{R}'})$, centered at $\underline{R}'$, in the following way,

$$K_L(r_{\underline{R}}) = -\sum_{L'} \mathcal{S}^0_{\underline{R}'L',\underline{R}L} J_{L'}(r_{\underline{R}'}) \quad , \tag{B.3}$$

where the sum is performed for all $\underline{R}' \neq \underline{R}$. Here $\mathcal{S}^0_{\underline{R}'L',\underline{R}L}$ are the so-called canonical structure constants and are given by [Skriver 84, Turek 97],

$$\mathcal{S}^0_{\underline{R}'L',\underline{R}''L''} = \sum_L (-1)^{\ell''+1} \frac{8\pi(2\ell-1)!!C_{LL'L''}}{(2\ell'-1)!!(2\ell''-1)!!} K_L(\underline{R}'' - \underline{R}') \quad , \tag{B.4}$$

where the sum is limited to ℓ-values for which the condition $\ell = \ell' + \ell''$ is successful. The $C_{LL'L''}$ are the Gaunt coefficients and $(2\ell+1)!! = (2\ell+1)(2\ell-1)!!$ with $(-1)!! = 1$.

Now, the <u>m</u>uffin-<u>t</u>in <u>o</u>rbital basis, MTO, defined in the whole space, can be built as a combination of the partial waves and the regular solutions, $\mathcal{N}^0_{\underline{R}L}(\varepsilon)\phi_{\underline{R}L}(r_{\underline{R}},\varepsilon) + P_{\underline{R}L}(\varepsilon)J_{\underline{R}L}(r_{\underline{R}})$, within the atomic sphere $\underline{R}$. The function $K_{\underline{R}L}(r_{\underline{R}})$, centered at $\underline{R}$, is taken for the interstitial region, and for the other spheres the solution is given by the expansion of equation (B.3). Thus, the muffin-tin orbitals can be written as,

$$\begin{aligned} \chi_{\underline{R}L}(r_{\underline{R}},\varepsilon) = \mathcal{N}^0_{\underline{R}L}(\varepsilon)\phi_{\underline{R}L}(r_{\underline{R}},\varepsilon) \\ + \sum_{\underline{R}'L'} J_{\underline{R}'L'}(r_{\underline{R}'}) \left\{ \mathcal{P}^0_{\underline{R}'L'}(\varepsilon)\delta_{\underline{R}'L',\underline{R}L} - \mathcal{S}^0_{\underline{R}'L',\underline{R}L} \right\} \\ + K_{\underline{R}L}(r_{\underline{R}}) \quad . \end{aligned} \tag{B.5}$$

Hence, the solution of the Schrödinger equation (5.2), in the MTO basis, can be written as $\Psi(\underline{r},\varepsilon) = \sum_{\underline{R}L} \chi_{\underline{R}L}(r_{\underline{R}},\varepsilon)\breve{a}_{\underline{R}L}$. After replacing the MTO basis (B.5), one can see that this solution satisfy the Schrödinger equation, inside $\underline{R}'$, only when the coefficients of $J_{\underline{R}'L'}(r_{\underline{R}'})$ vanish. This is known as the *tail-cancellation condition* and gives the KKR-ASA secular equation (5.7),

$$\sum_{\underline{R}L} \breve{a}_{\underline{R}L} \left\{ \mathcal{P}^0_{\underline{R}L}(\varepsilon)\delta_{\underline{R}'L',\underline{R}L} - \mathcal{S}^0_{\underline{R}'L',\underline{R}L} \right\} = 0 \quad .$$

The matching condition of the partial waves with the radial parts of $J_{\underline{R}L}$ and $K_{\underline{R}L}$, at the atomic surface $S_{\underline{R}}$, defines the potential function $\mathcal{P}^0$ [Andersen 84a, Turek 97],

$$\mathcal{P}_{\underline{R}\ell}(\varepsilon) = 2(2\ell+1)\left(\frac{w}{S_{\underline{R}}}\right)^{2\ell+1} \frac{D_{\underline{R}l}(\varepsilon) + \ell + 1}{D_{\underline{R}l}(\varepsilon) - \ell} \quad , \tag{B.6}$$

where $D_{\underline{R}l}(\varepsilon) = [r\phi'_{\underline{R}\ell}(r,\varepsilon)/\phi_{\underline{R}\ell}(r,\varepsilon)]\big|_{r=S_{\underline{R}}}$, with $\phi'_{\underline{R}\ell} = d\phi_{\underline{R}\ell}/dr$. Corresponding, the normalization function $\mathcal{N}^0$ is given by [Andersen 84a, Turek 97],

$$\mathcal{N}_{\underline{R}\ell}(\varepsilon) = (2\ell+1)\left(\frac{w}{S_{\underline{R}}}\right)^{\ell+1} \frac{1}{\phi_{\underline{R}\ell}(S_{\underline{R}},\varepsilon)} \frac{1}{\ell - D_{\underline{R}\ell}(\varepsilon)} \quad . \tag{B.7}$$

The problems to treat the KKR-ASA secular equation comes from the non-linear energy dependence of the potential function. Its linearization follows from equation (5.10) (indices $\underline{R}\ell$ omited)

$$\mathcal{P}^0(\varepsilon)^{-1} \simeq \frac{\Delta}{\varepsilon - C} + \gamma \quad .$$

This is related to an energy linearization of the radial part of the partial wave around some reference energy $\varepsilon_{\underline{R}\ell,\nu}$ which is chosen usually in the center of the occupied part of the valence state density of the orbital ℓ. The linear muffin-tin orbitals are obtained after a Taylor expansion of the radial part of the partial wave, $\phi_{\underline{R}\ell}(r,\varepsilon) = \phi_{\underline{R}\ell}(r,\varepsilon_\nu) + \dot{\phi}_{\underline{R}\ell}(r,\varepsilon_\nu)(\varepsilon - \varepsilon_{\underline{R}\ell,\nu}) + ...$, and replacing $K_\ell(r)$ and $J_\ell(r)$ by linear combinations of the energy independent $\phi_{\underline{R}\ell}(r,\varepsilon_\nu) \equiv \phi_{\underline{R}\ell,\nu}$ and $\dot{\phi}_{\underline{R}\ell}(r,\varepsilon_\nu) = [d\phi_{\underline{R}\ell}(r,\varepsilon)/d\varepsilon]\big|_{\varepsilon=\varepsilon_{\underline{R}\ell,\nu}} \equiv \dot{\phi}_{\underline{R}\ell,\nu}$, see equation (5.8).

Then, the potential parameters that linearize the potential function $\mathcal{P}_{\underline{R}\ell}(\varepsilon)$ are obtained from the condition that equations (B.6) and (5.10) coincide at the energy $\varepsilon = \varepsilon_{\underline{R}\ell,\nu}$ up to the second derivatives. The potential parameters are written as [Andersen 84a, Andersen 85] (indices $\underline{R}\ell$ omited),

$$\begin{aligned}
C &= \varepsilon_\nu - \frac{\phi_\nu}{\dot{\phi}_\nu}\frac{D[\phi_\nu]+\ell+1}{D[\dot{\phi}_\nu]+\ell+1} \quad , \\
\Delta &= -\frac{1}{2S_{\underline{R}}}\left(\frac{S_R}{w}\right)^{2\ell+1}\left\{\frac{1}{\dot{\phi}_\nu(D[\dot{\phi}_\nu]+\ell+1)}\right\}^2 \quad , \quad \texttt{and} \\
\gamma &= \frac{1}{2(2\ell+1)}\left(\frac{S_R}{w}\right)^{2\ell+1}\frac{D[\dot{\phi}_\nu]-\ell}{D[\dot{\phi}_\nu]+\ell+1} \quad ,
\end{aligned} \tag{B.8}$$

where the logarithmic derivative is defined as $D[f] = [rf'/f]\big|_{r=S_{\underline{R}}}$ with $f' = df/dr$.

Velocity matrix in the LMTO-ASA representation

The calculation of the Kubo-Greenwood spectral conductivity, equation (3.5), requires the LMTO-ASA eigenfunctions, $\Psi^{\underline{k},(i)}$, and eigenvalues, $\varepsilon^{\underline{k},(i)}$, which are obtained after solving the eigenvalue problem. Finally, the matrix elements $\langle\Psi^{\underline{k},(i)}|v_x|\Psi^{\underline{k},(j)}\rangle$ must be evaluated.

Two ways are usually employed to obtain these velocity-matrix elements. One possibility is to replace the velocity operator by $v_x = i[\mathcal{H},x]/\hbar$. Thereby follows the calculation of Hamilton and position operators in the LMTO-ASA basis. However, the matrix elements of the position operator can be determined only approximatively [Bose 93]. This position operator, equation (B.30), contains a term, called *dipol-term*, which is neglected (this will be discussed in appendix B.2). Moreover, supercell calculations give additional problems in the calculation of the position operator: position-matrix elements of far a way atoms must be taken into account, the periodicity must be considered completely, as was pointed out in [Arnold 97].

A more advantageous way to calculate the velocity-matrix elements employs the wave function as obtained from the supercell LMTO-ASA,

$$|\Psi^{\underline{k},(i)}\rangle = \sum_{\underline{B}L} A^{\underline{k},(i)}_{\underline{B}L} |\phi_{\underline{B}L,\nu}\rangle \; + B^{\underline{k},(i)}_{\underline{B}L,} |\dot{\phi}_{\underline{B}L,\nu}\rangle \qquad , \tag{B.9}$$

where the coefficients A and B are obtained from equations (5.17) and (5.8). Thus, the calculation of the velocity-matrix elements can be realized from atom-spheres integrations [Hobbs 95, Arnold 97]. Because of the Bloch-periodicity it is only necessary to calculate transitions of wave functions with the same $\underline{k}$ vectors [Arnold 97]. Then, the integration is restricted only to the unit-cell volume, Ω_{cell}, which is used instead of the system volume, Ω, in equation (3.5).

As discussed by [Arnold 97], the analysis of the velocity-matrix elements prior to the atomic sphere approximation shows that certain surface integrals of the atomic polyhedra cancel due to translation symmetry. Thus, following the notation of [Arnold 97], the velocity elements can be written as (index $\underline{k}$ omited),

$$\begin{aligned}
\langle\Psi^{(i)}|v_x|\Psi^{(j)}\rangle &= \frac{i}{\hbar}\sum_{\underline{B}}\int_{[\underline{B}]} d^3\underline{r}\ \Psi_i^*\Big[\mathcal{H}x - x\mathcal{H}\Big]\Psi_j \\
&= \frac{i}{\hbar}\sum_{\underline{B}}\int_{[\underline{B}]} d^3\underline{r}\ \Psi_i^*\mathcal{H}x\Psi_j - x\Psi_j\mathcal{H}\Psi_i^* + (\varepsilon_i - \varepsilon_j)\Psi_i^* x\Psi_j \\
&= \sum_{\underline{B}}\frac{1}{2}\int_{A[\underline{B}]} \underline{dA}\ (\underline{e}_x\underline{r})\Big[\Psi_i^*\underline{v}\Psi_j - \Psi_j\underline{v}\Psi_i^*\Big] \\
&\quad + \frac{\hbar}{2im_e}\int_{A[\underline{B}]} \underline{dA}\ \underline{e}_x\Psi_i^*\Psi_j \\
&\quad (\varepsilon_i - \varepsilon_j)\frac{i}{\hbar}\int_{[\underline{B}]} d^3\underline{r}\ \Psi_i^* x\Psi_j \qquad ,
\end{aligned} \tag{B.10}$$

where $[\underline{B}]$ and $A[\underline{B}]$, in the integrals, are the polyhedron volume and the polyhedron surface at the atom $\underline{B}$, respectively. Arnold found that, employing periodic boundary conditions, the surface terms $\int \underline{dA}\ \underline{e}_x\Psi_i^*\Psi_j$ cancel out in the summation over neighboring polyhedra. Hobbs *et al.* [Hobbs 95] could not find this cancellation, because, they have used directly the LMTO-ASA expansion of the wave function, equation (B.9). Hence, with $\varepsilon_i = \varepsilon_j$ (only states on the energy shell) equation (B.10) reduces to the first term.

In difference to the state density, for systems containing strong scatterers (for instance, Cu and Fe in i-Al-Cu-Fe), the conductivity must be calculated including

f orbitals. This is due to the velocity matrix elements, which contain derivatives d/dr of the partial waves, equation (B.12). These derivatives require the additional consideration of angular-momentum with $\ell + 1$ [Arnold 97].

In summary, and following Arnold, the velocity-matrix elements in the LMTO-ASA are obtained after replacing (B.9) in (B.10). These elements are written as [Arnold 97] (index $\underline{k}$ omited),

$$\begin{aligned}\langle\Psi^{(i)}|v_x|\Psi^{(j)}\rangle = \sum_{\underline{B}LL'} \Big[& A^{*(i)}_{\underline{B}L} A^{(j)}_{\underline{B}L'} U^{00}_{\underline{B}LL'}(\underline{e}_x) + A^{*(i)}_{\underline{B}L} B^{(j)}_{\underline{B}L'} U^{01}_{\underline{B}LL'}(\underline{e}_x) \\ & + B^{*(i)}_{\underline{B}L} A^{(j)}_{\underline{B}L'} U^{10}_{\underline{B}LL'}(\underline{e}_x) + B^{*(i)}_{\underline{B}L} B^{(j)}_{\underline{B}L'} U^{11}_{\underline{B}LL'}(\underline{e}_x) \Big] \quad ,\end{aligned} \tag{B.11}$$

where (index $\underline{B}$ omited, SI-units)

$$\begin{aligned} U^{nm}_{LL'}(\underline{e}_x) &= \langle \overset{n}{\phi}_{L,\nu}|v_x|\overset{m}{\phi}_{L',\nu}\rangle - \frac{\hbar}{2im_e}\int_{A[\underline{B}]} \underline{dA}\ \underline{e}_x\ \overset{n*}{\phi}_{L,\nu}(\underline{r})\ \overset{m}{\phi}_{L',\nu}(\underline{r}) \\ &= \frac{1}{\hbar} i^{\ell'-\ell-1} \int d\Omega\ Y^*_L(\underline{e})\ (\underline{e}_x\underline{e})\ Y_{L'}(\underline{e}) \ \times \\ &\quad \times \Bigg\{ \frac{\hbar^2}{2m_e}(S^{WS})^3 \left[\overset{n}{\phi}_{\ell,\nu}(r) \frac{d}{dr}\overset{m}{\phi}_{\ell',\nu}(r) - \overset{m}{\phi}_{\ell',\nu}(r) \frac{d}{dr}\overset{n}{\phi}_{\ell,\nu}(r) \right]_{r=S^{WS}} \\ &\qquad (\varepsilon_{\ell',\nu} - \varepsilon_{\ell,\nu}) M^{n,m}_{\ell\ell'} - n M^{n-1,m}_{\ell\ell'} + m M^{n,m-1}_{\ell\ell'} \Bigg\} \quad , \end{aligned} \tag{B.12}$$

with the ASA-integral

$$M^{\alpha,\alpha'}_{\ell\ell'} = \int_0^{S^{WS}} r^2 dr\ \overset{\alpha}{\phi}_{\ell,\nu}(r) r \overset{\alpha'}{\phi}_{\ell',\nu}(r) \quad , \tag{B.13}$$

$\overset{n}{\phi}_{\ell,\nu} \equiv [d^n\phi_{\ell,\nu}/d\varepsilon^n]\big|_{\varepsilon=\varepsilon_\nu}$, and m, n are equal 0 or 1.

Special points for Brillouin zone integrations

Generally, spectral properties, $\widehat{f}(\varepsilon)$, of periodic systems are obtained on integrating over the first Brillouin zone,

$$\widehat{f}(\varepsilon) = \int_{1.\mathrm{BZ}} \frac{d^3\underline{k}}{(2\pi)^3/\Omega}\ f(\underline{k}, \varepsilon) \quad . \tag{B.14}$$

For instance, this problem appears in supercell methods for the calculation of the state density and the spectral conductivity of a given system.

As a numerical problem, one wants to perform the integral (B.14) with the minor amount of $\underline{k}$-points. The most common numerical procedures are the tetrahedron method [Jepsen 71, Blöchl 94] and the special-point scheme [Baldereschi 73, Chadi 73, Monkhorst 76, Rogan 01]. Comparisons between both methods are not performed here, it goes beyond of the scope of this work.

Briefly, the first one determines the irreducible part of the Brillouin zone and divides it into tetrahedra, where the values of the function f are known at the tetrahedron corners $\underline{k}_i$. Thus, the integration for each tetrahedron can be performed analytically after linear interpolation of the function inside the tetrahedron.

The second one is employed in the present work and will be described below. Because of $f(\underline{k}, \varepsilon)$ is a Bloch function it can be expanded as a Fourier series,

$$f(\underline{k}, \varepsilon) = \widehat{f}_0(\varepsilon) + \sum_{m=1}^{\infty} \widehat{f}_m(\varepsilon) A_m(\underline{k}) \quad , \tag{B.15}$$

where (for cubic lattices)

$$A_m(\underline{k}) = \frac{1}{2^{3n}} \sum_{|\underline{t}|=c} e^{i\underline{k}\underline{t}} \qquad \texttt{for} \quad 0 < c < 2^n a \quad , \tag{B.16}$$

with a the lattice constant, $\underline{t}$ the translation vectors, and $n = 1, 2, 3, ...$

Replacing (B.15) into (B.14) one can see that, for any m, the integral of $A_m(\underline{k})$ vanishes and we have $\widehat{f}(\varepsilon) = \widehat{f}_0(\varepsilon)$. However, the true integral can not be performed. Approximately, one can write the integration (B.14) by a weighted sum over special $\underline{k}$-points,

$$\widehat{f}(\varepsilon) \simeq \sum_{\underline{k}} w_{\underline{k}} f(\underline{k}, \varepsilon) \quad . \tag{B.17}$$

On the other hand, the substitution of (B.15), with $M^{(n)}$ as the upper limit of the sum, into (B.17) gives

$$\widehat{f}(\varepsilon) \simeq \sum_{\underline{k}} w_{\underline{k}} \widehat{f}_0(\varepsilon) + \sum_{m=1}^{M^{(n)}} \widehat{f}_m(\varepsilon) \sum_{\underline{k}} w_{\underline{k}} A_m(\underline{k}) \quad . \tag{B.18}$$

If $M^{(n)}$ is high enough, then the coefficients $\widehat{f}_m$ with $m > M^{(n)}$ become negligible. Hence, the special $\underline{k}$ points and their weighting factors, for which the sum over $\underline{k}$ is 1, are chosen to make $\left[\sum_{\underline{k}} w_{\underline{k}} A_m(\underline{k})\right] \to 0$ for all $m \leq M^{(n)}$.

Hence, one searches for the set of vector $\{\underline{k}\}$ for which

$$\sum_{\underline{k}} e^{i\underline{k}\underline{t}} = 0 \qquad \texttt{for} \quad 0 < |\underline{t}| < 2^n a \quad . \tag{B.19}$$

The solution of this problem are the *special* $\underline{k}$ *points*, $\{\underline{k}^{(n)}\}$, given by Chadi and Cohen [Chadi 73]. For the cubic lattice, the sets $\{\underline{k}^{(n)}\}$ with $n = 1, 2, 3, ...$ are written as [Arnold 97] ($\underline{e}_i$ are the unit vectors),

$$\{\underline{k}^{(n)}\} = \left\{ \frac{\pi}{a} \sum_{i=1,3} \frac{b_i^{(n)}}{2^n} \underline{e}_i \right\} \qquad \texttt{with odd} \quad b_i^{(n)} \in (-2^n, 2^n). \tag{B.20}$$

The odd coefficients $b_i^{(n)}$ take all possible combinations which means 2^{3n} vectors.

An additional reduction was given by Chadi and Cohen [Chadi 73]. It is obtained from the restrictions for $A_m(\underline{k})$, see equation (B.18). After employing the crystal symmetry relations one can reduce the set $\{\underline{k}^{(n)}\}$ to a minimal set $\{\underline{K}^{(n)}\}$ and corresponding weighted-factors $w_{\underline{k}}^{(n)}$. They must fulfil the relation

$$\sum_{\underline{k}\in\{\underline{K}^{(n)}\}} w_{\underline{k}}^{(n)} \sum_{|\underline{t}|=c} e^{\imath \underline{k}\underline{t}} = 0 \qquad \texttt{for} \quad 0<c<2^n a \quad . \tag{B.21}$$

For a given n, the number of non-equivalent weighted special $\underline{k}$ points in the irreducible wedge of the cubic Brillouin zone is

$$M^{(n)} = 2^n(2^n+2)(2^n+4)/48 \qquad \texttt{for} \quad n=1,2,3,... \quad . \tag{B.22}$$

The physical meaning of such restrictions is clearly revealed within the Green-function approach to the state density [Arnold 97, Solbrig 00a]: spurious features of

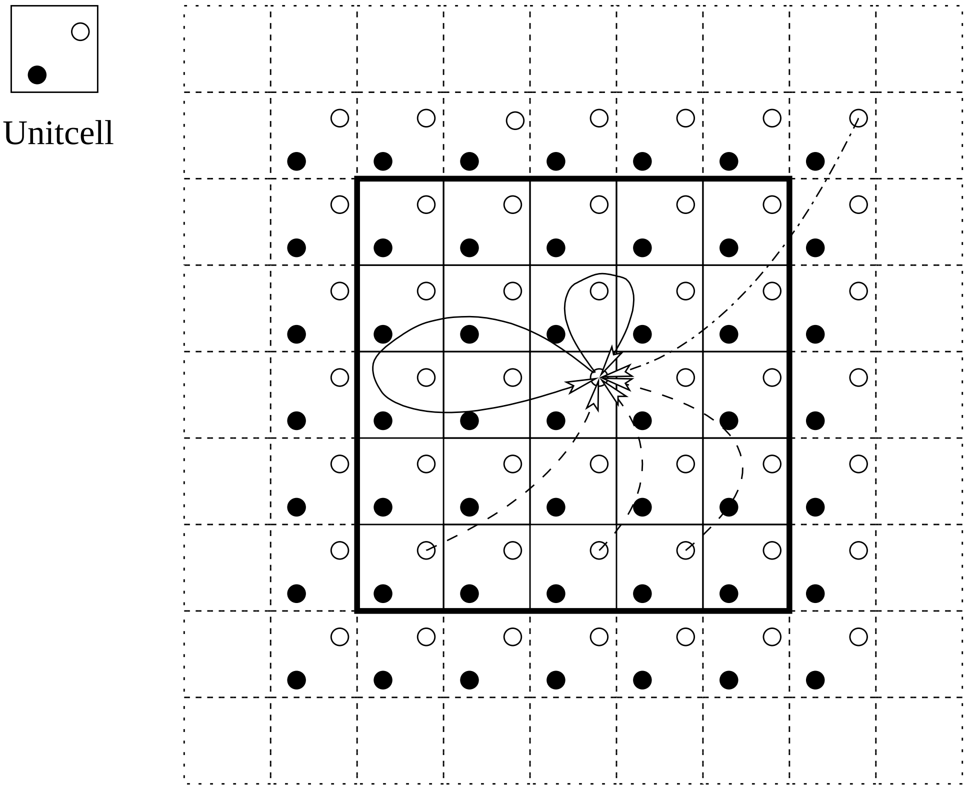

Figure B.1: The Green-function approach to the state density provides us the physical meaning of the special-point scheme [Arnold 97, Solbrig 00a]: spurious features of the local density of states in a central unit-cell are caused by open scattering paths (dot-dashed lines) from beyond a surrounding (cubical) shell of $(\{2(2^n-1)+1\}^3-1)$ unit-cells. The open scattering paths from $\underline{B}+\underline{t}$ to $\underline{B}$, within this shell (dashed lines), are eliminated in the special-point scheme.

the atomic sphere DOS in a central unit-cell are caused by open scattering paths from beyond a surrounding (cubical) shell of $(n = 1, 2, 3, ...)$

$$N_{uc}^{(n)} = \{2(2^n - 1) + 1\}^3 - 1 \tag{B.23}$$

unit-cells, see figure (B.1). The next shells of non-eliminated sources, for the open scattering paths, lie at the distances $2^n a$ (6 sources), $\sqrt{2}\,2^n a$ (12), and $\sqrt{3}\,2^n a$ (8).

B.2 TB-LMTO cluster recursion method

Structure constants in the tight-binding LMTO basis

The screening structure constants, $\underline{\mathcal{S}}^\beta$, can be obtained from the transformation,

$$(\underline{\mathcal{S}}^0)^{-1} - \underline{\beta} \equiv (\underline{\mathcal{S}}^\beta)^{-1} \quad , \tag{B.24}$$

or explicitly (Dyson equation),

$$\mathcal{S}^\beta_{\underline{R}L,\underline{R}'L'} = \mathcal{S}^0_{\underline{R}L,\underline{R}'L'} + \sum_{\underline{R}''L''} \mathcal{S}^\beta_{\underline{R}L,\underline{R}''L''}\ \beta_{\underline{R}''\ell''}\ \mathcal{S}^0_{\underline{R}''L'',\underline{R}'L'} \quad , \tag{B.25}$$

where the canonical structure constants, $\underline{\mathcal{S}}^0$, are given by equation (B.4) and the screening parameters, which are independents of $\underline{R}$, are given in table (5.1). For numerical treatments, the equation (B.24) can be rewritten as

$$\underline{\mathcal{S}}^\beta = \underline{\mathcal{S}}^0(1 - \underline{\beta}S^0)^{-1} = \underline{\beta}^{-1}\{(\underline{\beta}^{-1} - \underline{\mathcal{S}}^0)^{-1} - \underline{\beta}\}\underline{\beta}^{-1} \quad . \tag{B.26}$$

Hence, the evaluation of these screening constants is reduced to the calculation of the inverse of the matrix $(\underline{\beta}^{-1} - \mathcal{S}^0)$ for each site. Because of the screening constants vanish rapidly, the size of the matrix to be inverted is, for *spd* orbitals, $N_{nb} \times 9$, where N_{nb} is the number of the neighbour atoms to be considered. Normally, one takes $N_{nb} \approx 20 - 50$ atoms [Nowak 91].

Another way to obtain the screening structure constants is employing the universal interpolation formula for the off-site $(\underline{R} \neq \underline{R}')$ elements of the structure constants [Sob 88],

$$\mathcal{S}^\beta_{\underline{R}L,\underline{R}'L'} = A^\beta_{\ell\ell'm}\ exp\left\{-\lambda^\beta_{\ell\ell'm}\frac{|\underline{R} - \underline{R}'|}{w}\right\} \quad , \tag{B.27}$$

where w is the average Wigner-Seitz radius, (5.5), and the values of $A_{\ell,\ell'm}$ and $\lambda_{\ell,\ell'm}$ are tabulated in [Andersen 87, Sob 88]. Then, the on-site elements can be calculated from the Dyson equation (B.25) for $\underline{R}' = \underline{R}$. Considering that the on-site canonical structure constant is zero (per definition), the Dyson equation (B.25) for the on-site terms reduces to,

$$\mathcal{S}^\beta_{\underline{R}L,\underline{R}L''} = \sum_{\underline{R}'L'} \mathcal{S}^\beta_{\underline{R}L,\underline{R}'L'}\ \beta_{\underline{R}'\ell'}\ \mathcal{S}^0_{\underline{R}'L',\underline{R}L''} \quad , \tag{B.28}$$

where the off-site elements, $\mathcal{S}^\beta_{\underline{R}L,\underline{R}'L'}$, are taken from (B.27).

Position operator in the TB-LMTO representation

To calculate the electronic diffusivity, employing the recursion procedure, one needs the component μ of the velocity matrix, equation (5.27). A way to do it was presented by Bose [Bose 93]: taking $\mu = x$, the velocity operator is given by $v_x = i[\mathcal{H}, x]/\hbar$ then, the matrix elements of the velocity operator in the TB-LMTO representation ($\underline{\alpha} = \underline{\beta}$) are,

$$(v_x)^{\beta}_{\underline{R}L,\underline{R}'L'} = \frac{i}{\hbar} \sum_{\underline{R}''L''} \left\{ \mathcal{H}^{\beta}_{\underline{R}L,\underline{R}''L''} \; x^{\beta}_{\underline{R}''L'',\underline{R}'L'} - x^{\beta}_{\underline{R}L,\underline{R}''L''} \; \mathcal{H}^{\beta}_{\underline{R}''L'',\underline{R}'L'} \right\} \quad , \tag{B.29}$$

where the matrix elements of the TB-LMTO Hamiltonian are obtained from (5.13). The matrix elements of the position operator, $x^{\beta}_{\underline{R}L,\underline{R}'L'}$, can be written as [Bose 93],

$$\begin{aligned} x^{\beta}_{\underline{R}L,\underline{R}'L'} &= \langle \chi^{\beta}_{\underline{R}L} | x | \chi^{\beta}_{\underline{R}'L'} \rangle \\ &= \frac{1}{2}(x_{\underline{R}L} + x_{\underline{R}'L'}) \mathcal{O}^{\beta}_{\underline{R}L,\underline{R}'L'} + \langle \chi^{\beta}_{\underline{R}L} | \left\{ x - \frac{1}{2}(x_{\underline{R}L} + x_{\underline{R}'L'}) \right\} | \chi^{\beta}_{\underline{R}'L'} \rangle \quad , \end{aligned} \tag{B.30}$$

where $x_{\underline{R}L}$ is the x-coordinate of the atomic nucleus $\underline{R}$ on which the orbital L is centered. The last term in (B.30), known as the dipole term, is neglected assuming that it is small, see [Bose 93] and references therein.

Ignoring the non-orthogonality of the TB-LMTO basis, the overlap matrix is reduced to the unit matrix, $\mathcal{O}^{\beta}_{\underline{R}L,\underline{R}'L'} = \langle \chi^{\beta}_{\underline{R}L} | \chi^{\beta}_{\underline{R}'L'} \rangle \approx 1$. Thus, the velocity matrix is written as (neglecting the dipole term in (B.30)),

$$(v_x)^{\beta}_{\underline{R}L,\underline{R}'L'} \approx \frac{i}{\hbar} \mathcal{H}^{\beta}_{\underline{R}L,\underline{R}'L'} \left\{ x_{\underline{R}'L'} - x_{\underline{R}L} \right\} \quad . \tag{B.31}$$

Bose showed that this approximation can not be successfully applied for liquid transition metals [Bose 93]. However, in the case of the orthogonal LMTO basis ($\underline{\alpha} = \underline{\gamma}$) the overlap is, up to some accuracy, really the unit matrix, and equation (B.31) is the matrix representation of the velocity operator.

Tridiagonalization: the Lanczos procedure

The recursion procedure [Haydock 80] transforms a symmetric (Hermitian) matrix, $\underline{\mathcal{H}}$, into a tridiagonal form, $\underline{\mathcal{T}}$, employing the so-called Lanczos basis, $\{|n\rangle\}$.

The first state $|1\rangle \equiv |\varphi\rangle$ must be chosen. It determines the expected state density projected to $|\varphi\rangle$. In fact, the projected state density, equation (5.21), is calculated from the imaginary part of the Green function $G_{\varphi,\varphi}(\varepsilon + i\zeta) = (\varepsilon + i\zeta - \underline{\mathcal{T}})^{-1}$, which is no more than a continued fraction, equation (5.22).

Then, we construct the second state $|2\rangle$ through

$$\mathcal{H}|1\rangle = a_1|1\rangle + b_1|2\rangle \quad , \tag{B.32}$$

where a_1 is determined applying $\langle 1|$ in (B.32) and imposing orthonormality ($\langle 1|1\rangle = 1, \langle 1|2\rangle = 0$). This yields,

$$a_1 = \langle 1|\mathcal{H}|1\rangle \quad . \tag{B.33}$$

To obtain b_1, the equation (B.32) is rewritten as,

$$b_1|2\rangle = \mathcal{H}|1\rangle - a_1|1\rangle \quad . \tag{B.34}$$

Then, from (B.34) and requiring the normalization of $|2\rangle$ yields,

$$b_1^2 = \langle 1|(\mathcal{H} - a_1\mathcal{I})^\dagger(\mathcal{H} - a_1\mathcal{I})|1\rangle \quad . \tag{B.35}$$

From (B.34), the second state is

$$|2\rangle = \frac{1}{b_1}\Big\{(\mathcal{H} - a_1\mathcal{I})|1\rangle\Big\} \quad . \tag{B.36}$$

Note that following this construction $|2\rangle$ is normalized and orthogonal to $|1\rangle$. The general recurrence relation is given by ($n = 2, 3, 4, ...$),

$$\mathcal{H}|n\rangle = a_n|n\rangle + b_n|n+1\rangle + b_{n-1}|n-1\rangle \quad . \tag{B.37}$$

Then ($n = 2, 3, 4, ...$),

$$\begin{aligned} a_n &= \langle n|\mathcal{H}|n\rangle \\ b_n^2 &= \Big\{\langle n|(\mathcal{H} - a_n\mathcal{I})^\dagger - \langle n-1|b_{n-1}\Big\}\Big\{(\mathcal{H} - a_n\mathcal{I})|n\rangle - b_{n-1}|n-1\rangle\Big\} \\ |n+1\rangle &= \frac{1}{b_n}\Big\{(\mathcal{H} - a_n\mathcal{I})|n\rangle - b_{n-1}|n-1\rangle\Big\} \quad . \end{aligned} \tag{B.38}$$

The state $|n+1\rangle$ is normalized and orthogonal to $|n\rangle$ and $|n-1\rangle$.

Hence, the tridiagonal matrix, $\underline{\mathcal{T}}$, has the following form,

$$\underline{\mathcal{T}} = \begin{pmatrix} a_1 & b_1 & & & & & \\ b_1 & a_2 & b_2 & & & & \\ & b_2 & a_3 & b_3 & & & \\ & & & \ddots & & & \\ & & & b_{n-1} & a_n & b_n & \\ & & & & & \ddots & \\ & & & & & & \ddots \\ & & & & & & \end{pmatrix} \quad . \tag{B.39}$$

Filter technique

The filter method can be employed to obtain the electronic wave function for a specified energy, which is normally the Fermi energy, ε_F. The *filter* is no more than an operator which after applying to an arbitrary initial state, $|\alpha\rangle$, the result is another state. *High quality filters* choose out of the arbitrary initial state the wave functions that are associated to the energy ε: $|\Psi(\varepsilon)\rangle \approx F(\varepsilon)|\alpha\rangle$. The procedure proposed by Stein and Krey [Stein 80] is based on a modified recursion procedure that can be employed directly with the TB-LMTO Hamiltonian.

One wants to express the electronic wave function as a combination of Lanczos states,

$$|\Psi(\varepsilon)\rangle \equiv |\Psi^{opt}(\varepsilon)\rangle + |\Delta\Psi\rangle = \sum_{n=1}^{M} \phi_n |n\rangle + \sum_{n=M+1}^{N} \phi'_n |n\rangle \quad , \tag{B.40}$$

where $|\Psi^{opt}(\varepsilon)\rangle$ and $|\Delta\Psi\rangle$ are the first, respectively, the second summation, and N is the size of the Hamiltonian $\underline{\mathcal{H}}$.

An effective procedure should requires that $|\Delta\Psi\rangle \to |0\rangle$. Thus $|\Psi^{opt}(\varepsilon)\rangle$ can be considered as a good approximation for the wave function. That means, only the coefficients ϕ_n for which $n \leq M \ll N$ will be required, i.e. $(\underline{\mathcal{H}} - \varepsilon\underline{\mathcal{I}})|\Psi^{opt}(\varepsilon)\rangle \to |0\rangle$ for all $n \leq M$, see equation (B.42). Furthermore, the additional condition $\sum_{n=M+1}^{N} |\phi'_n|^2 \ll 1$ must be fulfilled. The extreme case should be given when $M = 1$, that means, $|1\rangle = |\Psi(\varepsilon)\rangle$ (the exact wave function) and $\phi_1 = 1$ (normalization). In this case all $\phi'_n = 0$ for all $n \neq 1$.

Explicitly, the procedure works as follow (for $\varepsilon = \varepsilon_F$):

1) When there is no idea of the properties of the wave function, one can take a *random*[1] state,

$$|\alpha\rangle \approx \sum_{n=1}^{M} \alpha_n^{(1)} |n\rangle \quad , \tag{B.41}$$

as starting state of the recursion algorithm, where $\alpha_n^{(1)}$ are uniformly distributed random numbers between [-1,1]. Another possible election is $\alpha_n^{(1)} = exp(i\nu_n)$ with ν_n uniformly distributed random numbers between $[0, 2\pi)$. Both elections yield similar results. Then, this initial state, $|\alpha\rangle$, must be normalized.

2) Employing the conditions of orthogonality of the Lanczos states, $\langle n|n'\rangle = \delta_{nn'}$, and the condition that

$$|\delta\rangle \equiv (\underline{\mathcal{H}} - \varepsilon_F\underline{\mathcal{I}})|\alpha\rangle = |0\rangle \quad , \tag{B.42}$$

for all $n \leq M$, one gets the new coefficients, $\alpha_n^{(2)}$. In general, for the step (i), the coefficients are determined from equation (B.42). The result is

$$\begin{aligned} \alpha_1^{(i)} &= 1 \\ \alpha_2^{(i)} &= (\varepsilon_F - a_1)\alpha_1/b_2 \\ \alpha_n^{(i)} &= (-b_{n-1}\alpha_{n-2} + (\varepsilon_F - a_{n-1})\alpha_{n-1})/b_n \qquad \texttt{for} \quad 3 \leq n \leq M \quad , \end{aligned} \tag{B.43}$$

---

[1] This *random* state is a weighted combination of Lanczos states, $|n\rangle$, correspondingly a weighted combination of the TB-LMTO local orbitals, see equation (5.25). The weights are here the $\alpha_n^{(1)}$ coefficients, see equation (B.41).

where the coefficients a_n and b_n are given by the normal recursion procedure, equation (B.38).

3) The new set of coefficients, $\{\alpha_n^{(i)}\}$, are used to build the new wave function in the same way as equation (B.41). Then, M is replaced by $M-1$. This is because one hopes that the new wave function is more in agreement with the correct wave function (see the discussion above of the extrem case for $M=1$). Thus, at the end, one can expect that $|1^{(M)}(\varepsilon_F)\rangle = |\Psi^{opt}(\varepsilon_F)\rangle \approx |\Psi(\varepsilon_F)\rangle$.

4) Finally, the steps 2) and 3) are repeated until the wave function is filtered into the energy ε_F.

The wave function is *filtered* at the energy ε_F after employing equation (B.43) with ε_F. The use of other energy gives only a wave function filtered at that energy. Hence, the filtered wave function after M iterations can be written as (in vectorial form),

$$|\Psi^{opt}(\varepsilon_F)\rangle = |1^{(M)}(\varepsilon_F)\rangle = (c_{\underline{R}_1 L_1}, c_{\underline{R}_2 L_2}, \ldots, c_{\underline{R}_N L_N})^\dagger \qquad \text{(B.44)}$$

where $c_{\underline{R}L}$ are the coefficients of the wavefunction in the TB-LMTO basis. They are vectors of length 9 (for $1s, 3p, 5d$ orbitals), $c_{\underline{R}L} = (c_{\underline{R}s}, c_{\underline{R}p_x}, c_{\underline{R}p_y} \ldots)^\dagger$.

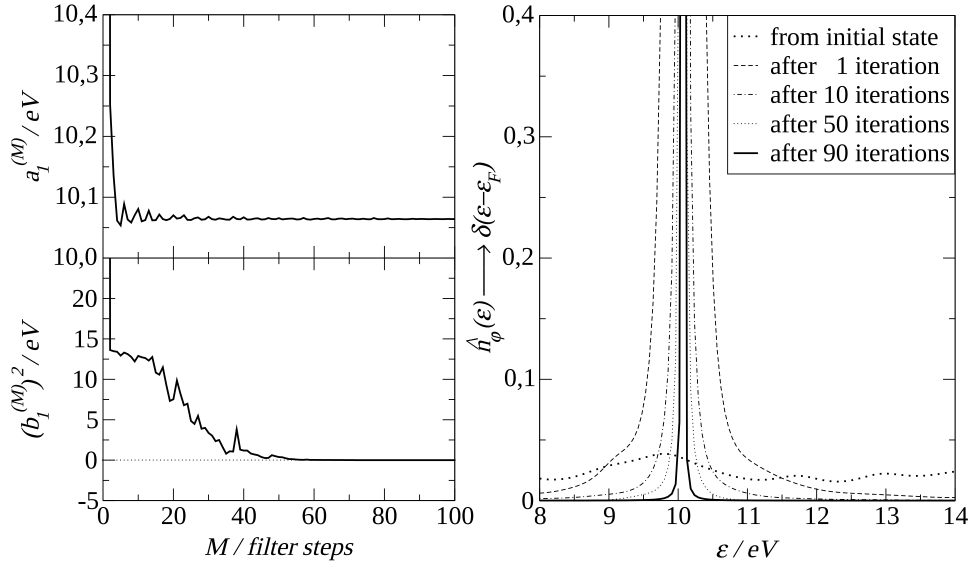

Figure B.2: Testing the filtered wave function. As expected from equations (B.45), (B.46), and (B.47), the coefficient $a_1^{(M)} \to \varepsilon_F$, $(b_1^{(M)})^2 \to 0$, and the state density projected onto the filtered wave function ($|\varphi\rangle = |\Psi(\varepsilon_F)\rangle$) goes to $\delta(\varepsilon - \varepsilon_F)$. As seen, in this case the wave function was filtered at the Fermi energy.

The *good* convergence of the filter technique can be tested assuring that,

$$\langle \Psi^{opt}(\varepsilon_F)|\underline{\mathcal{H}}|\Psi^{opt}(\varepsilon_F)\rangle = a_1^{(M)} \approx \varepsilon_F \quad , \qquad \text{(B.45)}$$

or

$$\langle \Psi^{opt}(\varepsilon_F)|(\underline{\mathcal{H}} - a_1\underline{\mathcal{I}})^\dagger(\underline{\mathcal{H}} - a_1\underline{\mathcal{I}})|\Psi^{opt}(\varepsilon_F)\rangle = (b_1^{(M)})^2 \approx 0 \quad . \qquad \text{(B.46)}$$

In the filter procedure the values $a_1^{(i)}$ and $b_1^{(i)}$ can be interpreted as the fluctuations around the chosen energy and the standard deviations from it at the step (i), respectively. Then, the energy window $\Delta\varepsilon$ around ε_F (the energy at which the wave function is filtered) is $2b_1^{(i)}$. That means, in the ideal case the density of states projected onto $|\varphi\rangle = |\Psi^{opt}(\varepsilon_F)\rangle$ is (see equation (5.21)),

$$\widehat{n}_\varphi(\varepsilon) = -\lim_{\zeta\to 0}\big\{(1/\pi)\ \mathrm{Im}\ G_{\varphi,\varphi}(\varepsilon + i\zeta)\big\} = \delta(\varepsilon - \varepsilon_F) \quad . \tag{B.47}$$

However, for numerical calculations one employs a fixed finite $\zeta \neq 0$. This gives, employing (5.22), a Lorentz function, centered at $a_1^{(M)} \approx \varepsilon_F$, width 2ζ, in the projected state density (B.47) (remember that after the final step in the filter technique all coefficients, except $a_1^{(M)}$, must go to zero). Futhermore, due to the small but non-zero $b_1^{(M)}$, the shape and width of this Lorentzian should be modified.

Figure (B.2) shows a *convergence test* of a wave function filtered at the Fermi energy. As expected from equations (B.45), (B.46), and (B.47), the coefficient $a_1^{(M)} \to \varepsilon_F$, $(b_1^{(M)})^2 \to 0$, and the state density projected onto the filtered wave function ($|\varphi\rangle = |\Psi(\varepsilon_F)\rangle$) goes to $\delta(\varepsilon - \varepsilon_F)$. These tests show that such wave function has reached convergence.

Appendix C

3D Penrose tiling approximant and its chemical decoration

C.1 Rational approximants

Approximants of the quasicrystal (in this case the icosahedral Penrose tiling) are obtained after changing the irrational value of the slope τ^*, also called *golden mean*, by a rational one in the cut-and-project method (see chapter 2). This change modify the acceptance domain in $P^{\perp}(\tau^* \to \tau_n^*)$, equation (2.4), and hence the atomic positions in the physical space. These new atomic positions form a periodic structure, also called *rational approximant*.

The approximation of τ^* is given as a series of 1/1, 2/1, 3/2, 5/3, ... This series is given as $\tau_n^* \equiv F_{n+1}/F_n$, where $F_{n+1} = F_n + F_{n-1}$, with $F_0 = F_1 = 1$, and F_n is called the Fibonacci number. In the limit $n \to \infty$, $\tau_n^* \to \tau^* = (\sqrt{5}+1)/2$.

These approximant structures present the following properties: i) approximants are compounds of a commensurable structure, ii) when τ_n^* is very close to τ both, the quasiperiodic and the periodic, structures are very similar (especially the local order remain the same), and iii) approximants can also be obtained by interchanging

Table C.1: Structural parameters of rational Penrose tiling approximants. N_i is the number of atoms in the unit cell obtained employing the cut-and-project method (see chapter 2) and N_a is the number of atoms in the unit cell with realistic distances.

Approximant structure τ_n^*	lattice constant Å	N_i	N_a
1/1	7.5564	32	25
2/1	12.2266	136	98
3/2	19.7830	576	434
5/3	32.0095	2440	1825
8/5	51.7925	10319	

atomic sites (phason flips) in the quasicrystalline structure.

Table (C.1) present the structure parameters of the five low order cubic approximants of the icosahedral Penrose tiling. N_i is the number of atoms obtained employing the cut-and-project method.

Really, the clusters that we obtain possess pair of atoms with unphysically short distances. These short distances do not permit calculations of the electronic properties in an *ab-initio* way. Therefore, to perform these calculations we take out those *unphysical* atomic positions (N_a in table (C.1) is the number of atoms without unphysically short distances). Thus, the structures presented here can be considered as *test-structures*, because there are different manners to eliminate these short distances (e.g. Monte-Carlo or molecular dynamic relaxations).

C.2 Chemical decoration and spectral results

The electronic properties of the approximants depend of the chemical decoration. To prove this, we decorate the two low order rational approximants of the icosahedral Penrose tiling in three different ways. The vertexes of the tiling are decorated with Al atoms or Fe atoms only. The third decoration, Al-rich-Fe, is a more realistic two component system (the Fe atoms are placed on the icosahedron centre).

Figure (C.1) shows the state density and spectral resistivity of low order approximants for three different decorations (as explained above). One-component dec-

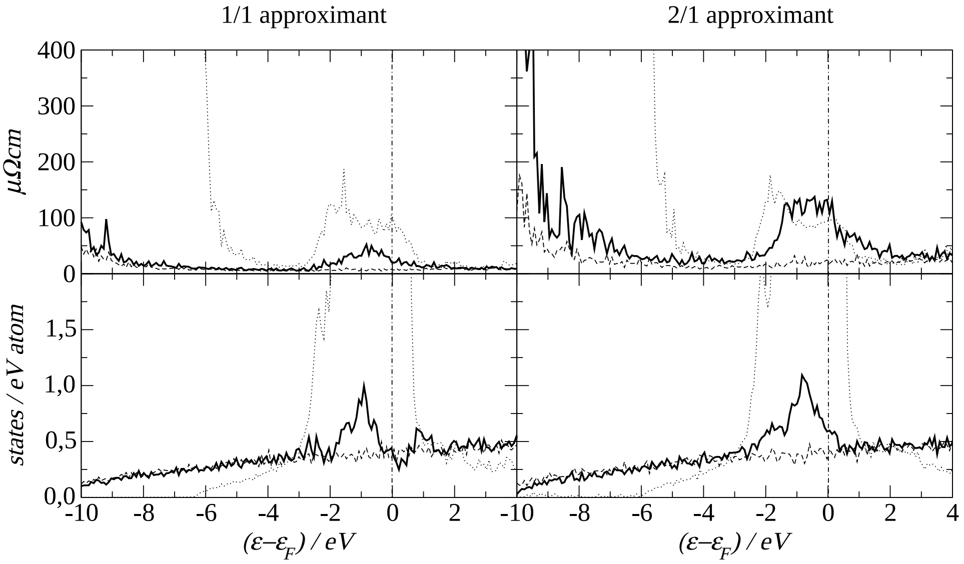

Figure C.1: Spectral properties of the 1/1 and 2/1 approximants of the icosahedral Penrose tiling. The tiling-vertexes are decorated with Al atoms (dashed), Fe atoms (dots), or Al/Fe atoms (solid), see text for details. The spectral resistivity (top) and state density (bottom) are calculated employing the LMTO-ASA supercell method and the Kubo-Greenwood formula (see chapter 5).

orations (Al or Fe atoms) cannot explain the trends found experimentally for the electronic properties. In fact, for the aluminium (weak scatterer) decorated approximants, the resistivity is very low, and for the iron (strong scatterer) decorated approximants, the state density is very high.

On the other hand, the two-component model provides state densities which correspond to experiments (see for instance [Stadnik 99]). The pseudogap around the Fermi energy is sensitive to the chemical decoration. For the 2/1 approximant, the resistivity arise values of $\sim 150\ \mu\Omega cm$ which is three times higher than the resistivity of the 1/1 approximant.

One can also see that the amount of states alone cannot explain the high resistivities. The kind of the states (expressed in the electronic diffusivity, or participation ratios) is also important. For example, the aluminium and Al-rich-Fe decorated models have (nearly) the same state density but very different resistivities around the Fermi energy.

Finally, as expected, the resistivity increases after increasing the order of the approximant. If the correct chemical decoration is given then, this increase is faster. Therefore both, structure and chemical decoration, are important to describe the electronic properties of approximants/quasicrystals.

Appendix D

Structural parameters of low order approximants

The employment of realistic approximant models, which provide the right structure and chemical decoration, are important to explain the *anomalous* properties of approximants (quasicrystals), as dicussed in chapters 6 and 7. Hence, approximant models obtained from different experimental works in structure refinement were employed in the present work.

The crystallographic data of the i-Al-Cu-Fe approximant is given in table (6.1), details of the structure are given in chapter 6. The γ-Al-Cu-Ru approximant is based on a simple cubic arrangement of dodecahedral atom clusters. There are 248 atoms per unit cell, the crystallographic data is given in table (D.1). The α-Al-Pd-Mn-(Si) approximant is based on a Bergman cluster with five atomic shells. There are 123 atoms per unit cell, the crystallographic data is given in table (D.2). The α-Al-Mn-(Si) approximant is based on a bcc arrangement of MacKay icosahedron atom clusters. The Elser-Henley model [Elser 85] is formed by 114 Al, 24 Mn, and 14 voids (the crystallographic data is given in table (D.3)). Here, the voids are eliminated by Monte-Carlo relaxation of the Al glue at 3000 K (Morse potentials [Mihalkovič 96]). In the present work, we will not distinguish Si atoms from Al atoms.

It is worth noting that some positions of several approximants are occupied/decorated with probabilities less than one. However, *ab-initio* electronic structure calculations require completely determined atomic positions. Hence, when the occupation probability of an atomic site is less than 0.5, the atom is taken out. In this sense, the approximants used here are not *completely* equivalent than the proposed in the experimental works: the differences are considered negligible.

Table D.1: Structural parameters of the γ-Al-Cu-Ru approximant of the i-Al-Cu-Ru [Sugiyama 98b]: Lattice constant $a = b = c = 15.38\text{Å}$, and Space Group Fm3. Atom types, symmetry sites, and coordinates (x,y,z) in (a,b,c)-units are presented.

Atom	Site	x/a	y/b	z/c	Atom	Site	x/a	y/b	z/c
Cu(1)	4a	0.000	0.000	0.000	Cu(2)	32f	0.095	0.095	0.095
Ru(1)	4b	0.500	0.500	0.500	Ru(2)	48h	0.000	0.853	0.253
Al(1)	8c	0.250	0.250	0.250	Al(3)	96i	0.096	0.251	0.342
Al(2)	24e	0.187	0.000	0.000	Al(4)	32f	0.404	0.404	0.404

Table D.2: Structure parameters of the α-Al-Pd-Mn-(Si) approximant of the i-Al-Pd-Mn [Sugiyama 98a]: Lattice constant $a = b = c = 12.281\text{Å}$, and Space Group Pm3. Atom types, symmetry sites, and coordinates (x,y,z) in (a,b,c)-units are presented. From the 6 symmetric positions of Al(9), we take into account only the first three symmetric positions, in order to avoid unphysically short distances.

Atom	Site	x/a	y/b	z/c	Atom	Site	x/a	y/b	z/c
Pd(1)	1b	0.500	0.500	0.500	Al(3)	8i	0.191	0.191	0.191
Pd(2)	6f	0.196	0.000	0.500	Al(4)	12k	0.500	0.391	0.307
Pd(3)	8i	0.308	0.308	0.308	Al(5)	12k	0.500	0.180	0.228
Mn(1)	6g	0.321	0.500	0.000	Al(6)	12j	0.000	0.308	0.123
Mn(2)	12j	0.000	0.107	0.175	Al(7)	12j	0.000	0.191	0.349
Al(1)	1a	0.000	0.000	0.000	Al(8)	24l	0.332	0.114	0.379
Al(2)	6h	0.104	0.500	0.500	Al(9)	6g	0.052	0.500	0.000

Table D.3: Structure parameters of the α-Al-Mn-(Si) approximant of the i-Al-Mn-Si [Villars 91]: Lattice constant $a = b = c = 12.68\text{Å}$, and Space Group Pm3. Atom types, symmetry sites, and coordinates (x,y,z) in (a,b,c)-units are presented.

Atom	Site	x/a	y/b	z/c	Atom	Site	x/a	y/b	z/c
Al(1)	6e	0.364	0.000	0.000	Al(6)	12k	0.500	0.334	0.399
Al(2)	6f	0.290	0.000	0.500	Al(7)	12k	0.500	0.121	0.118
Al(3)	6h	0.122	0.500	0.500	Mn(2)	12k	0.500	0.180	0.309
Al(4)	12j	0.000	0.164	0.100	Al(8)	24l	0.119	0.190	0.298
Al(5)	12j	0.000	0.332	0.404	Al(9)	24l	0.390	0.313	0.196
Mn(1)	12j	0.000	0.327	0.201					

Bibliography

[Ahlgren 97a] M. Ahlgren, C. Gignoux, M. Rodman, C. Berger and Ö . Rapp, Phys. Rev. B, Vol. **55**, page R–11915, 1997.

[Ahlgren 97b] M. Ahlgren, M. Rodman, C. Gignoux, C. Berger and Ö . Rapp, Mater. Sci. Eng. A, Vol. **226-228**, page 981, 1997.

[Andersen 75] O. K. Andersen, Phys. Rev. B, Vol. **12**, page 3060, 1975.

[Andersen 84a] O. K. Andersen, in P. Phariseau and W. M. Temmerman, The electronic structure of complex systems. Plenum Publishing Corporation, New York, 1984.

[Andersen 84b] O. K. Andersen and O. Jepsen, Phys. Rev. Lett., Vol. **53**, page 2571, 1984.

[Andersen 85] O. K. Andersen, O. Jepson and D. Glotzel, in F. Banani, F. Fumi and M. P. Tosi, Highlights of Condensed Matter Theory. North-Holland, Amsterdam, 1985.

[Andersen 87] O. K. Andersen, D. Jepsen and M. Šob. Electronic band structure and its applications, page 1. Springer-Verlag, Berlin, 1987.

[Anderson 58] P. W. Anderson, Phys. Rev., Vol. **109**, N. 5, page 1492, 1958.

[Arnold 97] R. Arnold, *Stabilisierendes Pseudogap und Streukonzept in nichtkristallinenMaterialien.* PhD thesis, Technische Universität Chemnitz, 1997.

[Asano 80] S. Asano and F. Yonezawa, J. Phys. F: Metal Phys., Vol. **10**, page 75, 1980.

[Ashcroft 76] N.W. Ashcroft and N.D. Mermin, Solid state physics. Saunders College Publishing, 1976.

[Baldereschi 73] A. Baldereschi, Phys. Rev. B, Vol. **7**, page 5212, 1973.

[Bancel 86] P. A. Bancel and P. A. Heiney, Phys. Rev. B, Vol. **33**, page 7917, 1986.

[Barth 72] U. von Barth and L. Hedin, J. Phys. C, Vol. **5**, page 1629, 1972.

[Basov 94a] D. N. Basov, F. S. Pierce, P. Volkov, S. J. Poon and T. Timusk, Phys. Rev. Lett., Vol. **73**, page 1865, 1994.

[Basov 94b] D. N. Basov, T. Timusk, F. Barakat, J. Greedan and B. Grushko, Phys. Rev. Lett., Vol. **72**, page 1937, 1994.

[Baym 64] G. Baym, Phys. Rev., Vol. **135**, page 1691, 1964.

[Beer 84] N. Beer and D. G. Pettifor, . in P. Phariseau and W. H. Temmerman, The Electronic Structure of Complex Systems, Plenum Press, page 769. New York, 1984.

[Belin 91] E. Belin and A. Traverse, J. Phys.: Cond. Matter, Vol. **3**, page 2157, 1991.

[Belin 92] E. Belin, Z. Dankhazi, A. Sadoc, Y. Calvayrac, T. Klein and J. M. Dubois, J. Phys.: Cond. Matter, Vol. **4**, page 4459, 1992.

[Bellissard 95] J. Bellissard and H. Schulz-Baldes, *Anomalous transport and quasicrystals.* in C. Janot and R. Mosseri, Proceedings of the 5th International Conference on Quasicrystals, World Scientific, page 439. Avignon, 1995.

[Bellissard 00] J. Bellissard, Mater. Sci. Eng. A, Vol. **294-296**, page 450, 2000.

[Berger 94] C. Berger, in F. Hippert and D. Gratias, Lectures on quasicrystals, page 463. Editions de Physique, Les Ulis-France, 1994.

[Berger 95] C. Berger, D. Mayou and F. Cyrot-Lackmann, *Anti metallic properties of quasicrystals.* in C. Janot and R. Mosseri, Proceedings of the 5th International Conference on Quasicrystals, World Scientific, page 423. Avignon, 1995.

[Bianchi 97] A. D. Bianchi, F. Bommeli, M. A. Chernikov, U. Gubler, L. Degiorgi and H. R. Ott, Phys. Rev. B, Vol. **55**, page 5730, 1997.

[Biggs 90] B. D. Biggs, S. J. Poon and N.R. Munirathnam, Phys. Rev. Lett., Vol. **65**, page 2700, 1990.

[Biggs 91] B. D. Biggs, Y. Li and S. J. Poon, Phys. Rev. B, Vol. **43**, page 8747, 1991.

[Bilušić 01] A. Bilušić, D. Pavuna and A. Smontara, Vacuum, Vol. **61**, page 345, 2001.

[Blöchl 94] P. E. Blöchl, O. Jepsen and O. K. Andersen, Phys. Rev. B, Vol. **49**, page 16223, 1994.

[Bose 88] S. K. Bose, S. S. Jaswal, O. K. Andersen and J. Hafner, Phys. Rev. B, Vol. **37**, page 9955, 1988.

[Bose 93] S. K. Bose, O. Jepsen and O. K. Andersen, Phys. Rev. B, Vol. **48**, N. 7, page 4265, 1993.

[Boudard 99] M. Boudard and M. de Boissieu. Physical Properties of Quasicrystals, page 91. Springer-Verlag, Berlin, 1999.

[Burkov 92] S. E. Burkov, T. Timusk and N. W. Ashcroft, J. Phys.: Cond. Matter, Vol. **4**, page 9447, 1992.

[Bush 74] G. Bush and J.J. Güntherodt, Solid State Phys., Vol. **29**, page 335, 1974.

[Butler 85] W. H. Butler, Phys. Rev. B, Vol. **31**, N. 6, page 3260, 1985.

[Büttiker 85] M. Büttiker, Y. Imry, R. Landauer and S. Pinhas, Phys. Rev. B, Vol. **31**, page 6207, 1985.

[Callen 85] H. B. Callen, Thermodynamics and an introduction to thermostatistics. John Wiley & Sons, New York, 1985.

[Carlsson 95] A. E. Carlsson and P. J. Meschter. Intermetallic compounds, page 55. John Willey and Sons, Chichester, 1995.

[Chadi 73] D. J. Chadi and M. L. Cohen, Phys. Rev. B, Vol. **8**, N. 12, page 5747, 1973.

[Chester 61] G. V. Chester and A. Thellung, Proc. Phys. Soc., Vol. **77**, page 1005, 1961.

[Cockayne 93] Eric Cockayne, Rob Phillips, X. B. Kan, S. C. Moss, J. L. Robertson, T. Ishimasa and M. Mori, J. Non-Cryst. Solids, Vol. **153-154**, page 140, 1993.

[Cusack 87] N. E. Cusack, The physics of structurally disordered matter. Adam Hilger, Bristol and Philadelphia, 1987.

[Davydov 98] D. N. Davydov, D. Mayou, C. Berger and A. G. M. Jansen, Int. J. Modern Phys. B, Vol. **12**, page 503, 1998.

[de Boissieu 94] M. de Boissieu, P. Guyot and M. Audier, in F. Hippert and D. Gratias, Lectures on quasicrystals, page 1. Editions de Physique, Les Ulis-France, 1994.

[de Groot 52] S. R. de Groot and P. Mazur, Thermodynamics of irreversible processes. North-Holland, Amsterdam, 1952.

[Delahaye 98] J. Delahaye, J. P. Brison and C. Berger, Phys. Rev. Lett., Vol. **81**, page 4204, 1998.

[Delahaye 00] J. Delahaye, J. P. Brison, C. Berger and G. Fourcaudot, Mater. Sci. Eng. A, Vol. **294-296**, page 580–583, 2000.

[Dubois 92] J. M. Dubois, S. S. Kang, P. Archambault and B. Colleret, Journ. Mat. Res., Vol. **8-1**, page 38, 1992.

[Elser 85] V. Elser and C. L. Henley, Phys. Rev. Lett., Vol. **55**, page 2883, 1985.

[Elser 86] V. Elser, Acta Cryst. A, Vol. **42**, page 36, 1986.

[Enderby 90] J. E. Enderby and A. C. Barnes, Rep. Progr. in Physics, Vol. **53**, page 85, 1990.

[Enderby 94] J. E. Enderby and A. C. Barnes, Phys. Rev. B, Vol. **49**, page 5062, 1994.

[Escudero 99] R. Escudero, J. C. Lasjaunias, Y. Calvayrac and M. Boudard, J. Phys.: Cond. Matter, Vol. **11**, page 383, 1999.

[Faber 65] T. E. Faber and J. M. Ziman, Phil.Mag., Vol. **11**, page 153, 1965.

[Friedel 88] J. Friedel, Helv. Physica Acta, Vol. **61**, page 538, 1988.

[Friedel 92] J. Friedel, Philos. Mag. B, Vol. **65**, page 1125, 1992.

[Frydmann 95] A. Frydmann and Z. Ovadyahu, Solid State Commun., Vol. **94**, page 745, 1995.

[Fujiwara 88] T. Fujiwara, M. Arai, T. Tokihiro and M. Kohmoto, Phys. Rev. B, Vol. **37**, page 2797, 1988.

[Fujiwara 89] T. Fujiwara, Phys. Rev. B, Vol. **40**, page 942, 1989.

[Fujiwara 91] T. Fujiwara and T. Yokokawa, Phys. Rev. Lett., Vol. **66**, N. 3, page 333, 1991.

[Fujiwara 93a] T. Fujiwara, J. Non-Cryst. Solids, Vol. **156-158**, page 865, 1993.

[Fujiwara 93b] T. Fujiwara, S. Yamamoto and G. Trambly de Laissardiére, Phys. Rev. Lett., Vol. **71**, N. 25, page 4166, 1993.

[Fujiwara 96] T. Fujiwara, T. Mitsui and S. Yamamoto, Phys. Rev. B, Vol. **53**, N. 6, page R2910, 1996.

[Ghibaudo 87] G. Ghibaudo, J. Phys. C: Solid State Phys., Vol. **20**, page L769, 1987.

[Gignoux 97] C. Gignoux, C. Berger, G. Fourcaudot, J.C. Grajeco and H. Rakoto, Europhys. Lett., Vol. **39**, N. 2, page 171, 1997.

[Gratias 93] D. Gratias, Y. Calvayrac, Q. Devaud-Rzepski, F. Faudot, M. Hermelin, A. Quivy and P. Bancel, J. Non-Cryst. Solids, Vol. **153-154**, page 482, 1993.

[Greenwood 58] D. A. Greenwood, Proc. Phys. Soc., Vol. **71**, page 585, 1958.

[Grest 83] G. S. Grest and P. A. Lee, Phys. Rev. Lett., Vol. **50**, page 693, 1983.

[Guo 96] Q. Guo and S. J. Poon, Phys. Rev. B, Vol. **54**, page 12793, 1996.

[Guohong 99] Li Guohong, He Haifeng, Wang Yunping, Lu Li, Li Shanlin, Jin Xiunian and Zshang Dianlin, Phys. Rev. Lett., Vol. **82**, N. 6, page 1229, 1999.

[Haberkern 93] R. Haberkern, G. Fritsch and M. Härting, Appl. Phys. A, Vol. **57**, page 431, 1993.

[Haberkern 95] R. Haberkern and G. Fritsch, *Semi-metallic behaviour of Al-Cu-Fe quasicrystals.* in C. Janot and R. Mosseri, Proceedings of the 5th International Conference on Quasicrystals, World Scientific, page 460. Avignon, 1995.

[Haberkern 00a] R. Haberkern, K. Khedhri, C. Madel and P. Häussler, Mater. Sci. Eng. A, Vol. **294-296**, page 475–480, 2000.

[Haberkern 00b] R. Haberkern, J. Barzola-Quiquia, C. Madel and P. Häussler, *Quasicrystalline films and their amorphous precursors.* Proceedings MRS-2000, in press.

[Haerle 98] R. Haerle and P. Kramer, Phys. Rev. B, Vol. **58**, N. 2, page 716, 1998.

[Hafner 92] J. Hafner and M. Krajčí, Phys. Rev. Lett., Vol. **68**, N. 15, page 2321, 1992.

[Hafner 93] J. Hafner and M. Krajčí, Phys. Rev. B, Vol. **47**, page 11795, 1993.

[Häussler 92] P. Häussler, Phys. Rep., Vol. **222**, page 65, 1992.

[Haydock 80] R. Haydock, V. Heine, M. L. Kelly and D. W. Bullett, Sol. State Phys., Vol. **35**, 1980.

[Hobbs 95] D. Hobbs, E. Piparo, Girlanda R. and M. Monaca, J. Phys.: Cond. Matter, Vol. **7**, page 2541, 1995.

[Hohenberg 64] P. Hohenberg and Kohn W., Phys. Rev., Vol. **136**, page B 864, 1964.

[Homes 91] C. C. Homes, T. Timusk and X. Wu, Phys. Rev. Lett., Vol. **67**, page 2694, 1991.

[Houari 00] A. Houari, M. Mebrouki, A.F.R. Dib and F. Ould-Kaddour, Physica B, Vol. **291**, page 387, 2000.

[Hume-Rothery 26] W. Hume-Rothery, J. Inst. Met., Vol. **35**, page 295, 1926.

[Itoh 92] M. Itoh, Phys. Rev. B, Vol. **45**, page 4241, 1992.

[Janot 94] C. Janot and M. de Boissieu, Phys. Rev. Lett., Vol. **72**, N. 11, page 1674, 1994.

[Janot 96] C. Janot, Phys. Rev. B, Vol. **53**, N. 1, page 181, 1996.

[Janot 97] C. Janot, J. Phys.: Cond. Matter, Vol. **9**, page 1493, 1997.

[Jepsen 71] O. Jepsen and O. K. Andersen, Solid State Commun., Vol. **9**, page 1763, 1971.

[Jones 89] R. O. Jones and O. Gunnarsson, Rev. Mod. Phys., Vol. **61**, page 689, 1989.

[Kahnt 94] R. Kahnt, *Transport in topologisch ungeordneten, stark streuenden Systemen*. PhD thesis, Technische Universit"at Chemnitz-Zwickau, 1994.

[Kahnt 95] R. Kahnt, J. Phys.: Cond. Matter, Vol. **7**, page 1543, 1995.

[Kalugin 85] P. A. Kalugin, A. Y. Kitaev and L. S. Levitov, JETP Lett., Vol. **41**, page 145, 1985.

[Katz 85] A. Katz and M. Duneau, Phys. Rev. Lett., Vol. **54**, page 2688, 1985.

[Katz 86] A. Katz and M. Duneau, J. de Physique, Vol. **47**, page 181, 1986.

[Klein 91] T. Klein, C. Berger, D. Mayou and F. Cyrot-Lackmann, Phys. Rev. Lett., Vol. **66**, N. 22, page 2907, 1991.

[Klein 92] T. Klein, H. Rakoto, C. Berger, G. Fourcaudot and F. Cyrot-Lackmann, Phys. Rev. B, Vol. **45**, page 2046, 1992.

[Kohmoto 83] M. Kohmoto, L. P. Kadanoff and C. Tang, Phys. Rev. Lett., Vol. **50**, page 1870, 1983.

[Kohmoto 86] M. Kohmoto, Phys. Rev. B, Vol. **34**, page 5043, 1986.

[Kohmoto 87] M. Kohmoto, B. Sutherland and C. Tang, Phys. Rev. B, Vol. **35**, page 1020, 1987.

[Kohn 65] W. Kohn and L. J. Sham, Phys. Rev., Vol. **140**, page A 1133, 1965.

[Kortan 93] A. R. Kortan, F. A. Thiel, N. Kopylov and H. S. Chen, J. Cryst. Growth, Vol. **128**, page 1086, 1993.

[Koumoto 97] K. Koumoto, W. S. Seo and S. Ozawa, Appl. Phys. Lett., Vol. **71**, page 1475, 1997.

[Krajčí 95] M. Krajčí, M. Windisch, J. Hafner, G. Kresse and M. Mihalkovič, Phys. Rev. B, Vol. **51**, page 17355, 1995.

[Krajčí 97] M. Krajčí, J. Hafner and M. Mihalkovič, Phys. Rev. B, Vol. **56**, page 3072, 1997.

[Krajčí 98] M. Krajčí and J. Hafner, Phys. Rev. B, Vol. **58**, N. 9, page 5378, 1998.

[Krajčí 99] M. Krajčí and J. Hafner, Phys. Rev. B, Vol. **59**, N. 13, page 8347, 1999.

[Krajčí 01] M. Krajčí and J. Hafner, J. Phys.: Cond. Matter, Vol. **13**, page 3817, 2001.

[Kubo 57] R. Kubo, J. Phys. Soc. Jap., Vol. **12**, N. 6, page 570, 1957.

[Lalla 95] N. P. Lalla, R. S. Tiwari and O. N. Srivastava, J. Phys.: Cond. Matter, Vol. **7**, page 2409, 1995.

[Lanczos 50] C. Lanczos, J. Res. Natl. Bur. Stand. Sec. B., Vol. **45**, page 255, 1950.

[Lauinger 95] C. Lauinger and F. Baumann, J. Phys.: Cond. Matter, Vol. **7**, page 1305, 1995.

[Lenoir 98] B. Lenoir, A. Dauscher, M. Cassart, Yu. I. Ravich and H. Scherrer, J. Phys. Chem. Solids, Vol. **59**, page 129, 1998.

[Lin 96] C.R. Lin, S. L. Chou and S.T. Lin, J. Phys.: Cond. Matter, Vol. **8**, page L725, 1996.

[Lindqvist 93] P. Lindqvist, C. Berger, T. Klein, P. Lanco and F. Cyrot-Lackmann, Phys. Rev. B, Vol. **48**, N. 1, page 630, 1993.

[Löser 96] Andrè Löser, Transport in topologisch ungeordneten Systemen. Master's thesis, Technische Universität Chemnitz-Zwickau, 1996.

[Luchini 87] M. U. Luchini and C. M. M. Nex, J. Phys. C: Solid State Phys., Vol. **20**, page 3125, 1987.

[Maciá 00a] E. Maciá, Phys. Rev. B, Vol. **61**, page 8771, 2000.

[Maciá 00b] E. Maciá, Appl. Phys. Lett., Vol. **77**, page 3045, 2000.

[Maciá 00c] E. Maciá and F. Domínguez-Adame, Electrons, phonons and excitons in low dimensional aperiodic systems. Editorial Complutense S. A., Madrid, 2000.

[Maciá 01] E. Maciá, Phys. Rev. B, Vol. **64**, page 94206, 2001.

[Madel 00] C. Madel, *Elektronische Transporteigenschaften von amorphem und quasikristallinem Al-Cu-Fe.* PhD thesis, Technische Universität Chemnitz, 2000.

[Mahan 90] G. D. Mahan, Many particle physics. Plenum, New York, 1990.

[Martin 91] S. Martin, A.F. Hebard, A.R. Kortan and F.A. Thiel, Phys. Rev. Lett., Vol. **67**, page 719, 1991.

[Mastronardi 99] K. Mastronardi, D. Young, C. C. Wang, P. Khalifah, R. J. Cava and A. P. Ramirez, Appl. Phys. Lett., Vol. **74**, page 1415, 1999.

[Mayou 93] D. Mayou, C. Berger, F. Cyrot-Lackmann, T. Klein and P. Lanco, Phys. Rev. Lett., Vol. **70**, N. 25, page 3915, 1993.

[Mayou 94] D. Mayou, in F. Hippert and D. Gratias, Lectures on quasicrystals, page 417. Editions de Physique, Les Ulis-France, 1994.

[Mayou 00] D. Mayou, Phys. Rev. Lett., Vol. **85**, page 1290, 2000.

[McMillan 81] W. L. McMillan, Phys. Rev. B, Vol. **24**, page 2739, 1981.

[Mihalkovič 96] M. Mihalkovič, W.-J. Zhu, C. L. Henley and R. Phillips, Phys. Rev. B, Vol. **53**, page 9021, 1996.

[Mizutani 94] U. Mizutani, Y. Yamada, T. Takeuchi, K. Hashimoto, E. Belin, A. Sadoc, T. Yamauchi and T. Matsuda, J. Phys.: Cond. Matter, Vol. **6**, page 7335, 1994.

[Mizutani 98] U. Mizutani, J. Phys.: Cond. Matter, Vol. **10**, page 4609, 1998.

[Monkhorst 76] H.J. Monkhorst and J.D. Pack, Phys. Rev. B, Vol. **13**, page 5188, 1976.

[Morgan 85] G. J. Morgan and M. A. Howson, J. Phys. C: Solid State Phys., Vol. **18**, page 4327, 1985.

[Mott 36] N. F. Mott and H. A. Jones, The Theory of the Properties of Metals and Alloys. Clarendon, Oxford, 1936.

[Mott 69] N.F. Mott, Philos. Mag., Vol. **19**, page 835, 1969.

[Mott 87] N.F. Mott, Conduction in non-crystalline materials. Oxford Univ. Press., New York, 1987.

[Nolting 97] W. Nolting, Grundkurs theoretische physik 7: Viel-teichen-theorie. Vieweg & Sohn, Braunschweig/Wiesbaden, Germany, 1997.

[Nowak 91] H. J. Nowak, O. K. Andersen, T. Fujiwara and O. Jepsen, Phys. Rev. B, Vol. **44**, page 3577, 1991.

[Oliveira 00] I. S. Oliveira, Eur. Phys. J. B., Vol. **14**, page 43, 2000.

[Passaro 92] B. Passaro, C. Sire and V. G. Benza, Phys. Rev. B, Vol. **46**, page 13751, 1992.

[Perrot 95] A. Perrot, J. M. Dubois, M Cassart and J. P. Issi, *Thermal conductivity and Lorenz number in Al-Cu-Fe quasicrystals.* in C. Janot and R. Mosseri, Proceedings of the 5th International Conference on Quasicrystals, World Scientific, page 588. Avignon, 1995.

[Pierce 93a] F. S. Pierce, P. A. Bancel, B. D. Biggs, Q. Guo and S. J. Poon, Phys. Rev. B, Vol. **47**, page 5670, 1993.

[Pierce 93b] F. S. Pierce, S. J. Poon and B. D. Biggs, Phys. Rev. Lett., Vol. **70**, page 3919, 1993.

[Pierce 94] F. S. Pierce, Q. Guo and S. J. Poon, Phys. Rev. Lett., Vol. **73**, page 2220, 1994.

[Poon 92] S.J. Poon, Advances in Physics, Vol. **41**, page 303, 1992.

[Pope 99] A. L. Pope, T. M. Tritt, M. A. Chernikov and M. Feuerbacher, Appl. Phys. Lett., Vol. **75**, page 1854, 1999.

[Pope 01] A. L. Pope, T. M. Tritt, R. Gagnon and J. Strom-Olsen, Appl. Phys. Lett., Vol. **79**, page 2345, 2001.

[Quiquandon 97] M. Quiquandon, D. Gratias, J. Devaud, A. Le Lann, M. J. Hÿtch, L. Bresson and A. Katz, *Translation defects in the cubic approximant of the icosahedral phase in Al-Si-Cu-Fe system.* in S. Takeuchi and T. Fujiwara, Proceedings of the 6th International Conference on Quasicrystals, World Scientific, page 239. , 1997.

[Rapp 99] Ö Rapp. Physical Properties of Quasicrystals, page 127. Springer-Verlag, Berlin, 1999.

[Rieth 95] H. Rieth, *Untersuchung der Lokalisierung von elektronischen Eigenzuständen in quasiperiodischen Gittern.* PhD thesis, Technische Universität Chemnitz, 1995.

[Roche 97a] S. Roche and D. Mayou, Phys. Rev. Lett., Vol. **79**, N. 13, page 2518, 1997.

[Roche 97b] S. Roche, G. Trambly de Laissardiere and D. Mayou, J. Math. Phys., Vol. **38**, page 1794, 1997.

[Roche 98] S. Roche and T. Fujiwara, Phys. Rev. B, Vol. **58**, N. 17, page 11338, 1998.

[Rogan 01] J. Rogan and M. Lagos, Philos. Mag. B, Vol. **81**, page 551, 2001.

[Roth 99] C. Roth, G. Schwalbe, R. Knöfler, F. Zavaliche, O. Madel, R. Haberkern and P. Häussler, J. Non-Cryst. Solids, Vol. **250-252**, page 869–873, 1999.

[Sahnoune 92] A. Sahnoune, J. O. Ström-Olsen and A. Zaluska, Phys. Rev. B, Vol. **46**, N. 17, page 10629, 1992.

[Sales 96] B. C. Sales, D. Mandrus and R. K. Williams, Science, Vol. **272**, page 1325, 1996.

[Sharp 99] J. W. Sharp, B. C. Sales, D. G. Mandrus and B. C. Chakoumakos, Appl. Phys. Lett., Vol. **74**, page 3794, 1999.

[Shechtman 84] D. Shechtman, I. Blech, D. Gratias and J. W. Cahn, Phys. Rev. Lett., Vol. **53**, page 1951, 1984.

[Sin 84] H. K. Sin, P. Lindenfeld and W. L. McLean, Phys. Rev. B, Vol. **30**, page 4067, 1984.

[Sire 94] C. Sire, in F. Hippert and D. Gratias, Lectures on quasicrystals, page 505. Editions de Physique, Les Ulis-France, 1994.

[Skriver 84] H. L. Skriver, The LMTO Method. Springer-Verlag, Berlin, Heidelberg, New York, Tokyo, 1984.

[Smith 87] A.P Smith and N.W. Ashcroft, Phys. Rev. Lett., Vol. **59**, N. 12, page 1365, 1987.

[Smith 01] N. V. Smith, Phys. Rev. B, Vol. **64**, page 155106, 2001.

[Sob 88]	M. Sob, O. Jepsen and O.K. Andersen, Z. Phys. Chem. (Neue Folge), Vol. **157**, page 515, 1988.
[Solbrig]	H. Solbrig, 2002, private communication.
[Solbrig 87]	H. Solbrig, phys. stat. sol. (b), Vol. **139**, page 223, 1987.
[Solbrig 00a]	H. Solbrig and C. V. Landauro, Physica B, Vol. **292**, page 47, 2000.
[Solbrig 00b]	H. Solbrig, C. V. Landauro and A. Löser, Mater. Sci. Eng. A, Vol. **294-296**, page 596, 2000.
[Stadnik 95]	Z. M. Stadnik, G. W. Zhang, A. P. Tsai and A. Inoue, Phys. Rev. B, Vol. **51**, page 4023, 1995.
[Stadnik 97]	Z. M. Stadnik, D. Purdie, M. Garnier, Y. Baer, A.-P. Tsai, A. Inoue, K. Edagawa, S. Takeuchi and K. H. J. Buschow, Phys. Rev. B, Vol. **55**, page 10938, 1997.
[Stadnik 99]	Z. M. Stadnik. Physical Properties of Quasicrystals, page 257. Springer-Verlag, Berlin, 1999.
[Stein 80]	Stein and U. Krey, Z. Physik B, Vol. **37**, page 13, 1980.
[Sugiyama 98a]	K. Sugiyama, N. Kaji and K. Hiraga, Z. kristallogr., Vol. **213**, page 168, 1998.
[Sugiyama 98b]	K. Sugiyama, T. Kato, K. Saito and K. Hiraga, Philos. Mag. Lett., Vol. **77**, page 165, 1998.
[Takeuchi 00]	T. Takeuchi, H. Yamada, M. Takata, T. Nakata, N. Tanaka and U. Mizutani, Mater. Sci. Eng. A, Vol. **294-296**, page 340–344, 2000.
[Tamura 97]	R. Tamura, H. Sawada, K. Kimura and H. Ino, . in S. Takeuchi and T. Fujiwara, Proceedings of the 6th International Conference on Quasicrystals, World Scientific. , 1997.
[Tamura 01]	R. Tamura, T. Asao and S. Takeuchi, Phys. Rev. Lett., Vol. **86**, page 3104, 2001.
[Tang 97]	X.-P. Tang, E. A. Hill, S. K. Wonnell, S. J. Poon and Y. Wu, Phys. Rev. Lett., Vol. **79**, page 1070, 1997.
[Tank 00]	R. W. Tank and C. Arcangeli, phys. stat. sol. (b), Vol. **217**, page 89, 2000.
[Tei-Ohkawa 93]	K. Tei-Ohkawa, K. Edagawa and S. Takeuchi, J. Non-Cryst. Solids, Vol. **153-154**, page 264, 1993.
[Trambly 94]	G. Trambly de Laissardiére and T. Fujiwara, Phys. Rev. B, Vol. **50**, N. 9, page 5999, 1994.
[Trambly 95]	G. Trambly de Laissardiére, D. Nguyen Manh, L. Magaud, Julien J. P., F. Cryot-Lackmann and D. Mayou, Phys. Rev. B, Vol. **52**, N. 11, page 7920, 1995.

[Trambly 97] G. Trambly de Laissardiére and D. Mayou, Phys. Rev. B, Vol. **55**, N. 5, page 2890, 1997.

[Traverse 96] A. Traverse, E. Belin, Z. Dankhazi, L. Mendoza-Zelis, O. Laborde and R. Poltier, J. Phys.: Cond. Matter, Vol. **8**, page 3843, 1996.

[Tsai 89] A. P. Tsai, A. Inoue and T. Masumoto, Mater. Trans. Jpn. Inst. Met., Vol. **30**, page 463, 1989.

[Tsai 99] A. P. Tsai. Physical Properties of Quasicrystals, page 5. Springer-Verlag, Berlin, 1999.

[Tsallis 88] C. Tsallis, J. Stat. Phys., Vol. **52**, page 479, 1988.

[Tsallis 99] C. Tsallis, Braz. J. Phys., Vol. **29**, page 1, 1999.

[Tsunetsuga 91] H. Tsunetsuga and K. Ueda, Phys. Rev. B, Vol. **43**, page 8892, 1991.

[Turek 97] I. Turek, V. Drchal, J. Kudrnovský, M. Šob and P. Weinberger, Electronic structure of disordered alloys, surfaces and interfaces. Kluwer Academic, Boston, London and Dordrecht, 1997.

[Villagonzalo 99] C. Villagonzalo, R. A. Römer and M. Schreiber, Eur. Phys. J. B., Vol. **12**, page 179, 1999.

[Villars 91] P. Villars and L. D. Calvet, Pearson's handbook of crystallographie data for intermetallic phase. American Society for Metals, Materials Park, OH, second edition, 1991.

[Windisch 94] M. Windisch, M. Krajčí and J. Hafner, J. Phys.: Cond. Matter, Vol. **6**, page 6977, 1994.

[Yamamoto 95a] S. Yamamoto and T. Fujiwara, Phys. Rev. B, Vol. **51**, page 8841, 1995.

[Yamamoto 95b] S. Yamamoto and T. Fujiwara, Phys. Rev. B, Vol. **53**, page R2910, 1995.

[Yokoyama 92] Y. Yokoyama, T. Miura, A.-P. Tsai, A. Inoue and T. Masumoto, Mater. Trans. Jpn. Inst. Met., Vol. **33**, page 97, 1992.

[Yoshizumi 88] S. Yoshizumi, T. H. Geballe, M. Kunchur and W. L. McLean, Phys. Rev. B, Vol. **37**, page 7094, 1988.

[Zhao 90] G.-L. Zhao, Yi He and W. Y. Ching, Phys. Rev. B, Vol. **42**, N. 17, page 10887, 1990.

[Zijlstra 00] E. S. Zijlstra and T. Janssen, Europhys. Lett., Vol. **52**, page 578, 2000.

[Zijlstra 01] E. S. Zijlstra, *Electronic properties of quasicrystals. A tight-binding study.* PhD thesis, Katholieke Universiteit Nijmegen, 2001.

[Ziman 61] J. M. Ziman, Phil.Mag., Vol. **6**, page 1013, 1961.

List of figures and tables

Figures

Tables

Abbreviations

1.BZ	First Brillouin zone
ADOS	Average Density of states
ASA	Atomic Sphere Approximation
DOS	Density of States
FOM	Figure of merit
KKR	Korringa, Kohn, Rostoker (Method)
LBA	Landauer/Büttiker approach
LMTO	Linear Muffin-Tin Orbitals (Basis)
LDOS	Local Density of states
MIT	Metal-insulator transition
MTSW	Muffin-Tin Scattered Wave
TBLMTO	Tight-Binding Linear Muffin-Tin Orbitals (Basis)
TDOS	Total Density of states
TM	Transition Metals
VRH	Variable Range Hopping

bcc	body centered cubic
d-	decagonal
fcc	face centered cubic
i-	icosahedral

Symbols

ε	Electron Energy
ε_F	Fermi Energy
ε_F^{sc}	Selfconsistently calculated Fermi energy
$\widehat{n}(\varepsilon)$	DOS
$\widehat{n}_{\underline{R}L}(\varepsilon)$	LDOS
$\langle\widehat{n}_{\underline{R}L}(\varepsilon)\rangle$	ADOS
$\widehat{\sigma}(\varepsilon)$	Spectral Conductivity
$\widehat{\rho}(\varepsilon)$	Spectral Resistivity
$\widehat{D}(\varepsilon)$	Spectral Diffusivity
$P(\varepsilon)$	Participation ratios

$\tilde{\sigma}(\omega)$	Complex optical conductivity
$\sigma_1(\omega)$	Real part of the complex optical conductivity

T	Temperature
$\mu(T)$	Chemical potential
ξ	Temperature dependent part of the chemical potential
$\sigma(T)$	Conductivity
$\rho(T)$	Resistivity
$S(T)$	Thermoelectric Power
$R_H(T)$	Hall Coefficient
$K_t(T)$	Thermal Conductivity, total
$K(T)$	Thermal Conductivity, electronic part
$K_L(T)$	Thermal Conductivity, lattice part
$L(T)$	Lorenz Number

$(\underline{R})$	Atomic sphere at $\underline{R}$

$[\underline{R}]$	Atomic polyhedron at $\underline{R}$
$\mathrm{A}[\underline{R}]$	Polydron surface at atom $\underline{R}$
Ω	Volume of the system
Ω_{cell}	Volume of the unit-cell

Constants

a_0	Bohr radius
m_e	electronic mass
e	negative electronic charge
$\hbar = h/2\pi$	Planck constant
k_B	Boltzmann constant
ϵ_0	Dielectric constant

Atomic units

$$\begin{aligned} \varepsilon^2 &= \tfrac{e^2}{4\pi\epsilon_0} \ , \\ 1 \text{ a.u.} &= a_0 = \left(\tfrac{\hbar^2}{2m_e}\right)\tfrac{2}{\varepsilon} = 0.529177\text{Å} \\ 1 \text{ ryd.} &= \left(\tfrac{\hbar^2}{2m_e}\right)\tfrac{1}{a_0^2} = 13.605 \text{ eV} \end{aligned}$$

Selbständigkeitserklärung

Ich erkläre, dass ich die vorliegende Arbeit selbständig und nur unter Verwendung der angegebenen Literatur und Hilfsmittel angefertigt habe.
Ich erkläre, nicht bereits früher oder gleichzeitig bei anderen Hochschulen oder an dieser Universität ein Promotionsverfahren beantragt zu haben.
Ich erkenne die Promotionsordnung der Fakultät für Naturwissenschaften der Technischen Universität Chemnitz vom 10. Oktober 2001 an.

Chemnitz, den 11. April 2002

Carlos V. Landauro Sáenz

Danksagung

An erster Stelle möchte ich dem Leiter unsere Arbeitsgruppe, Herrn Prof. Dr. H. Solbrig, danken vor allem für die unermüdliche Anleitung, die zahlreichen fruchtbaren Diskussionen und dafür, dass er es ermöglicht hat, intensiv auf dem hier dargestellten Forschungsgebiet zu arbeiten.

Zunächst möchte ich mich bei Dr. Hans Nowak bedanken für die stetige großzügige Unterstützung an Anfang meiner Doktorarbeit sowie für die zahlreichen Diskussionen über die LMTO Methode und die Rekursionsverfahren.

In den vergangenen Jahren hatte ich Gelegenheit zu zahlreichen Gesprächen und Diskussionen bezüglich der in dieser Arbeit dargelegten Thematik. Ich möchte mich daher zunächst bei allen Mitgliedern der Arbeitsgruppe für die Anregungen und Hinweise bedanken, die ich diesen Diskussionen entnehmen konnte.

Mein Dank gilt auch für Prof. Dr. Peter Häussler und seine Arbeitsgruppe für die viele Diskussionen in Bezug auf der Vergleich von Experimenten und Rechnungen.

Dr. E. Maciá und Dr. E. S. Zijlstra danke ich für die interessanten Diskussionen gegen Ende dieser Arbeit.

Ganz besonders bin ich meiner Frau und meinen Familie zu Dank verpflichtet für die stetige und großzügige Unterstützung meiner Arbeit.

Diese Arbeit wurde durch die Graduiertenkolleg: ,,Dünne Schichten und nichtkristalline Materialien” (TU Chemnitz) und die ,,Deutsche Forschungsgemeinschaft” im Rahmen des Schwerpunktprogramms ,,Quasikristalle” gefördert. Dafür möchte ich mich an dieser Stelle bei den Verantwortlichen bedanken.

Lebenslauf

Name: Carlos Landauro Sáenz

Familienstand: verheiratet, keine Kinder

02. März 1972	geboren in Huaraz, Peru
1978 bis 1983	Grundschulzentrum 1084 Jesús María. Lima. Peru
1984 bis 1988	Oberschule ,,C.N.V. Diego Ferré” Jesús María. Lima. Peru
1989 bis 1994	Universidad Nacional Mayor de San Marcos, Hauptstudium Physik, Abschluß: Bakalarius Grad
1995	Licenciaturarbeit: Quantentheorie des Laser ohne die ,,Rotating Wave Approximation” Abschluß: Licenciado in Physik. Prädikat: 18/20
1995 bis 1996	Pontificia Universidad Católica del Perú, Magisterstudium, (drei von vier Semestern)
1996 bis 1999	Graduiertenkolleg
seit 1999	wissenschaftlicher Mitarbeiter an der Technischen Universität Chemnitz, Institut für Physik, Professur Struktur und Elektronenstruktur nichtkristalliner Materialien